KING SAUD UNIVERSITY
COLLEGE OF ENGINEERING
ELECTRICAL ENGINEERING DEPARTMENT

IMAGE FUSION BASED ENHANCEMENT OF ELECTROMAGNETIC NONDESTRUCTIVE EVALUATION

BY

AYED SALMAN M. ALGARNI

SUBMITTED IN PARTIAL FULFILLMENT OF THE REQUIREMENT FOR THE DOCTOR OF PHILOSOPHY DEGREE IN THE DEPARTMENT OF ELECTRICAL ENGINEERING AT THE COLLEGE OF ENGINEERING OF KING SAUD UNIVERSITY

RIYADH
Rajab 1430 A.H.
July 2009 A.D.

بسم الله الرحمن الرحيم

IMAGE FUSION BASED ENHANCEMENT OF ELECTROMAGNETIC NONDESTRUCTIVE EVALUATION

BY

AYED SALMAN M. ALGARNI

This PhD. Dissertation was discussed on Rajab 25th, 1430 (July 18th 2009) and was accepted.

Committee Members

Supervisors:

Dr. Ibrahim M. Elshafiey

Dr. Majeed A. Al-Kanhal

Internal Examiners:

Prof. Awad K. Al-Asmari

Dr. Zeyad O. AL-Hekail

External Examiner:

Prof. Samir Fahmi Mahmoud

TO MY PARENTS AND MY FAMAILY

ACKNOWLEDGMENTS

I would like to express my gratefulness to the Saudi Ministry of Defense and Aviation for the support of this research and the supporting of my scholarship at King Saud University.

I would like also to thank everyone who helped me in conducting this dissertation. First, it is a great pleasure for me to express my appreciation and gratitude to my supervisors Dr. Ibrahim Elshafiey, and Dr. Majeed Alkanhal. Dr. Elshafiey guided and reviewed the dissertation proposal as well as his direct participation and supervision throughout the research milestones, while Dr. Majeed supported, and encouraged me, in addition to his supervision throughout the research. My thanks go to Prof. Saad Alghuwainem for his support in using the PC's in the simulator lab.

My gratitude is also due to Prof. Tariq Alkhalifah, the director of the Astronomy and Geophysics Research Institute, King Abdulaziz City for Science and Technology who facilitated the use of the equipment and facilities of his institute during the experimental work of this research.

Also I would like to thank King Abdulaziz City for Science and Technology (KACST), Grant No: (99 – 15 – أط) and Research Center, College of Engineering King Saud University for funding this research.

Moreover, I would like to thank my parents, wife, children, brothers, and sisters for support and encouragement which have made the completion of this dissertation possible. First and last praise be to Allah for help and guidance in preparing this PhD dissertation.

تعزيز مبني على دمج الصور للتقويم غير المتلف الكهرومغناطيسي

ملخص

تستخدم الاختبارات غير المتلفة في مجالات عديدة منها المجالات الصناعية لكشف عيوب أو خصائص المواد الصناعية وهناك العديد من الطرق التي يمكن استخدامها لعمل هذه الاختبارات كما أن لكل طريقة مميزاتها وعيوبها و يتم المقايضة بين المميزات والعيوب عند اختيار طريقة الفحص ولذا أصبح من المتعارف عليه أن طريقة فحص واحدة لا تكفي لعمل اختبارات دقيقة و موثوقة خاصة عندما تكون المواد مركبة أو ذات أشكال معقدة. ولذلك أصبح من الضروري استخدام أكثر من طريقة لعمل الفحوصات. ولذا كانت هذه الرسالة تقدم دراسة بحثية تعتمد على دمج الصور الناتجة عن الفحص بأكثر من طريقة لتحسين أداء الاختبارات الغير متلفة الكهرومغناطيسية.

يركز البحث على الصور التي يتم إنتاجها باستخدام الطريقة الكهرومغناطيسية التي تسمى التيارات الدوامة وقد تم أولا بناء نموذج حسابي لطريقة التيارات الدوامة التقليدي وطريقة التيارات الدوامة النبضية يعتمد في إيجاد الحل على طريقة العناصر المحدودة (FEM), وذلك لدراسة الظاهرة الفيزيائية وتحديد تأثير العيوب، أو التشوهات، أو الشقوق المصنعية على عناصر المستشعر المختلفة مثل الممانعة أو المحاثة أو فرق الجهد المستشعر بحيث يتم تسجيل نتائج التغير في عناصر المستشعر أثناء عملية الفحص المسحي وترتيبها بحيث تظهر على شكل صور.

في المرحلة الثانية من هذه الدراسة تم بناء نظام حسابي لمعرفة شكل الضوضاء الناتجة عن التغير العشوائي في المسافة بين المستشعر والجسم المراد فحصة (liftoff) وكذلك التغير العشوائي في خاصية التوصيل الكهربائي للمادة (conductivity) المراد فحصها على عناصر المستشعر، على افتراض أن التغير العشوائي يتم تبعا للتوزيع الطبيعي المسمى (Gaussian distribution) وبعد أن تم بناء النموذج الحسابي وحساب تأثير التغير العشوائي على خصائص المستشعر لعدد 260 حاله أصبح لدينا قاعدة عامه من خلالها يمكن التنبؤ بنوع الضوضاء المؤثرة ومن ثم إضافة هذا التأثير على نتائج النموذج الحسابي ليصبح اقرب ما يمكن للواقع.

ثالثا تم بناء نظام معملي للتصوير بطريق التيارات الدوامة وذلك بطريقتين مختلفتين لعملية التصوير. الأولى باستخدام آلة الرسم (Roland X-Y plotter DXY-1150A) في عملية المسح حيث تم إنتاج صور صناعية ذات كفاءة حقلية. النظام المعملي الثاني الذي تم تقديمه في هذا البحث يعتمد على إنسان آلي (Robot) ذو

ست درجات لحرية الحركة لإجراء المسح والذي يعطي دقة تصل إلى 0.1 مم. الطريقة الآلية التي تم تقديمها تمثل خطوة نحو التقنية القادمة لأنظمة الفحوصات الغير متلفة الصناعية. الصور التي تم إنتاجها عمليا بطريقة التيارات الدوامة تحتاج إلي عملية تسجيل (registration) مع الصور الضوئية وذلك لجعل الصور متطابقة تماما قبل عملية الدمج. تسجيل الصور تم بطريقة اختيار نقاط تحكم في الصور المراد تسجيلها.

في المرحلة الرابعة تم تصميم نظام لدمج الصور المستخرجة من نظام المحاكاة الحسابي وكذلك من النظام المعملي تحت قيود وخصائص مختلفة. يعتمد هذا النظام على عملية التحويل لدمج الصور التي تسمى (Intensity Hue Saturation)، حيث تم بناء عدد من النماذج المطورة من هذه الطريقة تعتمد على التحليل المسمى (Wavelet) و مبدأ تحليل العناصر (Principal Component Analysis).

أنظمة الاختبارات الغير متلفة المتوفرة حاليا تعتمد غالبا على قرار المشغل البشري غير الكمي بينما الأنظمة المستقبلية التي تسعى مراكز الأبحاث لإنتاجها تعتمد على إنتاج أنظمة ذكية يمكنها التعامل مع كميات محددة لجعل عملية الفحص آلية. هذا البحث يطور عدد من طرق القياس الكمية التي يمكن استخدامها لقياس فعالية الدمج ولتكون الخطوة الأولى في سبيل جعل عملية الفحص آلية. طرق القياس الكمية التي تم تقديمها في هذا البحث تنقسم إلى قسمين طرق قياس كمية تعتمد على وجود صورة مرجعية وأخرى لا تعتمد على وجود صورة مرجعية. الطرق التي تحتاج صورة مرجعية للمقارنة معها هي جذر المعدل لمربع الخطاء (RMSE)، الترابط (CORR)، ذروة نسبة الإشارة إلى الضوضاء (PSNR)، المعلومات المشتركة (MI) و هيكلية المعلومات والتشابه الهيكلي (SSIM)، أما الطرق التي لا تشترط وجود المرجعية فهي الانحراف المعياري (SD)، كمية المعلومات (H) و مؤشر الجودة (QE).

المقارنة التي تم دراستها في هذا البحث باستخدام طرق القياس الكمية لعدد من طرق الدمج أظهرت أداء أفضل لطرق الدمج التي تعتمد على (Intensity Hue Saturation) قد يصل إلى 28% و يختلف باختلاف المقياس المستخدم.

إلى أقصى حدود معرفة الباحث فانه تم في هذا البحث تقديم طريقة جديدة لدمج الصور في تطبيقات الفحوصات الكهرومغناطيسية الغير متلفة. وقد تم اختبار هذا النظام باستخدام تقنية الإنسان الآلي و تصنيع هذا النظام ينبغي أن يكون ممكنا في المستقبل القريب وسيكون له أثر كبير على الفحوصات الغير متلفة الصناعية بصفة عامة وعلى الصناعة في المملكة العربية السعودية بصورة خاصة.

Image Fusion Based Enhancement of Electromagnetic Nondestructive Evaluation

Abstract

Nondestructive evaluation NDE is implemented in various industrial sectors. Different modalities have been developed for NDE applications during the last few decades. The advantages and limitations associated with each modality raises a tradeoff in which no single nondestructive evaluation (NDE) inspection technique can be identified for a particular application, particularly for complex structures. This dissertation presents a research based on image fusion approach to enhance electromagnetic NDE modalities.

First a computational model based on finite element method (FEM) analysis is designed to build the fusion system for eddy current (EC) inspection. Conventional as well as pulsed eddy current (PEC) modalities are used. C-scan images are generated corresponding to different EC excitation frequencies. Time domain metrics are obtained to generate the images corresponding to PEC. Where differential analysis model is used to produce C-scan images instead of conventional absolute analysis for both eddy current methods.

In the second phase of this research the developed model is implemented in a novel noise analysis of the inspection process. A total of 260 runs are conducted to model the liftoff and conductivity perturbation noise, based on Gaussian distribution model. The noise analysis model is to generalize the effect of noise on the probe impedance, and the results are validated with experimentally.

Two hardware EC imaging systems are designed and implemented to obtain experimental EC images in the third part of this research. The first system employs a Roland X-Y plotter as a scanning system, and is used to obtain field quality industrial images. The second introduced system is based on a six degree of freedom robot arm, manufactured by Stäubli, with 0.1 mm resolution, and is thus used to obtain high quality images. Advanced robotic systems being investigated for NDE applications can be considered the next generation of NDE industrial systems.

In the fourth phase the simulated as well as experimental images were used to design an innovative fusion system, where fusion system has been proposed based on pseudo-color interpretation of eddy color images. The proposed fusion system for NDE application is based on intensity hue saturation (IHS) transformation, improved with principal component analysis (PCA), and multi-resolution wavelet decomposition (MWD), where PCA can be used to generalize the fusion of arbitrary number of images.

The system can be used for multi-modal, multi-spectral and multi-temporal fusion. Image registration is implemented to highly correlate EC scan images and optical camera images of the object under test. The proposed systems are compared with other fusion methods namely discrete wavelet transform (DWT), shift invariant discrete wavelet transform (SIDWT), and Laplacian pyramid (LP).

The current status of NDE systems is characterized by commercial systems mostly dependent on the subjective judgment of the operator, and automated systems which are the main focus of research centers which provide objective evaluation. This research develops image evaluation measures (quality metrics) to cross the gap between subjective and objective evaluation. Some of the developed quality metrics

depend on reference image using techniques based on root mean square error (RMSE), correlation (CORR), peak signal to noise ratio (PSNR), mutual information (MI), and structural information, structural similarity (SSIM). The other methods are free from the need of reference image and are based on the standard deviation (SD), entropy (H), and Petrovic quality index (QE).

The comparison shows that the IHS based fusion system performs better than others fusion methods, where almost all quality metrics show increase in performance of the proposed system up to 28% depending on the quality metric.

To the best of knowledge of the author, the dissertation presents a novel system implementing image fusion in EM NDE applications. The system implements the state of the art hardware robotic equipment and image processing. Industrialization of the system, however, should be feasible in the near future and could have major impact for NDE industry, in general and in the Saudi industry in particular.

TABLE OF CONTENTS

ACKNOWLEDGMENTS..I

ملخص..II

Abstract..IV

TABLE OF CONTENTS..IVII

LIST OF FIGURES..X

LIST OF TABLES..XIV

CHAPTER 1 INTRODUCTION..1

1.1 Multimodal NDE..2

1.2 Outline and Aim of Present Study..4

1.3 Research Contributions..5

CHAPTER 2 DATA FUSION FOR NDE APPLICATIONS..7

2.1 Introduction..7

2.2 NDE Data Fusion..10

2.3 Eddy Current Fusion Methods..11

2.4 Ultrasonic Fusion Methods..13

2.5 Fusion Methods for other NDE Modalities..13

2.6 NDE Fusion Algorithms..14

2.6.1 Linear Minimum Mean Square Error (LMMSE)..15

2.6.2 Neural Networks (NN) Fusion..16

2.6.3 Multi-Resolution Analysis (MRA) Fusion..17

2.6.3.1 Laplacian Pyramid..18

2.6.3.2 Ratio of Low Pass Pyramid..21

2.6.3.3 Wavelet Fusion..21

2.6.3.4 Wavelet Image Fusion Rules..25

CHAPTER 3 EDDY CURRENT (EC) INSPECTION MODALITIES 27

3.1 Introduction 27

3.2 Analytical Formulation 30

3.3 Numerical Techniques 37

3.3.1 Finite Difference Method 38

3.3.2 Finite Element Method 38

3.4 Eddy Current Finite Element Realizations 41

3.5 Computational Modeling Implementation of Eddy Current 45

3.5.1 Power Loss 49

3.5.2 Energy in a Magnetic Field 50

3.5.3 Flux Passing Through a Closed Contour 50

3.6 Pulsed Eddy Current (PEC) 51

3.7 Analysis of Pulsed Eddy Current 52

CHAPTER 4 EDDY CURRENT IMAGING 60

4.1 Eddy Current Imaging 60

4.2 Experimental Eddy Current imaging 63

4.3 Image Registration Methodology 66

4.4 Eddy Current Noise Analysis 70

CHAPTER 5 FUSION PERFORMANCE EVALUATION 79

5.1 Objective Evaluation Measures Requiring a Reference Image 80

5.2 Objective Evaluation Measures Not Requiring a Reference Image 82

CHAPTER 6 PROPOSED NDE FUSION SYSTEMS 85

6.1 Introduction 85

6.2 Intensity-Hue-Saturation (IHS) Transform Fusion 87

6.3 Principal Component Analysis PCA Fusion 90

6.4 Improved IHS Based on Multi-resolution Wavelet Decomposition (MWD) Fusion Technique 94

6.5 NDE Fusion Results 100

6.5.1 Simulation Results 100

6.5.2 Experimental Results 107

CHAPTER 7 CONCLUSIONS AND FUTURE WORK 115

REFERENCES 120

LIST OF PUBLICATIONS 128

LIST OF FIGURES

Figure 1.1: Outline of the work done in this research.. 6

Figure 2.1: Data fusion procedure. 9
Figure 2.2: Image fusion levels.. 11
Figure 2.3: Model for Linear signal fusion ([40]).. 15
Figure 2.4: Procedure for multi-resolution image fusion ([1]). 19
Figure 2.5: The decomposition procedure of the image by DWT. 23
Figure 2.6: One stage 2-D DWT decomposition. 24
Figure 2.7: One stage 2-D SIWT decomposition. 24

Figure 3.1: Eddy current inspection... 28
Figure 3.2: Eddy current density.. 29
Figure 3.3: Typical eddy current problem ([50])... 34
Figure 3.4: Schematic plot for the model to be simulated. 45
Figure 3.5: Schematic plot for the model... 46
Figure 3.6: SOLID97 element geometry. 47
Figure 3.7: Meshed model. (Coarse to be clear)... 48
Figure 3.8: Layout of PEC inspection. 53
Figure 3.9: Typical PEC excitation pulse in time domain (a) and spectrum of frequency domain (b).. 55
Figure 3.10: Time domain picked up voltage signal for crack I.................................... 56
Figure 3.11: Time domain picked up voltage signal for crack II................................... 56
Figure 3.12: Time domain picked up voltage signal for crack III. 57
Figure 3.13: Time domain picked up voltage signal at origin for three cracks, with excitation pulse width 31.25μs. 58
Figure 3.14: Time domain picked up voltage signal at origin for three cracks, with excitation pulse width 78.125μs. 59
Figure 3.15: Time domain picked up voltage signal at origin for three cracks, with excitation pulse width 93.75μs. 59

Figure 4.1: Ten images representing probe resistance values R_1-R_5 (top row, left to right) and inductance values L_1-L_5 (bottom row, left to right) corresponding to five different frequencies: 100 Hz, 1 kHz, 10 kHz, 100 kHz, and 1M Hz.......................... 62
Figure 4.2: PEC images for the minimum amplitude feature for different excitation pulse width.. 62
Figure 4.3: PEC images for the time to minimum amplitude feature for different excitation pulse width. 62
Figure 4.4: PEC images for maximum amplitude for different feature for different excitation pulse width. 63
Figure 4.5: PEC image for the time to maximum feature taking the surface as a reference.. 63
Figure 4.6: Type I developed scanning system based on Roland X-Y plotter DXY-1150A... 64
Figure 4.7: Eddy current measurement system (Rohmann B 300)............................. 64
Figure 4.8: Staubli robot which is the main part of advanced type II scanning system. 65
Figure 4.9: Optical photo of the plate used in experimental measurements................ 65
Figure 4.10: Measured EC images at 10 kHz, 100 kHz, 300 kHz, and 800 kHz. 67
Figure 4.11: Four steps of image registration ([64])... 71
Figure 4.12: Normal probability plot of probe resistance noise at 100Hz................... 73
Figure 4.13: Normal probability plot of probe resistance noise at 10 kHz.................. 73
Figure 4.14: Normal probability plot of probe resistance noise at 100 kHz................ 74
Figure 4.15: Normal probability plot of probe resistance noise at 500 kHz................ 74
Figure 4.16: Normal probability plot of probe resistance noise at 1 MHz. 75
Figure 4.17: Normal probability plot of flux angle noise at 100Hz............................ 76
Figure 4.18: Normal probability plot of flux angle noise at 100kHz.......................... 76
Figure 4.19: Normal probability plot of flux angle noise at 500kHz.......................... 77
Figure 4.20: Normal probability plot of flux angle noise at 1MHz............................ 77
Figure 4.21: Gaussian noise added to EC images... 78

Figure 6.1: Eddy current Technology progress. 86
Figure 6.2: IHS fusion procedure.. 88
Figure 6.3: PCA fusion process. 93

Figure 6.4: Arbitrary number of inputs IHS fusion system. 94
Figure 6.5: Example of histogram matching... 96
Figure 6.6: Approximation and detail coefficients of intensity component image *I*. Daubechies wavelets were used. 97
Figure 6.7: Approximation and detail coefficients of HR image (HR= R_5). Daubechies wavelets were used. 98
Figure 6.8: Improved IHS fusion based on MWD. 99
Figure 6.9: Ten images representing probe resistance values R_1-R_5 (top row, left to right) and inductance values L_1-L_5 (bottom row, left to right) corresponding to five different frequencies: 100 Hz, 1 kHz, 10 kHz, 100 kHz, and 1M Hz........................ 101
Figure 6.10: Simple fusion, with 2 frequency domain images and one time domain image. 102
Figure 6.11: Fusion obtained with IHS transformation. 102
Figure 6.12: The first four principal components images computed from R_1-R_5 (the first row of Figure 6.9) 103
Figure 6.13: Fusion obtained with wavelet decomposition, where the high spatial resolution image was taken as R_5 103
Figure 6.14: Images used to evaluate the fusion algorithms, (a) maximum amplitude feature transient image, (b) time to maximum transient image, (c) probe L image at 10 kHz, (d) probe L at 1MHz as a HR. 104
Figure 6.15: Fusion results of the images shown in Figure 6.14, (a) LAP, (b) DWT, (c) SIDWT, (d) IHS, (e) IHSW. 106
Figure 6.16: Performance of fusion with standard deviation quality metric. 106
Figure 6.17: Performance of fusion with entropy quality metric............................... 107
Figure 6.18: Optical image of the test sample. 108
Figure 6.19: Experimental EC images at frequencies 10 kHz, 100 kHz, 300 kHz, and 800 kHz (top to bottom order). 109
Figure 6.20: Performance of fusion with mutual information quality metric. 110
Figure 6.21: Performance of fusion with structure information, structural similarity quality metric. 110
Figure 6.22: Performance of fusion with correlation quality metric. 111
Figure 6.23: Performance of fusion with root mean square error quality metric. 111
Figure 6.24: Performance of fusion with peak SNR quality metric. 112

Figure 6.25: Fusion results with the first three low frequencies images shown in figure 6.18, and optical image (IHS, IHSW, SIDWT, DWT, LAP top to bottom respectively). 113
Figure 6.26: Fusion results with the last three high frequencies images shown in figure 6.18, and optical image (IHS, IHSW, SIDWT, DWT, LAP top to bottom respectively). 114

LIST OF TABLES

Table 2.1: Some benefits of data fusion ([14]). 8

Table 2.2: Fusion algorithms applied to NDE. 14

Table 2.3: MRA based image fusion algorithms. 19

Table 4.1 Standard deviation of the real and imaginary components of the probe impedance 71

Table 6.1: Comparison between different quality measures for the fused images shown in Figure 6.15. 106

CHAPTER 1

INTRODUCTION

The subject of data fusion, in general, with application to Non Destructive Evaluation (NDE), has received significant attention in recent years [1]. Demand of the accuracy and reliability of any NDE system is increasing in many application requirements like aerospace and nuclear power industries. In order to meet these high requirements, a single sensor or individual measurement system can't meet such requirements. Thus multiple testing and inspection techniques are applied so that the evaluation can get the benefit of the advantages of different inspection environments or systems.

Various inspection measurements can then be combined with the help of advanced processing techniques for better evaluation results. The objective of signal processing is to extract as much information as possible from the given input signal which is usually derived from several sensors. In practice, it is often possible to employ different combination of sensors. Many choices of sensors combination are available which include using multiple sensors that are either identical or different.

Automation of inspection process requires the development of computational metrics that represent the quality of sample under test.

This chapter provides background of multimodal NDE followed by outline present study, then section about research contributions.

1.1 Multimodal NDE

NDE methods involve the application of a suitable form of energy to the specimen under test. A snapshot of the material/energy interaction process is then taken via an appropriate transducer and analyzed to ascertain the state of the specimen. This energy depends on the physical properties of the specimen, information needed and the test conditions. Therefore wide variety of testing methods has been presented. Each method has certain properties and offers some advantages as well as drawbacks, depending on the type of excitation energy, its amplitude, frequency and wavelength.

The basic categories of NDE methods are: visual and optical testing (VT), radiography (RT) particle (magnetic) testing (MT), ultrasonic testing (UT), penetrant testing (PT), electromagnetic testing (ET), leak testing (LT) and acoustic emission testing (AE).

Electromagnetic testing modalities operating frequency cover the entire electromagnetic spectrum. Techniques employing the static ($\omega = 0$) operation, such as the magnetic flux leakage, and the quasi-static frequency range such as eddy current methods are more commonly used in industry than higher frequency wave phenomenon methods [2] and [3]. However, attention is being made to the other end of the spectrum. Examples include application of microwave imaging techniques in inspecting civil structures [4]. At higher frequency ranges, thermal wave are being used in characterization of coating adhesion [5], optical methods are used in evaluating concrete and composite materials [6], and ionization frequency range as in x-ray techniques which is used in tomographical reconstruction of defects and in assessing residual stresses and crystalline texture of metal alloys. Hybrid techniques that operate

at both high and low frequency ranges are also used as in the case of magneto-optic / eddy current imaging method [7].

Among the ET modalities the EC get more attention, because of the hazardous precautions of the ionization frequency range, and in static range there is no time information. At the same time EC is one of the most sensitive and reliable methods for detecting surface and sub surface flaws, it can be performed through normal paint. The characteristics responsible for such popularity of this technique include simplicity, versatility, high sensitivity, non-contact operation, couplant free testing and high speeds of testing [8]. On the other hand the depth of penetration is limited by the single frequency of the probe. To overcome this limitation, multi frequency, and pulsed eddy current (PEC) was introduced [9] and [10].

Any system capable of extracting complementary segments of information from data collected from multiple NDE testing methods can offer additional insight relative to that obtained using one NDE testing method. For example, ultrasonic methods offer good penetration into the material and high resolution, but the signal suffer from poor signal to noise ratio (SNR), whereas electromagnetic methods offer good sensitivity and SNR, but poor resolution. Data fusion algorithms exploit both the redundancy and complementary information to enhance the resulting image. Redundant information is used to improve the SNR and complementary information is used to augment the overall information content, which increases the accuracy and reliability of inspection systems.

The limitations of a method or technique include conditions required by that method, conditions to be met for technique application (access, physical contact and preparation) and requirements to adopt the probe or probe medium to the test object.

1.2 Outline and Aim of Present Study

The dissertation can be divided into four parts:

- Part 1 introduces the computational modeling of conventional eddy current (EC), and pulsed eddy current (PEC) modalities, and presenting the EC inspection data in image format. This part is discussed in chapter 3 and section 4.1.
- Part 2 deals with EC noise analysis, where various modeling runs have been performed to model the liftoff and conductivity perturbation noise assuming Gaussian distribution. The second part is presented in sections 4.2, and 4.3.
- Part 3 EC images have been produced experimentally after the establishment of a lab and the resulting EC and optical images are registered. Experimental results and registration are presented in chapter 4.
- Part 4 of the research focuses on image fusion, where fusion system has been proposed, designed and tested using EC/PEC images acquired from computational model and EC/optical images acquired experimentally. Chapter 5 and 6 presents the performance evaluation measures and fusion systems with related results.
- Part 5 discusses the conclusions and future work in chapter 7.

A block diagram illustrates the outline of the work done in this dissertation shown in Figure 1.1. The block diagram also outlines the flow of this dissertation.

The aim of this research is to investigate how to enhance and characterize the NDE signal by the image fusion strategy. With typical NDE signals, the way to effectively acquire and present more useful information was studied. Enhance the

extracted information, and finally integrate this information together to increase the performance and reliability of inspection.

1.3 Research Contributions

The following contributions have been made in this study and reported in this dissertation.

In this research a novel study of fusion of conventional eddy current images and pulsed eddy current images is presented.

A new system has been developed to fuse multi-spectral, multi-temporal, and multi-spatial information in EC images. The proposed fusion system performs once as superior to many other fusion systems applied to NDE, according to various performance quality measures applied to the fusion systems results.

Noise simulation of Gaussian distribution of the liftoff and conductivity parameters have been investigated, and validated with experimental work; which indicate that the normality is preserved as the frequency increased.

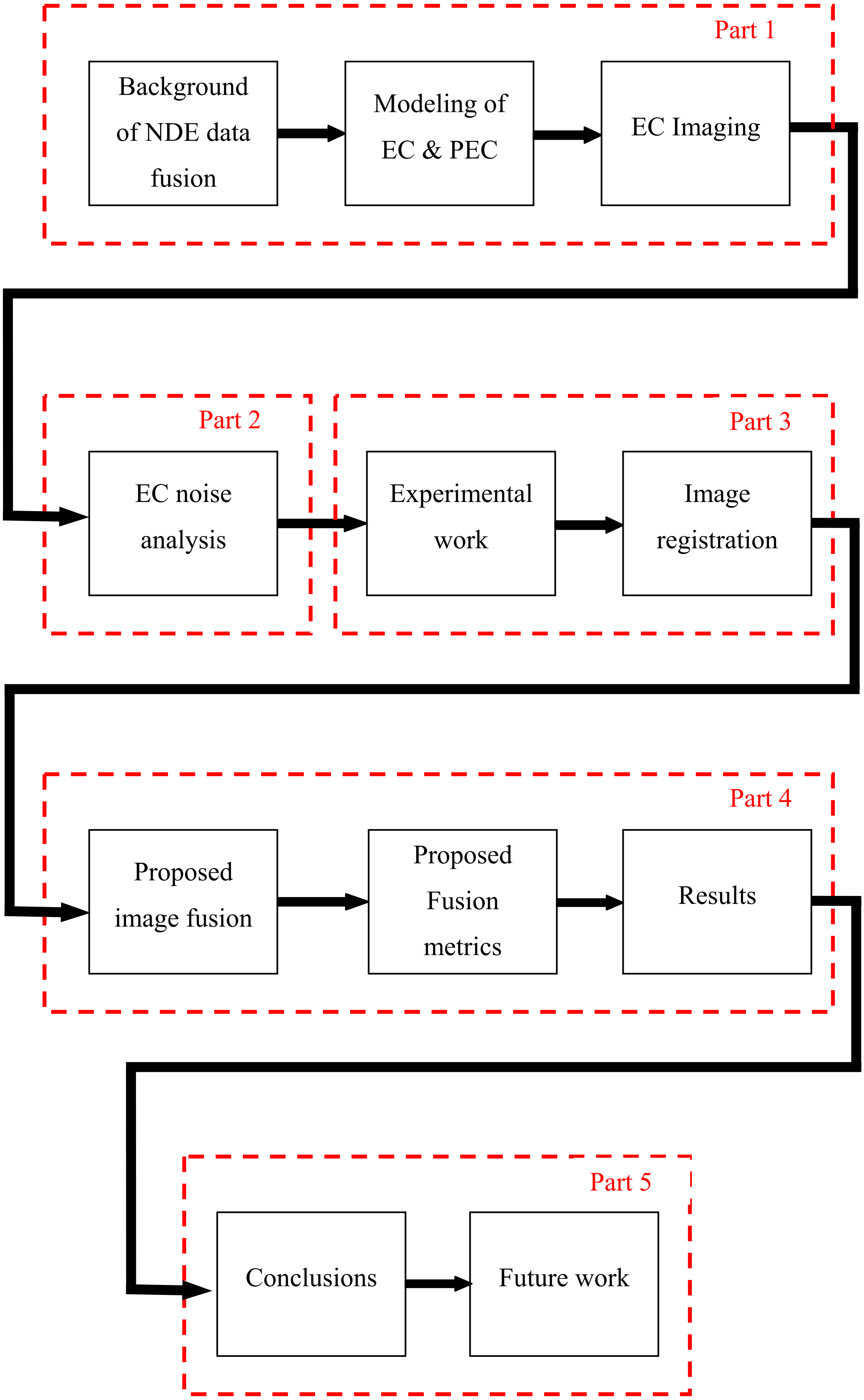


Figure 1.1: Outline of the work done in this research.

CHAPTER 2

DATA FUSION FOR NDE APPLICATIONS

2.1 Introduction

Data fusion in general, also known as multi-sensor data fusion or distributed sensing, is introduced to the military area in the 70s. It is such a technique that concerned with the problem of making inference from multiple sensors. Data fusion can be regarded as the processing, interpretation and use of data from multiple sources in order to make inferences about a physical event, activity, or situation. The brain of the human beings is the most complicated and accurate fusion center on earth, and praise be to the Creator. The sensory data or information, such as smell, taste, visual, and touch, are used by the brain, then a comprehensive impression about the environment or the object is deduced. As a part of this complicated system the human eye fuse spectral color information to enhance perception of objects.

There are many applications of data fusion, in military and non-military fields. Military applications include a wide range command, control, communication and intelligence (C3I) missions for both tactical and strategic warfare, such as battle surveillance, tactical situation assessment and thereof assessment [11]. Civilian

applications include concealed weapon detection (CWD) [12], robotics, automated manufacturing, remote sensing, medical diagnosis and nondestructive testing.

The benefits of data fusion are both quantitative and qualitative. Benefits include improved operational performance, extended spatial coverage, extended temporal coverage, increased confidence, reduced ambiguity of inferences, improved detection, enhanced spatial resolution, improved system reliability, and increased dimensionality [13]. Table 2.1 lists some of the benefits of fusion.

Table 2.1: Some benefits of data fusion ([14]).

Category of Benefit	Benefits
Operation performance	One sensor can contribute information while others are unavailable, denied, or lack coverage of a target.
Extended spatial coverage	One sensor can look while another cannot.
Extended temporal coverage	One sensor can detect an object when another cannot.
Increase confidential.	One or more sensor can confirm the same object.
Reduce ambiguity.	Joint information from multiple sensors reduces the set of hypotheses about the object
Improve detection	Effective integration of multiple measurements of the object increases the assurance of its detection.
Enhanced spatial resolution	Multiple sensors can geometrically form a synthetic aperture capable of greater resolution than a single sensor can form.
Improved system reliability	Multiple sensor suites have an inherent redundancy.
Increased dimensionality	A system employing different sensors to measure various portions of the electromagnetic spectrum is less vulnerable to disruption by enemy action or natural phenomena.

Figure 2.1 illustrates the general procedure for data fusion, where the data collected from sensors first preprocessed and then registered to the same physical space. Then the fusion technique is applied.

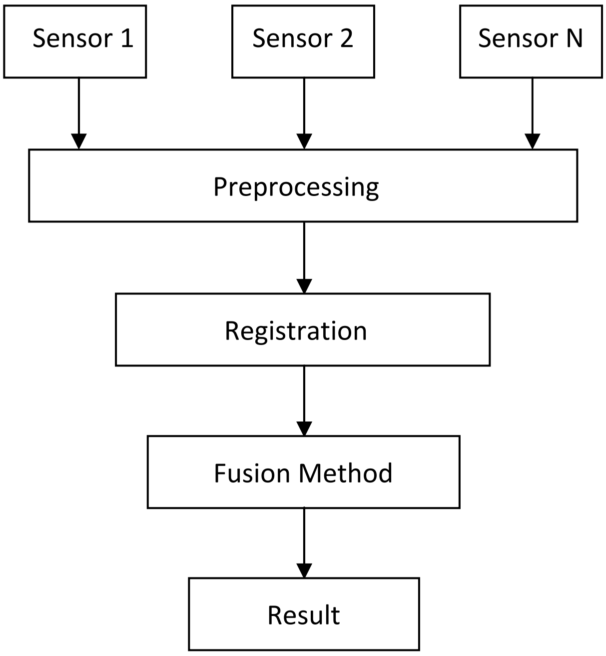


Figure 2.1: Data fusion procedure.

To date various image fusion methods have been proposed, starting from simple pixel averaging or linear weighted/un-weighted combination to more complicated techniques.

In this research, the pixel level fusion approaches are addressed with application to NDE. These fusion techniques applied to NDE can be divided into two groups: conventional and advanced methods. In conventional method two images are used as input for one stage fusion algorithm. This is the mostly used technique with application to NDE and will be reviewed in this chapter. The other group is the advanced method where more than two images could be used as input to the fusion approach. For the best of our knowledge, these techniques have not been applied in NDE field. This dissertation introduces these for NDE and will be described in chapter 6.

2.2 NDE Data Fusion

NDE data fusion can be traced back to early 90s [15]. Data fusion algorithms in NDE can be broadly classified as phenomenological or non- phenomenological. Phenomenological algorithms utilize knowledge of the underlying physical processes as a basis for deriving the procedure for fusing data. However, such methods are likely to be difficult to derive and cumbersome to implement [16]. Non- phenomenological approaches, in contrast, tend to ignore the physical process and attempts to fuse information using the statistics associated with individual segments of data. The later methods can be classified into three different categories, pixel level fusion, feature level fusion and symbol level fusion, according to the stage at which fusion takes place as illustrated in Figure 2.2.

Pixel based fusion requires accurate registration of the images to each other, where image registration is the process of aligning two or more images of the same scene.

Typically, one image, called the base image, is considered the reference to which the other images, called input images, are compared. The objective of image registration is to bring the input image into alignment with the base image by applying a spatial transformation to the input image. A spatial transformation maps locations in one image to new locations in another image. Image registration is often used as a preliminary step in other image processing applications; one of them is image fusion.

Techniques based on data level or pixel level fusion can be categorized under two umbrellas: color related techniques and statistical techniques. Example of color related techniques includes intensity-hue-saturation (IHS) transform, and example of statistical techniques includes principal component analysis (PCA). Fusion at feature

level requires the extraction of objects and then fusing those using statistical approaches or artificial neural network (ANN).

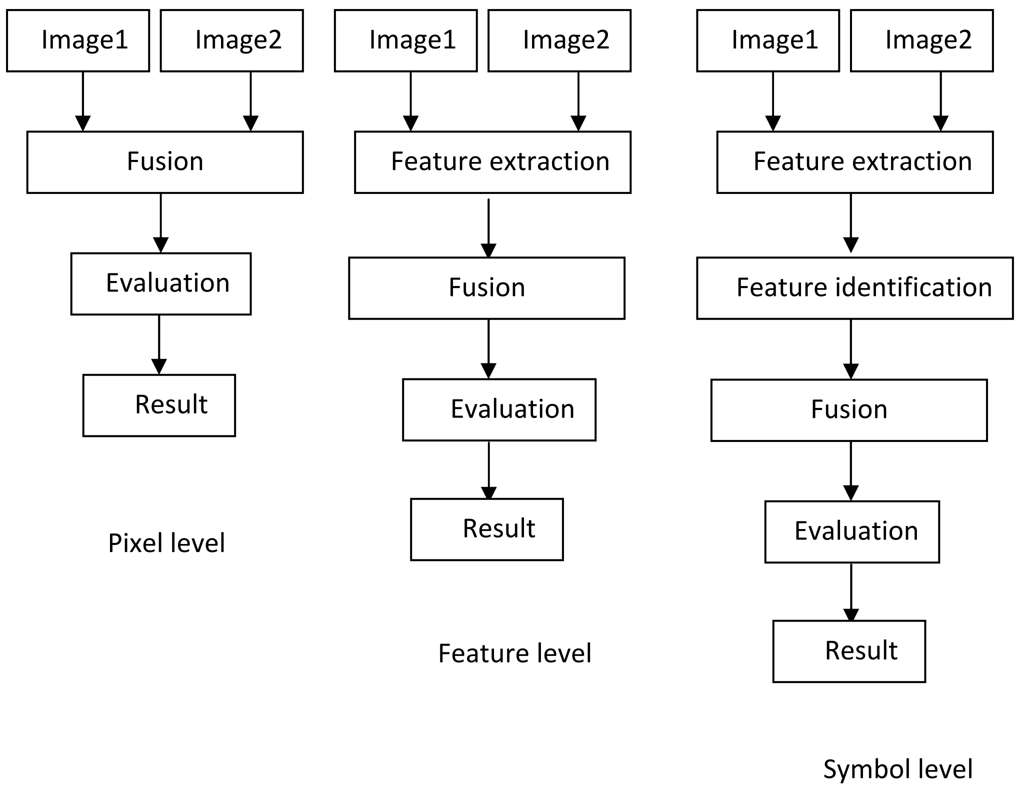


Figure 2.2: Image fusion levels.

Decision (Symbol) level fusion represents a method that uses value-added data where the input images are processed individually for information extraction. The obtained information is then combined by applying decision rules.

2.3 Eddy Current Fusion Methods

Eddy current testing (ET) is one of the electromagnetic inspection methods, which has number of popular industrial application starting from crack detection to the rapid sorting of small components for flaws and material variations. Various techniques

have been developed to put eddy current inspection data in the form of C-scan images [17] and [18].

Mina et al. [19] proposed a fusion algorithm that uses the data from both real and imaginary image components, using artificial cracks around rivet holes in an aluminum specimen. The operation was implemented in the frequency domain with the discrete Fourier transform. The fusion process is then based on the spectrum of the acquired signal, where the linear minimum mean square error (LMMSE) approach was adopted to fuse the images using a weighting scheme. The details of LMMSE approach will be discussed in section 2.6.

Multi-frequency eddy current testing (MF-ET) was proposed, where the lower frequency excited signals penetrate deeper into the specimen. The MF-ET technique was applied to inspect surface and subsurface flows on aluminum sample in [20]. The algorithms proposed in [19] were applied to the MF-ET C-scan data to achieve a better SNR. Yim et al. fused two ET scan images obtained at 6 and 20 KHz, with radial basis function (RBF) neural networks (NNs) [21]. A relatively clear display of subsurface flows is achieved after the fusion process. Pixel level fusion technique using a multi-resolution image pyramid was proposed in [22], a better SNR was achieved through the fusion of MF-ET data. Laplacian pyramid, and wavelet transform were investigated in the aforementioned studies.

Gros et al. [23] integrated the signals from two different ET systems in weld inspection; using the Dempster-Shafer (DS) combination rule and concluded that more accurate estimation of crack size was achieved.

2.4 Ultrasonic Fusion Methods

Ultrasonic Fusion (UT) is another widely exploited method in NDE, which uses sound waves of short wavelength and high frequency. The amplitude, frequency, or time of flight of the echo signals provides information about the nature and position of flaws. This method produces a measurement with high resolution but it is affected by the surface roughness of the specimen and grain structure of metals. Meanwhile it provides little information about the depth of narrow cracks. This method has main disadvantage because it requiring use of coupling liquid between transducer and specimen under test. Ultrasonic image was fused with eddy current images using the AND operation by Song and Udpa [24] in order to take advantage of both methods. Experiments were carried out on an aluminum plate where a simulated defect was present. The boundary of the defect was extracted from the UT image, whereas the depth information could be characterized from an ET image. Another way to fuse UT and ET data is the use of RBF NNs or multilayer perceptron (MLP). The experiments were carried out by Simone [16], to fuse eddy current and ultrasonic images showed that the fusion operation improves the process of defect classification.

2.5 Fusion Methods for other NDE Modalities

Infrared (IR) thermographic testing and ET C-scan was fused using wavelet-based methods, where an impacted carbon fiber reinforced plastic composite panel was used as in [25] and [26]. The fusion of IR and optical images was also found in the application of inspecting construction defects. The use of multiple inspection techniques for NDE application is increasing [27-29].

2.6 NDE Fusion Algorithms

Many algorithms have been developed for NDE data fusion. The main goal for NDE data fusion is to improve the reliability and the performance of testing. The fusion methods as found in the literature applied to NDE systems are listed in table 2.1 and the most widely applied are summarized next.

Table 2.2: Fusion algorithms applied to NDE.

Modality	Fusion Technique	Reference
EC / photo inductive imaging	Physical interaction / Human fusion	Cheng Chi, 2008 [30]
EC / PEC	Dempester-Shfer	Z. Liu, 2007 [31]
X-Ray / Ultrasonic	Evidence Theory / Fuzzy logic	Varlerie K., 2005 [29]
EC / Flux leakage	Barkhausen noise method	T. Chady, 2005 [32]
X-ray / Geometrical data	Bayesian	A. Djafari, 2002 [33]
X-ray/ Ultrasonic	Dempester-Shfer	Kaftandjian, 2002 [34]
EC/Ultrasonic	Feed forward Neural Networks (NN)	G. Simone, 2001 [16]
EC/Ultrasonic	NN	L, Udpa, 2001 [35]
EC, Infrared	Wavelet	X. E. Gros, 2000 [36]
Ultrasonic / radiographic	Wavelet	Matuszewski, 2000 [37]
Edge of light / PEC	Image subtraction	Forsyth, 2000 [38]
Multi-frequency EC	Multiresolution Analysis (MRA)	Z. Liu, 1999 [26]
Multi-frequency EC	Image Pyramid	M. Mina, 1996 [19]

Real/imaginary of Z	DFT/LMMSE	M. Mina, 1996 [20]
Ultrasonic/EC	Image Pyramid	Y. W. Song, 1996 [24]
Multi-frequency EC	NN	J. Yim, 1995 [21]
Ultrasonic/EC	NN	L.Udpa, 1995 [39]
Ultrasonic/EC	LMMSE	J. Yim, 1995 [40]
Multi-frequency EC	MRA	Z. Liu, 1999 [22]

2.6.1 Linear Minimum Mean Square Error (LMMSE)

This optimal approach uses a LMMSE filter to fuse multiple images, which was proposed in [40]. The architecture of the fusion algorithm is given in Figure 2.3.

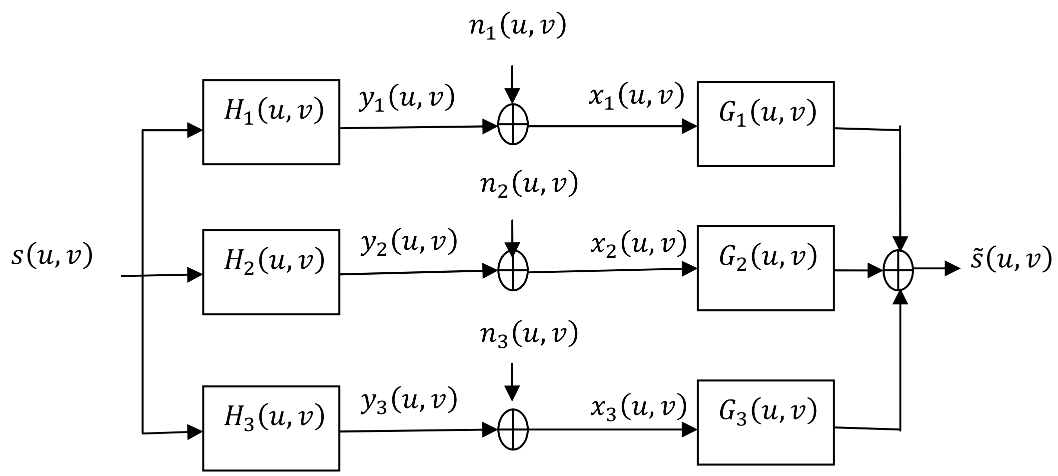


Figure 2.3: Model for Linear signal fusion ([40]).

From system point of view, *s(u,v)* is the input signal to the system with the degradation transfer function $H_i(u,v)$ associated with i^{th} stage, $1 \le i \le N$. From NDE point of view, *s(u,v)* is the perfect response of the original signal in the inspection process. The measurement system acquires signal $x_i(u,v)$ with additive noise $n_i(u,v)$.

Applying a controller/filter $G_i(u,v)$, the output signal is controlled to have a minimum mean square error with the input signal. When there are multiple images the restoration process can be regarded as a fusion operation. $G_i(u,v)$ can be constructed from the spectra of the acquired images as follows.

$$G_j(u,v) = \frac{\sqrt{S_s(u,v)S_{xj}(u,v)}}{\sum_{i=1}^{N} S_{xi}(u,v)} \qquad 1 \leq j \leq N \tag{2.1}$$

$G_j(u,v)$ is the j^{th} filter, $S_s(u,v)$ is the Laplace transform of the original signal $s(u,v)$, and $S_{xj}(u,v)$ is the Laplace transform of the j^{th} acquired image.

The spectrum of the original signal is not available, so an approximation can be used [40] i.e.

$$G_j(u,v) = K\frac{\sqrt{S_{xj}(u,v)}}{\sum_{i=1}^{N} S_{xi}(u,v)} \qquad 1 \leq j \leq N \tag{2.2}$$

Where, K is estimated spectrum which can be estimated by using the coefficients of Fourier decomposition of the signal. This algorithm uses the ultrasonic C-scan images and C-scan eddy current images, no specific evaluation on the quality of the results were available in the literature.

2.6.2 Neural Networks (NN) Fusion

An attempt to fuse eddy current and ultrasonic images, and other to fuse Multi-frequency eddy current images are proposed as in [21], and [35]. Networks that were

evaluated for implementing the fusion algorithm include MLPs as well as RBF networks.

The MLP network consists of a set of simple nonlinear processing elements that are arranged in layers and connected via weights. The network is usually trained using an appropriate algorithm such as back propagation algorithm and a set of exemplars to estimate the interconnection weights.

In RBF network, two layers were employed. The output nodal values are a linear combination of the basis functions that are calculated by the hidden layer nodes. A variety of basis functions can be employed. The most common basis function that is employed is a Gaussian function.

The results reported for the above algorithms indicate that the fusion of ultrasonic image and eddy current image can increase the reliability of inspection. The MLP-based algorithm is sensitive to the choice of exemplars during the training phase, and sometimes generates a result which is biased either towards the ultrasonic or eddy current image. The RBF-based system fuses the image inputs smoothly reflecting information from both input images. The noise in the ultrasonic image was reduced by the fusion, and output image also offers good resolution.

2.6.3 Multi-Resolution Analysis (MRA) Fusion

In this approach, the input NDE image is decomposed into a set of spatial frequency band pass sub-images. The sub-band images are computed by convolving and sub-sampling operations, as presented in [22], [25] and [37]. The procedure for multi-resolution image fusion is shown in Figure 2.4.

The multi-resolution analysis fusion techniques include the image pyramid approaches and wavelet based approaches. Different implementations of multi-resolution fusion are presented in Table. 2.2, and discussed next.

2.6.3.1 Laplacian Pyramid

Burt and Adelson proposed Laplacian pyramid in1983 [41]. The pyramid can be used for image compression and processing. First, the Gaussian pyramid should be introduced here. Gaussian pyramid introduces a blurring operation, e.g. low-pass filtering. Two operation involved are the EXPAND and REDUCE. The relation between two sub-images G_l and G_{l-1} at level *l* and *l-1* is:

$$G_l = REDUCE\ (G_{l-1}) \tag{2.3}$$

For levels $0 < l < K$ and nodes $i, j, 0 \leq i \leq C_l, 0 \leq j \leq R_l, (R_l, C_l)$ here refer to the size of the image at level *l* there is:

$$G_l(i,j) = \sum_{m=-2}^{2} \sum_{n=-2}^{2} \omega(m,n) G_{l-1}(2i+m, 2j+2) \tag{2.4}$$

The coding processing can also be achieved by applying a set of equivalent weighting functions. A function called the EXPAND as the reverse of REDUCE can be defined. Its effect is to expand a (*M* + *1*) by (*N* + *1*) array into a (*2M* + *1*) by (*2N* + *1*) array. Let $G_{l,k}$ be the result of expanding G_l *k* times. Then there are:

$$G_{l,k} = EXPAND\left(G_{l,k-1}\right) \tag{2.5}$$

$$G_{l,k}(i,j) = 4 \sum_{m=-2}^{2} \sum_{n=-2}^{2} \omega(m,n) G_{l,k-1}\left(\frac{i-m}{2}, \frac{j-n}{2}\right) \tag{2.6}$$

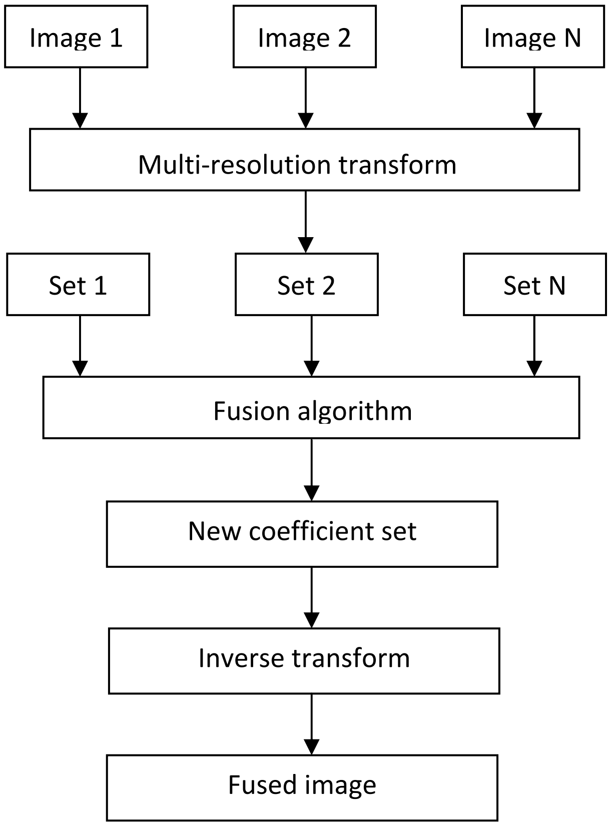


Figure 2.4: Procedure for multi-resolution image fusion ([1]).

Table 2.3: MRA based image fusion algorithms.

MRA Method	Algorithm	Rule of fusion
Gaussian pyramid	Sequence of images in which each member of the sequence is a low pass filtered version of its predecessor	
Laplacian pyramid	It is a set of band pass images, in which each is a band pass filtered copy of its predecessor	-Coefficient selection based on maximum absolute value. -Coefficient selection or average based on salience and match measure.
Ratio of low pass pyramid	Every level the image is the ratio of two successive levels of the Gaussian pyramid	Coefficient selection based on maximum absolute contrast.
Discrete wavelet transform (DWT)	Images decomposed via wavelet transform, after applying the rule of fusion,	-Selection based on choosing the maximum absolute

	then inverse discrete wavelet transform is found	values. -Or an area based maximum energy
Shift invariant discrete wavelet transform (SIDWT)	SIDWT obtained using àtrous algorithm so the process of fusion is independent of the location of an object in the image	Same as in DWT.

Only terms for which $\frac{i-m}{2}$ and $\frac{j-n}{2}$ are integers are included in this sum in (2.6). Obviously, if G_l is expanded l times, an image with the same size as the original one comes out. The pyramid-generating kernel used here is a separable weighting pattern:

$$\omega = \{0.0625, 0.250, 0.375, 0.250, 0.0625\} \quad (2.7)$$

It should be noted that the kernel function has four constrain [42] as:

1. Normalization$\sum_{i=-m}^{m} \omega(i) = 1$.
2. Symmetry $\omega(x) = \omega(-x)$ for all x.
3. Unimodal $\omega(x_1) \geq \omega(x_2) \geq 0 \; for \; 0 \leq x_1 \leq x_2$.
4. Equal contribution$\sum_{i=-m}^{m} \omega(j + ir) = constant \; (= 1/r) \; for \; all \; j, 0 \leq j \leq r$.

For above kernel function ω, m equals to 2. So we can get a 5-by-5 2D filter $\omega(m, n)$.

$$L_l = G_l - EXPAND \; (G_{l+1}) \; for \; 0 \leq l \leq K \quad (2.8)$$

Since there is no G_{K+1}, we define $L_K = G_K$

Gaussian pyramid is a set of low-pass filtered copies of the original image while Laplacian pyramid is a set of band-pass filtered copies of the image. The sequence

images of Laplacian pyramid are error images between two levels of the Gaussian pyramid. So the Laplacian pyramid is also called difference of low-pass pyramid.

Image pyramid thus consists of a set of low pass (Gaussian pyramid) or band pass (Laplacian pyramid) copies of an image, each copy representing pattern information of a different scale. Typically in an image pyramid every level is a factor two smaller as its predecessor.

2.6.3.2 Ratio of Low Pass Pyramid

The ratio of low pass pyramid is defined as introduced by Toet [43] as:

$$R_l = \frac{G_l}{EXPAND(G_{l+1})} \; for \; 0 \leq l \leq K \; also \; R_K = G_K \tag{2.9}$$

This is also based on the Gaussian pyramid. The perceptually important details are revealed by this kind of representation. It can be found from the definition that the pixel value of the expanded version of sub-images cannot be zero. As defined above, every level is the radio of two successive levels in the Gaussian pyramid. The pyramid is first used to enhance the image contrast during the reconstruction procedure. The fusion rule in pyramid fusion methods is the maximum selection rule.

2.6.3.3 Wavelet Fusion

Multi-resolution analysis using wavelet transforms allows decomposing images into a set of new images with coarser and coarser spatial resolution (approximation images). The discrete approach of the wavelet transform mainly can be performed using two algorithms; discrete wavelet transform (DWT) also called decimated algorithm, and

shift invariant discrete wavelet transform (SIDWT) called un-decimated discrete wavelet transform:

1) Decimated Algorithm: It is a fast DWT algorithm based on a multi resolution dyadic scheme that allows to decompose an image LL^i, into an approximation image LL^{i+1} and three detail coefficient images, LH^{i+1}, HL^{i+1}, and HH^{i+1}, where i is the level of the decomposition. If the original image LL^i has C columns and R rows, the approximation and the wavelet coefficient images obtained applying this multi-resolution decomposition have C/2 columns and R/2 rows.

Figure 2.5 show the decomposition procedure of the image by wavelet. The computation of the approximation and the detail coefficients is accomplished with a pyramidal scheme based on convolutions along rows and columns with one-dimensional filters followed by a sub-sampling or decimation operation as illustrated in Figure 2.6. When the multi-resolution wavelet decomposition process is inverted, the original image LL^i can be reconstructed exactly from an approximation image LL^{i+1}, and the detail coefficients , LH^{i+1}, HL^{i+1}, and HH^{i+1}, applying an up-sampling or oversampling process followed by filtering. Both decomposition and reconstruction filters have to be quadrature mirror in order to satisfy constraints inherent to a perfect reconstruction of the original image. To get an image fusion, wavelet decomposition is applied for both images needed to be fused. Then integrate these decomposition coefficients according to certain fusion rule as discussed next to produce a composite representation. An inverse discrete wavelet transform is applied to get the fused image.

The wavelet base fusion technique can reduce color distortion. Furthermore, the down sampling process may cause shift variation, which increases the distortion in the fused images.

2) Un-decimated Algorithm: This algorithm is based on the idea of no decimation. It is a redundant wavelet transform algorithm based on a multi-resolution dyadic scheme accomplished not with a pyramidal scheme but with a parallelpipedic scheme. As shown in Figure 2.7, the original image is decomposed as into four coefficients as in DWT but without decimation.

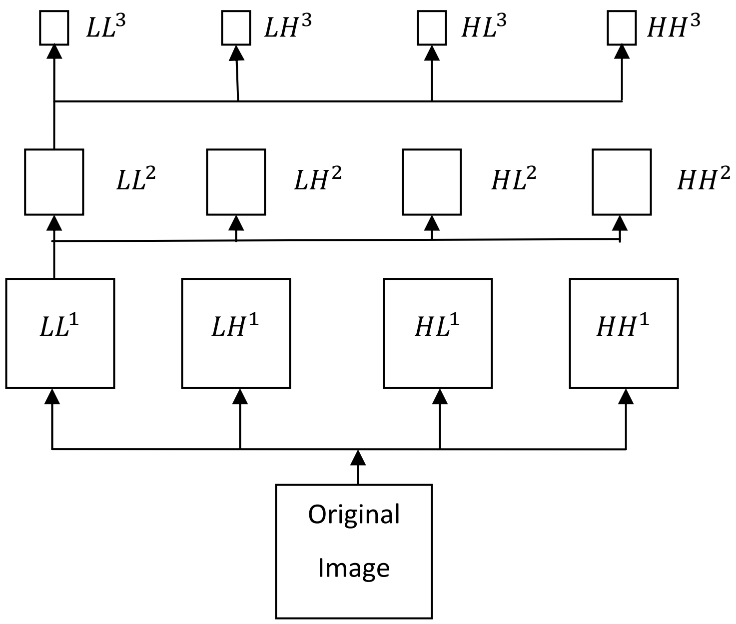


Figure 2.5: The decomposition procedure of the image by DWT.

In contrast to the decimated, the un-decimated algorithm allows shift-invariant discrete wavelet decomposition. All the approximation and wavelet coefficient images obtained by applying this algorithm have the same number of columns and rows as the original image thus such decomposition is highly redundant.

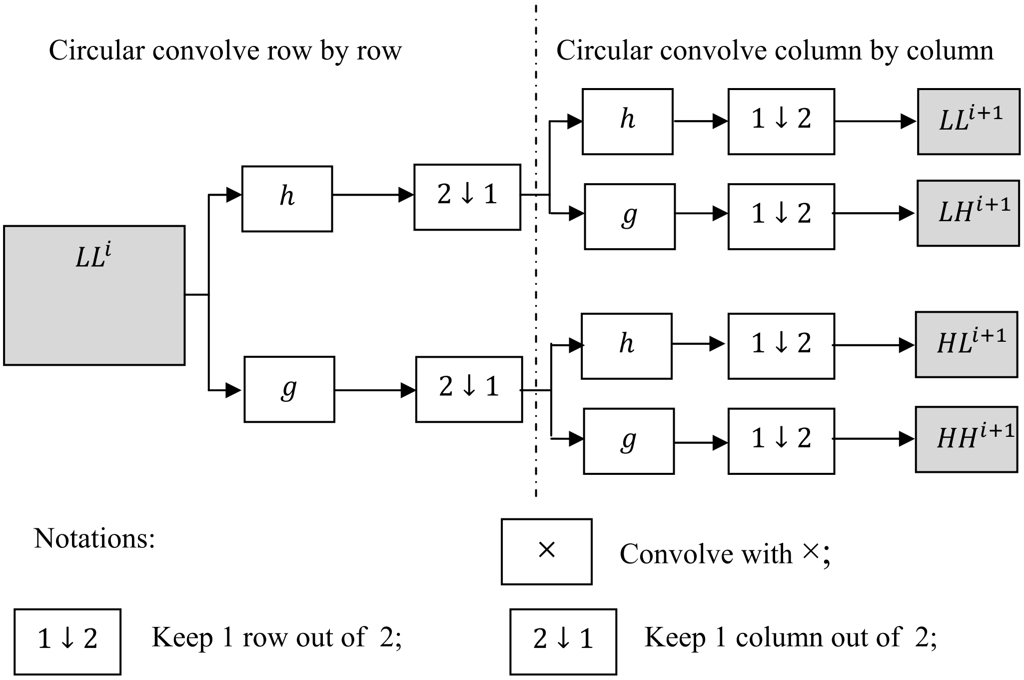


Figure 2.6: One stage 2-D DWT decomposition ([44]).

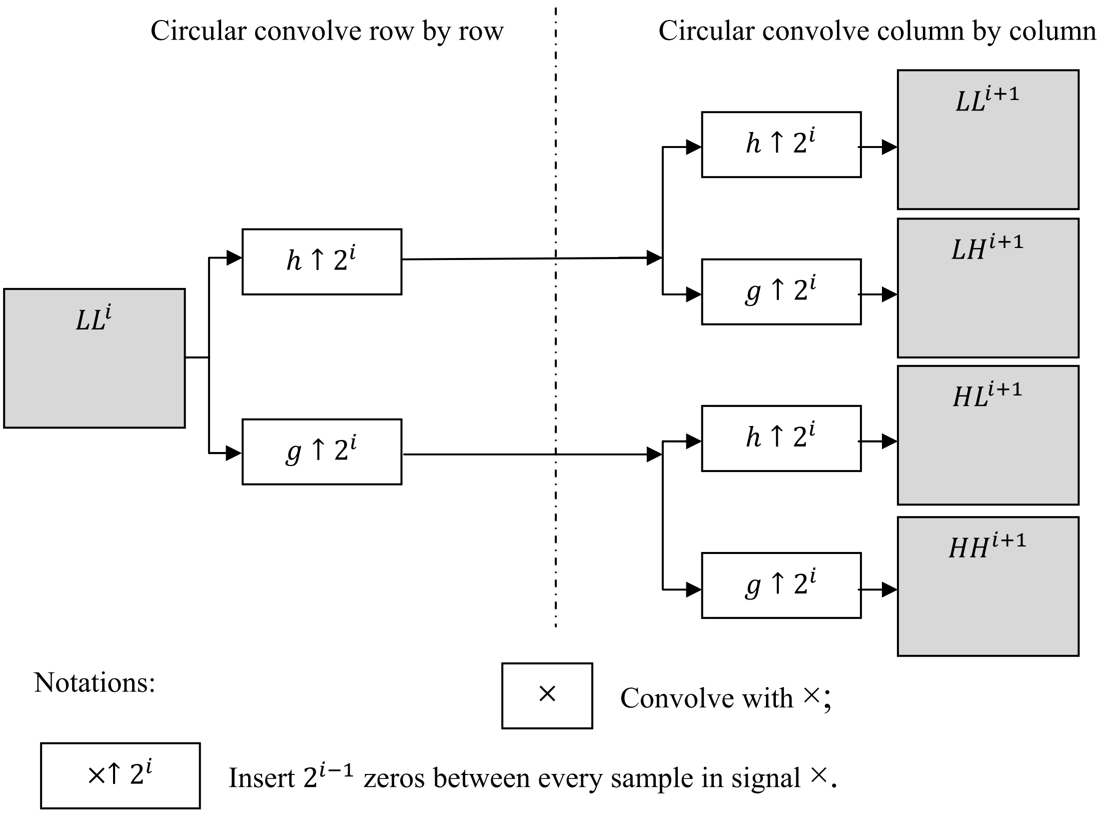


Figure 2.7: One stage 2-D SIDWT decomposition ([44]).

The practical implementation of this algorithm is similar to that of the decimated one but in this case, the sub-sampling or decimation operation is suppressed and the decomposition and reconstruction filters are up-sampled inserting zeros between its coefficients with a step 2^i.

Based on Li et al [45] the performance of the SIDWT based algorithm outperforms the DWT based fusion algorithms.

2.6.3.4 Wavelet Image Fusion Rules

There are several rules, which can be used for selecting the wavelet packet coefficients for image fusion. The most frequently used fusion rules are:

1- Maximum frequency rule. It selects the coefficients with the highest absolute value. The high values indicate salient features like edges and are thus incorporated into the fused image. This rule is applied at all resolutions under consideration.

2- Weighted average rule. It generates a coefficient via a weighted average of the two images' coefficients. The weighting coefficients are based on the correlation between the two images.

3- Standard deviation rule. It calculates an activity or energy measure associated with a pixel. A decision map is created, which indicates the source image from which the coefficient has to be selected.

4- Window based verification rule. It creates a binary decision map to choose between each pair of coefficients using a majority filter.

In the MRA methods listed in table 2.3, the most popular rules is the maximum absolute value selection, where the large value is retained in the new coefficient set, because it corresponds to the image feature such as lines, edges and boundaries. Also

it can be the absolute value, the contrast value, the activity measure, or the local oriented energy at a certain pixel.

The SNR was improved through the fusion of MF-ET C-scan as in [22]. In [37] it was argued that the fusion of ultrasonic, radiographic and shearographic images facilitate the further interpretation and classification procedure.

CHAPTER 3

EDDY CURRENT (EC) INSPECTION MODALITIES

3.1 Introduction

Eddy current tests can be made on all materials which are electrically conducting. They include the sizing of surface and sub surface cracks, measurements of thicknesses of metallic plates and non-metallic coatings on metal substrates, assessment of corrosion and measurement of electrical conductivities and magnetic permabilities. An important advantage of eddy current over other methods such as ultrasonic, magnetic particle, is that there is no need for physical contact with the surface of the object being tested, and surface preparation is usually not necessary, other advantage include simplicity, versatility, high sensitivity, high speeds of testing and it can be performed through normal paint [46].

Eddy current testing technique works on the principal of electromagnetic induction. In this technique, coil (also called probe or sensor) is excited with sinusoidal alternating current to induce eddy current in an electrically conducting material such as stainless steel, aluminum etc. being tested, as depicted in Figure 3.1. The change in coil impedance that arises due to distortion of eddy currents at regions

of discontinuities and associated magnetic flax linkages is measured and correlated with the cause producing it i.e. discontinuities. The locus of impedance change formed during the movement of an eddy current probe coil over a test material having a defect is called an eddy current signal.

The peak to peak amplitude of the eddy current signal provides information about the defect severity. The phase angle of the eddy current signal with respect to a known reference (light – off) provides information about the defect location or depth.

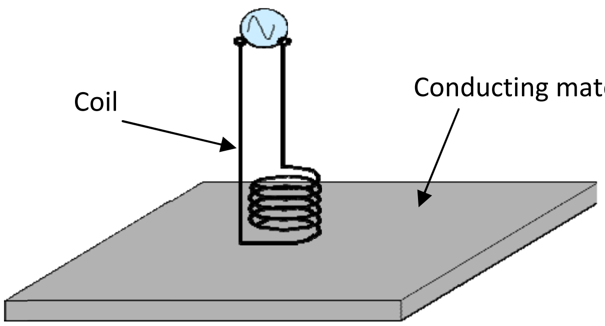


Figure 3.1: Eddy current inspection.

Defects that cause maximum perturbation to eddy current flow produce large eddy current response (signal amplitude) and hence detected with high sensitivity. Conversely, defects that are parallel to eddy current flow may not produce significant change in coil impedance and as a result they produce a weak response, i.e. detected with poor sensitivity.

Eddy current density in a material is not uniform in the thickness (depth) direction. It is greatest on the material surface and decreased continuously with depth (skin effect) as illustrated in Figure 3.2. Thus, in order to detect very shallow detects (cracks, flows) in a material and also to measure thickness of this sheets, very high frequencies are to be used. Similarly, in order to detect subsurface defects and to test

highly conductive magnetic thick materials, low frequencies are to be used [47], and [48].

This technique is employed in all types of engineering industries, especially space, nuclear, defenses, power, chemical, and petrochemical industries.

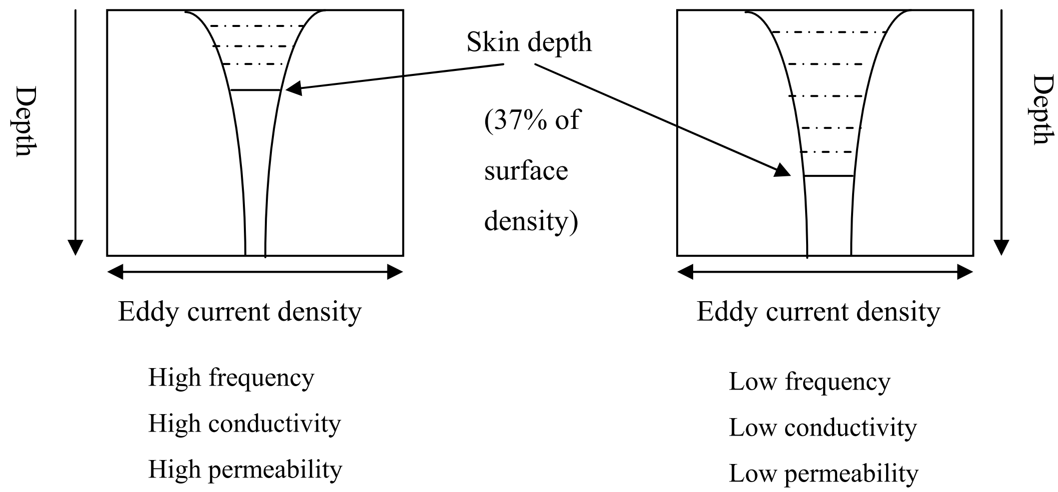


Figure 3.2: Eddy current density.

Since eddy current methods for nondestructive testing rely for their operation on the interaction of induced alternating currents and fields with defects to produce noticeable changes in search coil impedance, it needs a solution for this interaction phenomenon. To date, analytical solution for such phenomena has been largely ineffective in providing a model suitable for the basis of a general defect characterization scheme because of the inherent complexity of the field equation describing the phenomena.

There are many several techniques in solving filed problems. These techniques can be classified as experimental, analytical, or numerical. Experimental are expensive time consuming, sometimes hazardous, and usually do not allow much flexibility in parameter variation. However every numerical method involves an

analytic simplification to the point where it is easy to apply the numerical method. Until the 1940s, most of electromagnetic (EM) problems were solved using the classical methods of separation of variables and integral equation solutions [49]. Besides the fact that a high degree of ingenuity, experience, and effort were required to apply those methods, only a narrow range of practical problems could be investigated due to the complex geometries defining the problems.

Numerical solution of EM problems started in 1960s with the availability of modern high speed digital computers. Since then considerable effort has been expended on solving practical, complex EM related problems for which closed form analytical solutions are either intractable or do not exist. The numerical approach has the advantage of allowing the actual work to be carried out by operators without knowledge of higher mathematics or physics.

The rest of this chapter is organized as follows. An overview of the analytical formulation of EC inspection is described in section 3.2. In section 3.3, compressions of the computational methods that can be used in solving eddy current problem are presented. The selected technique will be covered in section 3.4, and 3.5.

3.2 Analytical Formulation

Most of study in EC modeling limited their comments to the intermediate frequency range where diffusion equations can be used to describe the behavior of impressed and induced currents and fields, thus avoiding discussion of theoretical modeling developments associated with magneto static's (active and residual) leakage fields at the lowest end of the frequency spectrum and pulsed eddy current and microwave methods at the higher frequency ranges.

It is not surprising that the analytical solution of EC inverse problem have been slow in developing for their operation on an alternating current excitation that induces secondary currents and fields in the specimen undergoing inspection. Defects in the specimen cause changes in both induced currents and fields, which result in measurable impedance variations of the search coil. The very nature of this NDE technique leads in general to three dimensional, nonlinear partial differential equations with very awkward boundary conditions, if the probe is moving the solution are functions of both time and position. Non linearity occur wherever specimen properties, such as conductivity and permeability, are non linear functions of excitation. The awkward boundary conditions arise because of the rather arbitrary nature of practical defect shapes.

Eddy current testing works on the principals of electromagnetic induction as stated before and hence, EC phenomena are governed by the following Maxwell's equations, neglecting the displacement current.

$$\boldsymbol{\nabla} \times \boldsymbol{H} = \boldsymbol{J} \tag{3.1}$$

$$\boldsymbol{\nabla} \times \boldsymbol{E} = -\frac{\partial \boldsymbol{B}}{\partial t} \tag{3.2}$$

$$\boldsymbol{\nabla} \cdot \boldsymbol{B} = 0 \tag{3.3}$$

$$\boldsymbol{\nabla} \cdot \boldsymbol{D} = \rho \tag{3.4}$$

Where

$\boldsymbol{\nabla} \times$ = curl operator

$\nabla\cdot$ = divergence operator

$\boldsymbol{H}$ = magnetic field intensity vector

$\boldsymbol{J}$ = total current density vector

t = time

$\boldsymbol{E}$ = electric field intensity vector

$\boldsymbol{B}$ = magnetic flux density vector

$\boldsymbol{D}$ = electric flux density vector

The constitutive equations (no permanent magnets).

$$\boldsymbol{H} = \boldsymbol{\nu B} \ \ \boldsymbol{or} \ \boldsymbol{B} = \boldsymbol{\mu H} \tag{3.5}$$

$$\boldsymbol{J} = \boldsymbol{\sigma E} \quad , \quad \boldsymbol{D} = \boldsymbol{\varepsilon E} \tag{3.6}$$

Define the material properties where the reluctivity ***v***, $\boldsymbol{\mu}$ magnetic permeability, $\boldsymbol{\varepsilon}$ permittivity, and conductivity $\boldsymbol{\sigma}$ may be field dependent and/or vary in space.

$\boldsymbol{\mu}$ may be a function of temperature or field. Specifically, if it is only a function of temperature,

$$\boldsymbol{\mu} = \mu_0 \begin{bmatrix} \mu_{rx} & 0 & 0 \\ 0 & \mu_{ry} & 0 \\ 0 & 0 & \mu_{rz} \end{bmatrix} \tag{3.7}$$

where

μ_0 = permeability of free space

μ_{rx} = relative permeability in the x-direction

In case of isotropic material,

$$\boldsymbol{\mu} = \mu_h \begin{bmatrix} 1 & 0 & 0 \\ 0 & 1 & 0 \\ 0 & 0 & 1 \end{bmatrix} \tag{3.8}$$

where

μ_h = permeability derived from the BH curve

If $\boldsymbol{\mu}$ is function of both field and temperature , e.g.

$$\boldsymbol{\mu} = \begin{bmatrix} \mu_h & 0 & 0 \\ 0 & \mu_0\mu_{ry} & 0 \\ 0 & 0 & \mu_h \end{bmatrix} \tag{3.9}$$

The conductivity, and permittivity in general,

$$\boldsymbol{\sigma} = \begin{bmatrix} \sigma_{xx} & 0 & 0 \\ 0 & \sigma_{xx} & 0 \\ 0 & 0 & \sigma_{zz} \end{bmatrix} \tag{3.10}$$

$$\boldsymbol{\varepsilon} = \begin{bmatrix} \varepsilon_{xx} & 0 & 0 \\ 0 & \varepsilon_{xx} & 0 \\ 0 & 0 & \varepsilon_{zz} \end{bmatrix} \tag{3.11}$$

A typical eddy current phenomena is illustrated in Figure 3.3. It consist of eddy current region with nonzero conductivity (Ω_1) and free of eddy currents region which contain source currents (Ω_2).

The union of (Ω_1), and (Ω_2) is denoted (Ω). The boundary of (Ω_2) and hence (Ω) is divided in to two parts according to the types of boundary conditions, on Γ_B the normal component of magnetic flux density is prescribed, whereas on Γ_H the tangential components of magnetic field intensity is given. Both boundary conditions assumed to be homogeneous. The boundary of eddy currents region (Ω_1) denoted by (Γ_{12}) represent the interface between the conducting and non conducting regions.

From the well-known boundary conditions the normal component of magnetic flux density and the tangential component of magnetic field intensity are continuous.

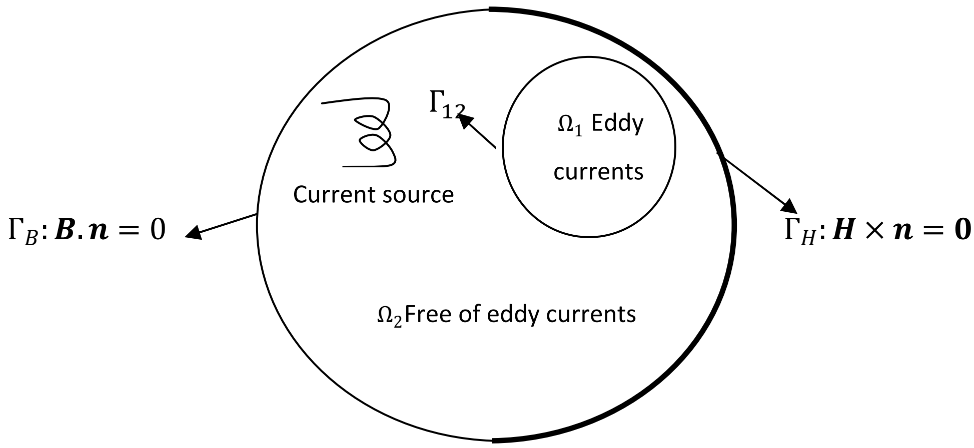


Figure 3.3: Typical eddy current problem ([50]).

Rewriting the equations and boundary conditions in each region as follows:

In Ω_1

$$\boldsymbol{\nabla} \times \boldsymbol{H} - \boldsymbol{\sigma E} = \boldsymbol{0} \tag{3.12}$$

$$\boldsymbol{\nabla} \times \boldsymbol{E} + \frac{\partial \boldsymbol{B}}{\partial t} = \boldsymbol{0} \tag{3.13}$$

$$\boldsymbol{\nabla} . \boldsymbol{B} = 0 \tag{3.14}$$

In Ω_2

$$\boldsymbol{\nabla} \times \boldsymbol{H} = \boldsymbol{J_s} \tag{3.15}$$

$$\boldsymbol{\nabla} . \boldsymbol{B} = 0 \tag{3.16}$$

On Γ_B

$$\boldsymbol{B}.\boldsymbol{n} = 0 \tag{3.17}$$

On Γ_H

$$\boldsymbol{H} \times \boldsymbol{n} = \boldsymbol{0} \tag{3.18}$$

On Γ_{12}

$$\boldsymbol{B_1}.\boldsymbol{n_1} + \boldsymbol{B_2}.\boldsymbol{n_2} = 0 \tag{3.19}$$

$$\boldsymbol{H_1} \times \boldsymbol{n_1} + \boldsymbol{H_2} \times \boldsymbol{n_2} = \boldsymbol{0} \tag{3.20}$$

where

$\boldsymbol{J}_s$ = given source current density

$\boldsymbol{n}$ = outer normal on the surface

1, 2 refer to regions Ω_1, and Ω_2 respectively

The above equations ensure the uniqueness of $\boldsymbol{B}$ and $\boldsymbol{E}$ [50].

A solution can be obtained by introducing potential which allow the magnetic field $\boldsymbol{B}$ and the electric field $\boldsymbol{E}$ to be expressed in term of magnetic vector potential $\boldsymbol{A}$ and electric scalar potential V as:

$$\boldsymbol{B} = \boldsymbol{\nabla} \times \boldsymbol{A} \tag{3.21}$$

$$\boldsymbol{E} = -\frac{\partial \boldsymbol{A}}{\partial t} - \boldsymbol{\nabla} V \tag{3.22}$$

Substitute in equations (3.12), and (3.15) we can end up with

In Ω_1

$$\boldsymbol{\nabla} \times \boldsymbol{\nu}\boldsymbol{\nabla} \times \boldsymbol{A} + \boldsymbol{\sigma}\frac{\partial \boldsymbol{A}}{\partial t} + \boldsymbol{\sigma}\boldsymbol{\nabla}V = \boldsymbol{0} \tag{3.23}$$

In Ω_2

$$\boldsymbol{\nabla} \times \boldsymbol{\nu}\boldsymbol{\nabla} \times \boldsymbol{A} = \boldsymbol{J_s} \tag{3.24}$$

The boundary conditions (3.17) and (3.18) are formulated as:

On Γ_B

$$\boldsymbol{n}.\boldsymbol{\nabla} \times \boldsymbol{A} = \boldsymbol{0} \tag{3.25}$$

On Γ_H

$$(\boldsymbol{\nu}\boldsymbol{\nabla} \times \boldsymbol{A}) \times \boldsymbol{n} = \boldsymbol{0} \tag{3.26}$$

and the interface conditions on Γ_{12} are

$$\boldsymbol{n_1}.\boldsymbol{\nabla} \times \boldsymbol{A_1} + \boldsymbol{n_2}.\boldsymbol{\nabla} \times \boldsymbol{A_2} = \boldsymbol{0} \tag{3.27}$$

$$(\boldsymbol{\nu_1}.\boldsymbol{\nabla} \times \boldsymbol{A_1}) \times \boldsymbol{n_2} + (\boldsymbol{\nu_2}\boldsymbol{\nabla} \times \boldsymbol{A_2}) \times \boldsymbol{n_2} = \boldsymbol{0} \tag{3.28}$$

In order to solve the above equations analytically, simplifying approximations are made with regard to the number of dimensions, linearity or material properties, symmetry, boundary conditions, and in case if there is a defect the shape of defect. Even with such simplifying assumptions the mathematics is at best complex and the results tend to be limited to a single geometry. So numerical modeling is invoked for applications where there is no general analytical solution.

3.3 Numerical Techniques

Numerical models are mathematical descriptions of a physical process, as in EC technique, expressed in the form of algebraic equations or more usefully, computer programs. The first step for developing a numerical model is to formulate a differential equation that describes all the interactions, which has been done in section 3.2. This equation is solved in a specific region with a set of boundary conditions for a desired variable.

A necessary prerequisite for the development of a numerical model in EC is to predict the electromagnetic field/defect interactions. Such models can be used to understand and study those testing conditions governing the EC problem, e.g. impedance change in a probe coil due to a defect. Using such models it would be possible to simulate and study those testing conditions, which are difficult to repeat many times in the laboratory. Having simulated the inspection problem on the computer it is relatively a simple task to calculate the effects of each variable on the impedance for example. There are many numerical techniques used in solving the EC problem.

Numerical methods used to solve such problem are the finite difference method (FDM) and the finite element method (FEM). Other numerical methods include boundary element and volume integral techniques. The most widely used numerical techniques to solve EC problems are the FEM and FDM, each of those two methods have its advantages and disadvantages. In the following subsections a brief introduction of FEM and FDM are given.

3.3.1 Finite Difference Method

The finite difference method is the oldest technique used to deal with a system of differential equations [3]. The FDM techniques are based upon approximations which permit replacing differential equations by finite difference equations. These finite difference approximation are algebraic in form, they relate the value of the dependent variable at a point in the solution region to the values at some neighboring points. Thus a finite difference solution basically involves three steps:

1. Dividing the solution region into a grid of nodes.

2. Approximating the given differential equations by finite difference equivalent that relates the dependent variable at the solution region to its values at the neighboring points.

3. Solving the difference equations subject to the prescribed boundary conditions and / or initial conditions.

3.3.2 Finite Element Method

The finite element method (FEM) is a numerical technique, well suited to digital computers, which can be applied to solve problems in many fields, such as structure, electromagnetic, solid mechanics, fluid mechanics, heat transfer and vibrations, the procedures to solve problems in each of these fields is similar. The FEM has its origin in the field of structural analysis. Although the earlier mathematical treatment of the method was provided by Courant in 1943, the method was not applied to EM problems until 1968. There are a number of steps in the solution procedure using finite element methods [51].

1. Specifying Geometry - First the geometry of the structure to be analyzed is defined.

2. Specify Element Type and Material Properties - Next, the material properties are defined.

3. Mesh the Object - The structure is broken (or meshed) into small elements. This involves defining the types of elements into which the structure will be broken, as well as specifying how the structure will be subdivided into elements (how it will be meshed).

4. Apply Boundary Conditions and External Loads - Next, the boundary conditions and the external loads are specified.

5. Generate a Solution - Then the solution is generated based on the previously input parameters.

6. Post-processing - Based on the initial conditions and applied loads, data is returned after a solution is processed.

7. Refine the Mesh - Finite element methods are approximate methods and, in general, the accuracy of the approximation increases with the number of elements used. The number of elements needed for an accurate model depends on the problem and the specific results to be extracted from it. Thus, in order to judge the accuracy of results from a single finite element run, you need to increase the number of elements in the object and see if or how the results change.

8. Interpreting Results - This step is perhaps the most critical step in the entire analysis because it requires that the modeler use his fundamental knowledge to interpret and understand the output of the model.

The eight steps mentioned above have to be carried out before any meaningful information can be obtained regardless of the size and complexity of the problem to be solved.

Although the FDM is conceptually simpler and easier to program than the finite element method, FEM is a more powerful and versatile numerical technique for handling problems involving complex geometries and inhomogeneous media [49]. The systematic generality of the method makes it possible to construct general purpose computer programs for solving a wide range of problems; consequently programs developed for a particular discipline have been applied successfully to solve problems in a different field with little or no modification [51].

In this study the finite element FE used to solve the EC problem and hence numerically model the EC phenomena [50-53] for both conventional EC and pulsed eddy current PEC inspections techniques.

Analysis is done under ANSYS environment, using electromagnetic-circuit field coupling analysis [54]. ANSYS multi-physics finite element package is a powerful tool to perform multi-physics analysis. As a result, the realization of the FE for modeling EC is discussed in the next section.

3.4 Eddy Current Finite Element Realizations

There are various ways of setting up the finite element equations, the most used method being the Galerkin form of weighted residual equations [50]. The numerical approximation of the potentials is based on a finite element mesh; the potentials are expanded in terms of shape functions associated with the nodes of this mesh

$$\boldsymbol{A} \approx \sum_{j} A_{xj}N_{Aj}\boldsymbol{e_x} + A_{yj}N_{Aj}\boldsymbol{e_y} + A_{zj}N_{Aj}\boldsymbol{e_z} = \sum_{\boldsymbol{k}} A_k\boldsymbol{N_{Ak}} \tag{3.29}$$

$$V \approx \sum_{j} V_j N_j \tag{3.30}$$

where A_{xj} , A_{yj} , A_{zj} are the three components of the vector potential at node j ; V_j is the scalar potentials at node j ; N_j is the shape function associated with node j that assumes the value of one at this node and the value of zero at any other node. The vector $\boldsymbol{e_x}$, $\boldsymbol{e_y}$,and $\boldsymbol{e_z}$ are the Cartesian unit vectors. The index k assumes three times as many values as j, i.e.

$$A_k = A_{xj}\ or\ A_{yj}\ \ or\ A_{zj} \tag{3.31}$$

$$\boldsymbol{N_k} = N_j\boldsymbol{e_x}\ or\ N_j\boldsymbol{e_y}\ \ or\ N_j\boldsymbol{e_z} \tag{3.32}$$

The basic equation to be solved is of the form:

$$[\,\overline{C}\,]\{\dot{U}\} + [\,\overline{K}\,]\{U\} = \{\bar{J}_i\} \tag{3.33}$$

The terms of equation (3.33) are defined as:

Degrees of freedom

$$\{U\} = \begin{Bmatrix} \{A_e\} \\ \{v_e\} \end{Bmatrix} \tag{3.34}$$

Where:

$\{A_e\}$ = magnetic vector potentials.

$\{v_e\}$ = time integrated electric scalar potential ($v = \int V dt$)

Coefficient matrices

$$[\overline{K}] = \begin{bmatrix} [K^{AA}] \\ [K^{vA}] \end{bmatrix} \tag{3.35}$$

$$[K^{AA}] = [K^L] + [K^N] + [K^G] \tag{3.36}$$

$$[K^L] = \iiint (\nabla \times [N_A]^T)^T \, [\nu]\big(\nabla \times [N_A]^T - [N_A][\sigma](\{V\} \times \nabla \times [N_A]^T)\big) d(vol) \tag{3.37}$$

$$[K^N] = 2 \iiint \frac{d\nu_h}{d(|B|^2)} \big(\{B\}^T(\nabla \times [N_A]^T)\big)^T \big(\{B\}^T(\nabla \times [N_A]^T)\big) d(vol) \tag{3.38}$$

$$[K^G] = \iiint (\nabla \cdot [N_A]^T)^T [\nu] \, (\nabla \cdot [N_A]^T) d(vol) \tag{3.39}$$

$$[K^{VA}] = -\iiint (\nabla [N]^T)^T [\sigma] \, \{V\} \times \nabla \times [N_A]^T d(vol) \tag{3.40}$$

$$[\bar{C}] = \begin{bmatrix} [C^{AA}] & [C^{AV}] \\ [C^{AV}] & [C^{VV}] \end{bmatrix} \tag{3.41}$$

$$[C^{AA}] = \iiint [N_A][\sigma] \, [N_A]^T d(vol) \tag{3.42}$$

$$[C^{AV}] = \iiint [N_A][\sigma]\nabla\{N\}^T \, d(vol) \tag{3.43}$$

$$[C^{VV}] = \iiint (\nabla\{N\}^T)^T[\sigma]\nabla\{N\}^T \, d(vol) \tag{3.44}$$

Applied loads

$$\{J_i\} = \begin{Bmatrix} \{J^S\} + \{J^{pm}\} \\ \{I^t\} \end{Bmatrix} \tag{3.45}$$

where

$$\{J^S\} = \iiint \{J_s\}[N_A]^T \, d(vol) \tag{3.46}$$

$$\{J^{pm}\} = \iiint (\nabla \times [N_A]^T)^T\{H_c\} \, d(vol) \tag{3.47}$$

$$\{I^t\} = \iiint \{J_t\}[N_A]^T \, d(vol) \tag{3.48}$$

where:

$[N_A]$ = matrix of element shape functions for $\{A\}$

$$\{A\} = [N_A]^T\{A_e\};\ \{A_e\}^T = \lfloor \{A_{xe}\}^T \quad \{A_{ye}\}^T \quad \{A_{ze}\}^T \rfloor \tag{3.49}$$

$[N]$ = vector of element shape functions for $\{V\}$

$$V = \{N\}^T\{V_e\} \tag{3.50}$$

$\{J_s\}$ = source current density vector.

$\{J_t\}$ = total current density vector (used in case of 2-D analysis only).

vol = volume of the element.

$\{H_c\}$ = coercive force vector.

ν_0 = reluctivity of free space.

$[\nu]$ = reluctivity matrix.

$\frac{d\nu_h}{d(|B|)^2}$ = derivative of reluctivity with respect to the magnitude of magnetic flux squared.

$[\sigma]$ = conductivity matrix.

$\{v\}$ = velocity vector.

The above element matrices and load vectors are for the most general case of a vector potential analysis. Many simplifications can be made depending on the conditions of the specific problem.

In our case the model implements a voltage source applied to the coil. From equation (3.33) the following element matrix is derived [54]

$$\begin{bmatrix} [0] & [0] \\ [C^{iA}] & [0] \end{bmatrix} \begin{Bmatrix} \{\dot{A}\} \\ 0 \end{Bmatrix} + \begin{bmatrix} [K^{AA}] & [K^{Ai}] \\ [0] & [K^{ii}] \end{bmatrix} \begin{Bmatrix} \{A\} \\ \{i\} \end{Bmatrix} = \begin{Bmatrix} \{0\} \\ \{V_0\} \end{Bmatrix} \tag{3.51}$$

where

$\{A\}$ = nodal magnetic vector potential vector.

$\{i\}$ = nodal electric current vector.

$\{V_0\}$ = applied voltage drop vector.

The sub-matrices are defined above and called, the potential stiffness matrix$[K^{AA}]$, resistive stiffness matrix$[K^{ii}]$, the potential-current coupling stiffness matrix$[K^{Ai}]$, and the inductive damping matrix$[C^{iA}]$.

3.5 Computational Modeling Implementation of Eddy Current

Three dimensional model was built to simulate a coil on top of a metal object with defects as shown in Figure 3.4.

The coil is designed to be of 10-mm outer radius, 5-mm inner radius, and 5-mm height. The object is composed of aluminum with 100-mm radius and 10mm thickness, and the lift-off between the probe and the object is of 1.1-mm. Three cracks are modeled. All cracks have the same cross section of 2mm×2mm that is parallel to the object upper surface. Type I is a surface crack of 5 mm depth. Type II crack is a subsurface crack of 3mm depth and is present 1 mm under the upper surface of the object. Type III crack is of 1 mm depth and is present at 3 mm from the top surface. Figure 3.5 show a schematic of the simulated model.

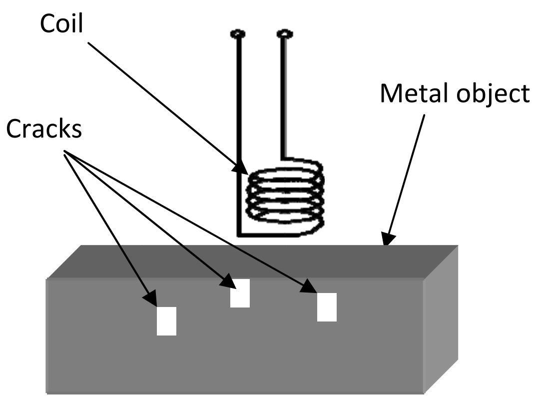
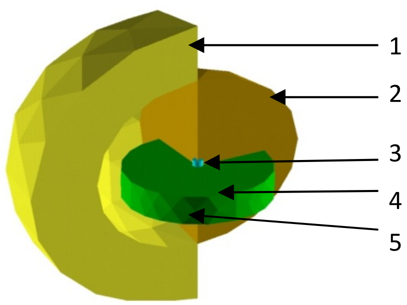


Figure 3.4: Schematic plot for the model to be simulated.

The ANSYS elements library consist of more than 100 different element formulations or types each has different features and applications [54]. From this library the elements used are SOLID97, CIRCU124, INFIN111, with different features, briefly discussed next.

SOLID97 models 3-D magnetic fields. The element is defined by eight nodes, and has up to five degrees of freedom per node out of six defined degree of freedoms (DOFs); that is, the magnetic vector potential (*AX, AY, AZ*), the time-integrated electric potential (*VOLT* – classical formulation) or the electric potential (*VOLT* – solenoidal formulation), the electric current (*CURR*), and the electromotive force (*EMF*).



1 – Infinite elements. 2- Air around the model. 3- Probe.
4- Object to be tested. 5- Crack inside the object.

Figure 3.5: Schematic plot for the model.

SOLID97 is based on the magnetic vector potential formulation, and is applicable to the following low-frequency magnetic field analyses: magnetostatics, eddy currents (AC time harmonic and transient analyses), voltage forced magnetic fields (static, AC time harmonic and transient analyses), and electromagnetic-circuit coupled fields (static, AC time harmonic and transient analyses). The element has nonlinear magnetic capability for modeling B-H curves or permanent magnet demagnetization curves. SOLID97 has two formulation options: classical and solenoidal. The solenoidal formulation used in this simulation automatically satisfies

the solenoidal condition by directly solving for current (density) using a coupled current conduction and electromagnetic field solution. The SOLID97 solenoidal option is compatible with CIRCU124 element allowing circuit coupling. This element has brick geometry, this geometry can be formed by defining the same node numbers for many nodes, to form a tetrahedral-shaped element, wedge-shaped element and a pyramid-shaped element as shown in Figure 3.6, this element used to model the probe, object, crack, and air around the model.

CIRCU124 is a general circuit element applicable to circuit simulation. The element may also interface with electromagnetic finite elements to simulate coupled electromagnetic-circuit field interaction, which has been used her. The element has up to 6 nodes to define the circuit component and up to three degrees of freedom per node to model the circuit response. For electromagnetic-circuit field coupling, the element may interface with SOLID97. CIRCU124 is applicable to static, harmonic, and transient analyses. The element used to model the independent currant source also to couple the model with the excitation circuit.

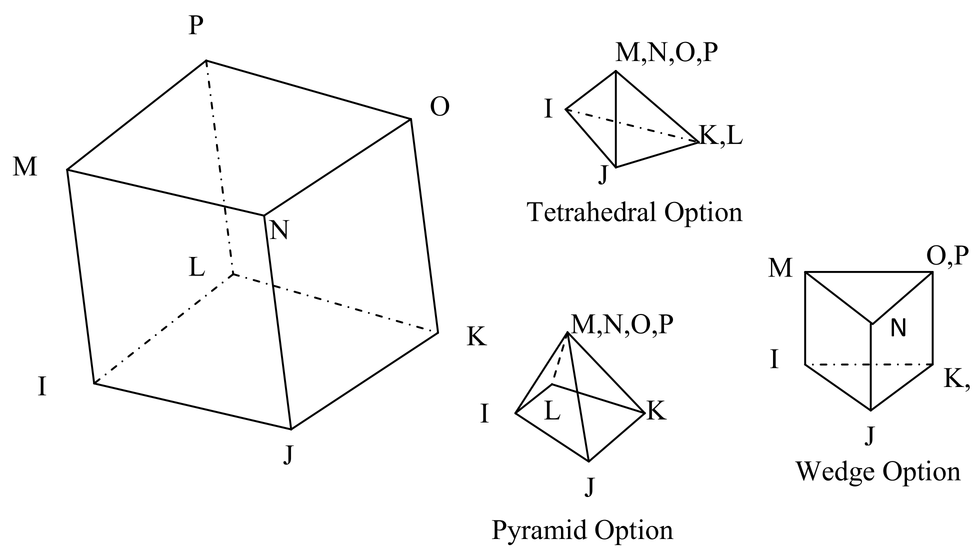


Figure 3.6: SOLID97 element geometry.

INFIN111 is used to model an open boundary of a 3-D unbounded field problem. A single layer of elements is used to represent an exterior sub-domain of semi-infinite extent. This element is defined by either 8 or 20 nodes and has 3-D magnetic vector potential capabilities. It is used to model the open boundary of the model.

After assigning the element attributes and materials property and set mesh controls, the process for generating a mesh of nodes and elements (meshing) is done.

A total number of 117385 elements generated for acceptable accuracy, as in Figure 3.7, the boundary conditions then applied to the exterior INFIN111 elements, and the DOFs, current and volt is coupled for all nodes of the probe. The excitation is applied and the model is solved for various crack positions and also corresponding to various excitation frequencies. Infinite boundary elements are implemented to model the surrounding infinite space. Simulation results were conducted corresponding to the following five inspection frequency values: 100 Hz, 1 kHz, 10 kHz, 100 kHz, and 1M Hz.

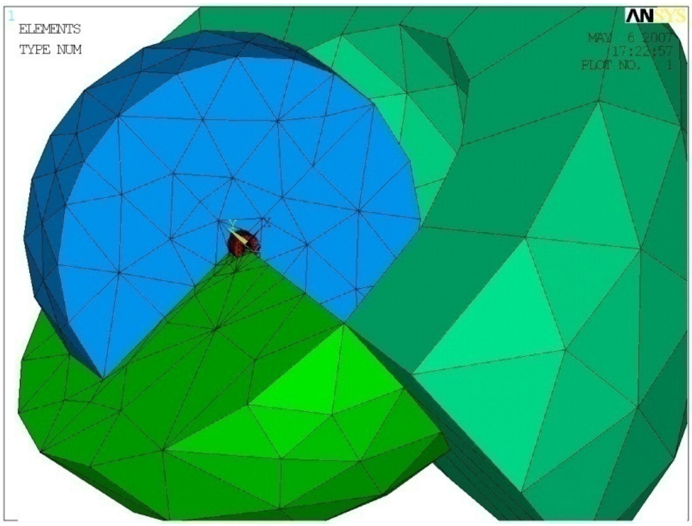


Figure 3.7: Meshed model. (Coarse to be clear).

After the solution has been done and the primary data was produced, in the post-processing stage, the data needed can be derived, in this study the power loss, stored energy, and the flux passing through a closed contour. These derived data was derived as follows:

3.5.1 Power Loss

The r.m.s. power loss is calculated from the equation:

$$P_{rms} = \iiint \rho \left|\tilde{J}_t\right|^2 d(vol) \tag{3.52}$$

where:

P_{rms} = rms power loss.

ρ = material resistivity.

$\tilde{J}_t$ = total current density (complex quantity).

The power loss integrating over the selected element set according to:

$$P_{rms} = \frac{1}{2} Re\left(\sum_{1}^{m}\left(\left([\rho_i]\{\tilde{J}_{ti}\}\right)^* \cdot \{\tilde{J}_{ti}\}\right) vol_i\right) \tag{3.53}$$

where:

m = number of elements.

Re( ) = real component of a complex quantity.

$\{\tilde{J}_{ti}\}$ = total eddy current density vector for element i.

vol_i = element volume.

* = complex conjugate operator.

3.5.2 Energy in a Magnetic Field

For time-harmonic analysis, the r.m.s. stored magnetic energy is calculated as:

$$P_{rms} = \frac{1}{4} Re \iiint \{\tilde{B}\} \cdot \{\tilde{H}\}^* \, d(vol) \tag{3.54}$$

3.5.3 Flux Passing Through a Closed Contour

The flux passing through a surface defined by a closed line contour can be calculated as:

$$\phi = \iint \{B\} \cdot \{n\} d(area) \tag{3.55}$$

where:

ϕ = flux enclosed by the bounding surface.

$\{B\}$ = flux density vector.

$\{n\}$ = unit normal vector.

area = area of the bounding surface.

Equation (3.52) can be rewritten in terms of the definition of the vector potential as:

$$\phi = \iint (\nabla \times \{A\}) \cdot \{n\} d(area) \tag{3.56}$$

Applying Stokes theorem, the surface integral reduces to a line integral of A around a closed contour;

$$\phi = \int \{A\} \cdot \boldsymbol{dl} \tag{3.57}$$

where:

l = length of the bounding contour line.

Sequence values of probe inductance and resistance values are recorded after the post-processing has been done to be arranged to form the harmonic EC images, this point will be discussed in the next chapter.

3.6 Pulsed Eddy Current (PEC)

Conventional eddy current techniques use single frequency sinusoidal excitation and detect flaws as impedance or voltage changes on an impedance plane display with inspectors interpreting the magnitude and phase changes. However, these techniques are sensitive to a variety of parameter as mentioned in the preceding section. To obtain the depth information of defects, multiple frequency measurements have been combined to provide a more rigorous assessment of structural integrity. Pulsed eddy current sensing is a new and emerging technique [48] that has been particularly developed for subsurface flaws. These techniques can work at some distance below the surface (up to 100mm in aluminum) [48].

In PEC techniques the probe's excitation coil is excited with a repetitive broadband pulse, usually a rectangular wave. The resulting transient current through the coil induces transient eddy currents in the test object, which are associated with highly attenuated magnetic pulses propagating through the material. The probe

provides a series of voltage-time data pairs as the induced field decays, and since the produced pulses consist of a broad frequency spectrum, the reflected signal contains important depth information, physically, the field is broadened and delayed as it travels deeper into the highly dispersive material, and flows or other anomalies close to the surface affect the eddy current response earlier than deeper flaws. Peak values, time to maximum values, and time to minimum values have been used for flaw detection and identification.

Typically, a single sensor PEC probe consists of an excitation coil and a pickup coil or a magnetic field sensor, such as an inductive coil or Giant Magneto Resistive (GMR) [55] as shown in Figure 3.8.

3.7 Analysis of Pulsed Eddy Current

PEC is analyzed either using transient time domain analysis or a series of harmonic analysis. In this study a series of harmonic analysis was used because this method provided higher accuracy of amplitude than the time stepping method [56]. And the analysis in frequency domain gives the reliability to investigate effect of using different pulse width for excitation.

Figure 3.9 presents typical excitation pulse in both time and frequency domains. The pulse has a duration of τ=0.25 ms and is repeated every T_0= 1 ms. The bars in Figure 3.9(b) are obtained using fast Fourier transform of the time domain signal and the envelope represent the analytical Fourier spectrum $V(f)$ multiplied by sampling frequency f_S, where $V(f)$ is given as [57]

$$V(f) = \frac{A}{f_p} sinc\left(\frac{f}{f_p}\right) \tag{3.58}$$

where A is the magnitude of the pulse, and $f_p=1/\tau$.

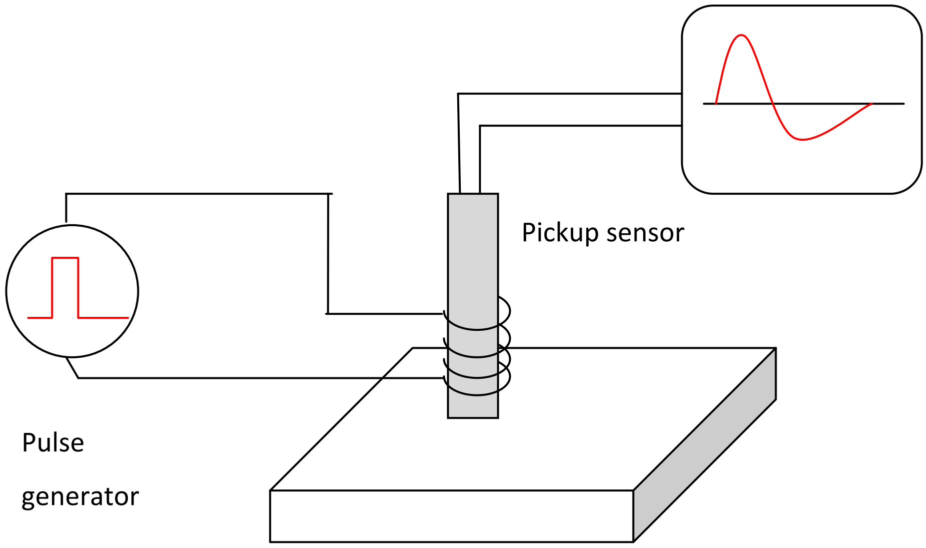


Figure 3.8: Layout of PEC inspection.

It is apparent that most of energy is concentrated in the lower frequency band, and there are repeated nulls in the spectrum. More insight into material characteristics could be obtained by enrichment of the spectrum information available from PEC inspection with information that might available at particular spectrum nodes obtained using harmonic eddy current inspection.

In the harmonic analysis of PEC technique the finite element model already built was with small modifications run to obtain the flux passing through a closed contour ϕ_{FE} using equation (3.55) corresponding to frequencies kf_o where f_o is the inverse of repetition period to and Ke 1, 2, . . . $N/2$, and N is the total number of time or frequency samples. Runs are excluded for frequencies mf_p where f_p is the inverse of pulse period τ and m is an integer. The spectrum of ϕ is obtained for a specified excitation signal as:

$$\emptyset(f) = V(f)\emptyset_{FE}(f) \tag{3.59}$$

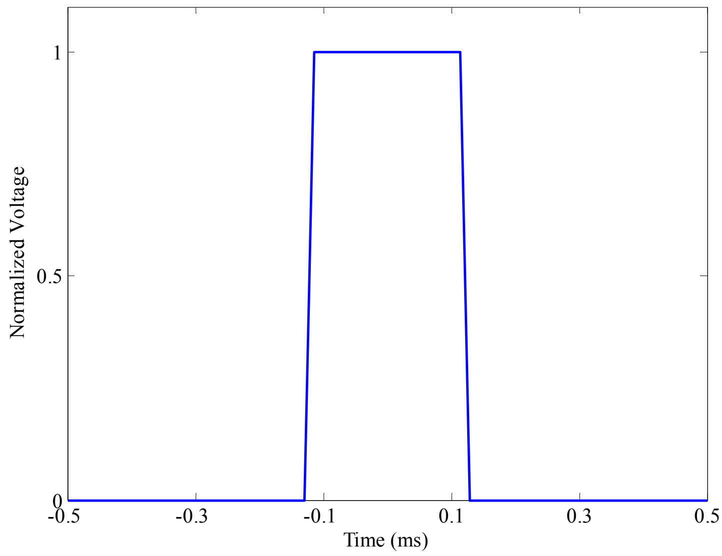
where $V(f)$ as mentioned before is the Fourier transform of the excitation signal.

Inverse Fourier transform is applied to obtain time-domain signals, after taking the derivative of equation (3.59) in frequency domain i.e. multiply it by $-j\omega$, where the negative frequencies results are obtained as the conjugate of the simulation results corresponding frequency.

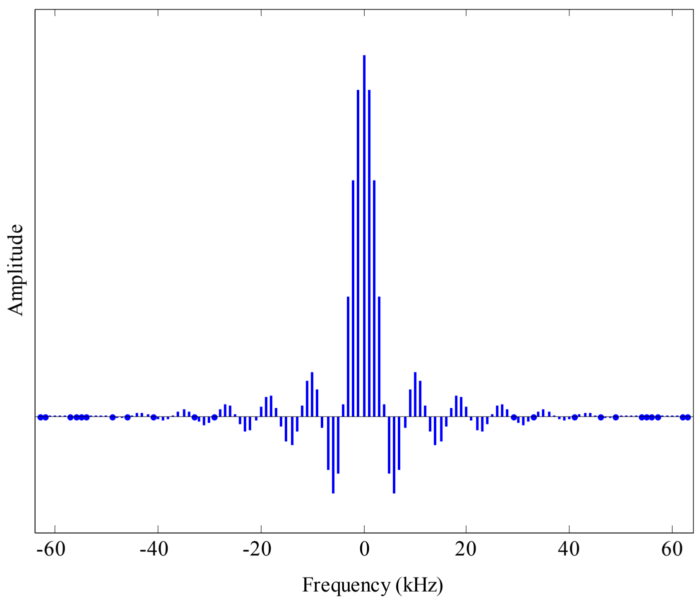
In order to eliminate the effect of mesh the model solved with no cracks and with cracks, then the difference of the picked up signal is taken to represent the effect of crack only.

A number of 64 harmonic analysis runs is performed. Each run takes around 7 minutes and 5 seconds, using a computer equipped with quad-core 3GHz processor. Two loops are included in the post-processing analysis, with diameter values of 1-mm and 4-mm, respectively, centered along the centerline of the coil and placed 1-mm above the specimen.

Sample of the differential response of the picked-up signals are shown in Figures 3.10, 3.11, and 3.12 for cracks I (shallow), II (deeper), and III (deepest) respectively with different horizontal distance between the axis of coil and axis of each crack. From these results, it is clear that the crack near the surface is affected earlier in time, and bigger crack size gives large amplitude.



(a)



(b)

Figure 3.9: Typical PEC excitation pulse in time domain (a) and spectrum of frequency domain (b).

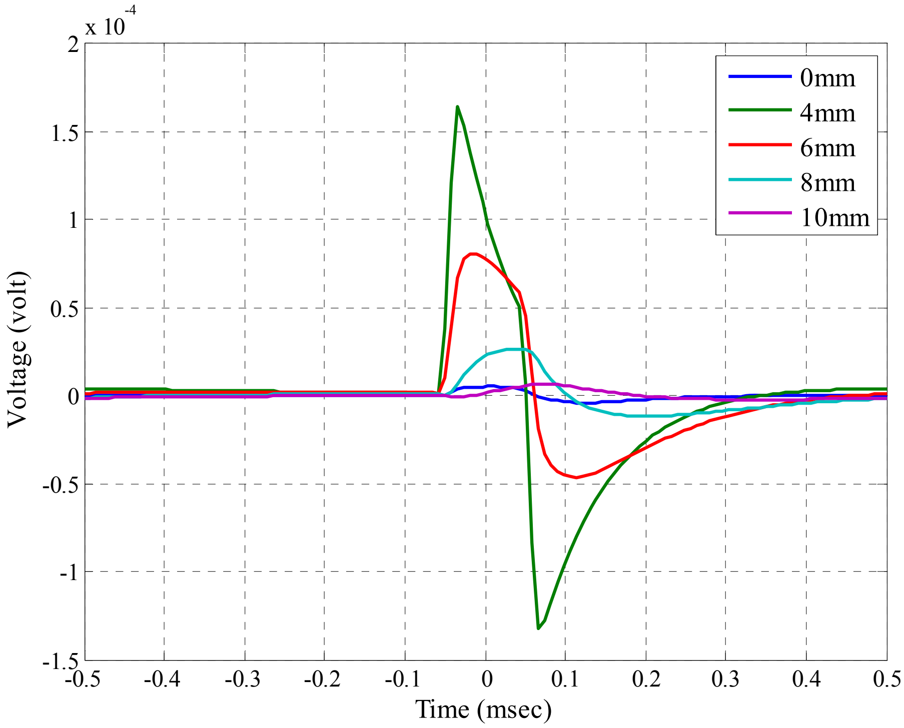


Figure 3.10: Time domain picked up voltage signal for crack I for different probe positions.

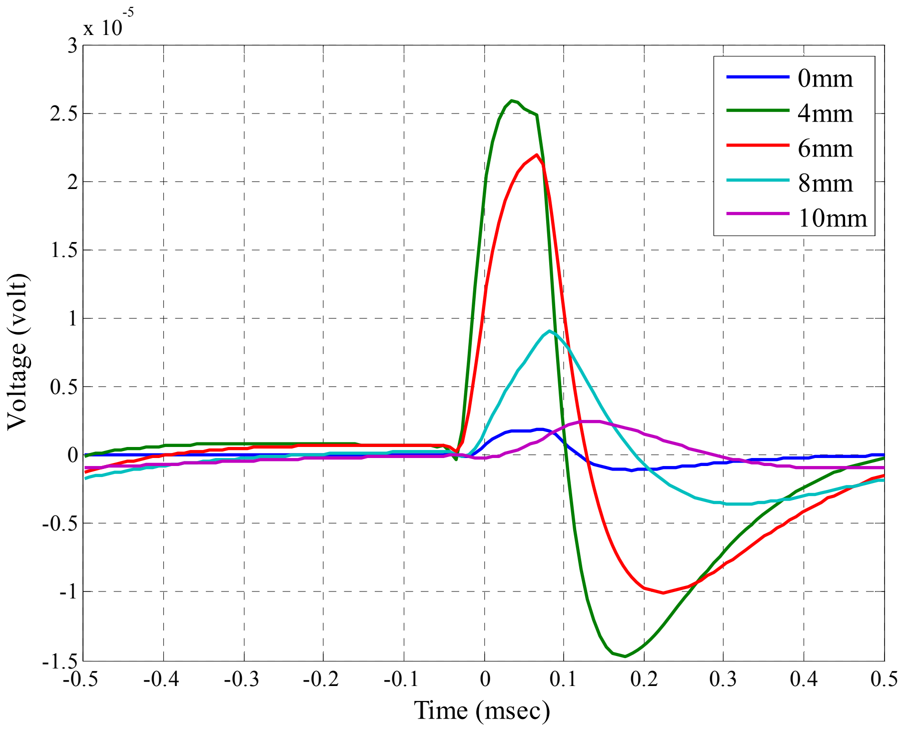


Figure 3.11: Time domain picked up voltage signal for crack II for different probe positions.

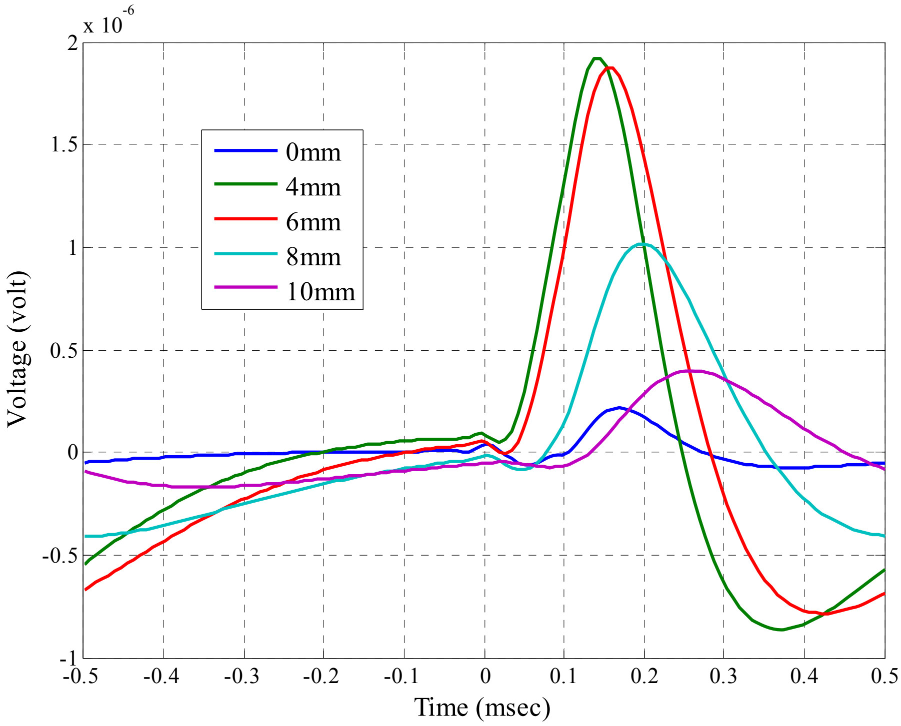


Figure 3.12: Time domain picked up voltage signal for crack III for different probe positions.

From the above three figures notice the effect when the coil and the crack on the same axis i.e. when the coil at position exactly above the crack, the picked up signal is very small as a result of the core and symmetry. This effect introduces the tradeoff between the spatial resolution and the practical difficulty in designing a small coil that can drive high inspection current.

Figures 3.13, through 3.15, show the PEC signal with different excitation pulse width, but the same average power, at the same location of probe with respect to the three cracks, these Figures demonstrate the difference effect of each crack on the picked up signal, where the size of the cracks decreases and so the amplitude of the

signal, while the deeper the crack the lag the effect on the picked up signal. Meanwhile the pulse width has no significant effect.

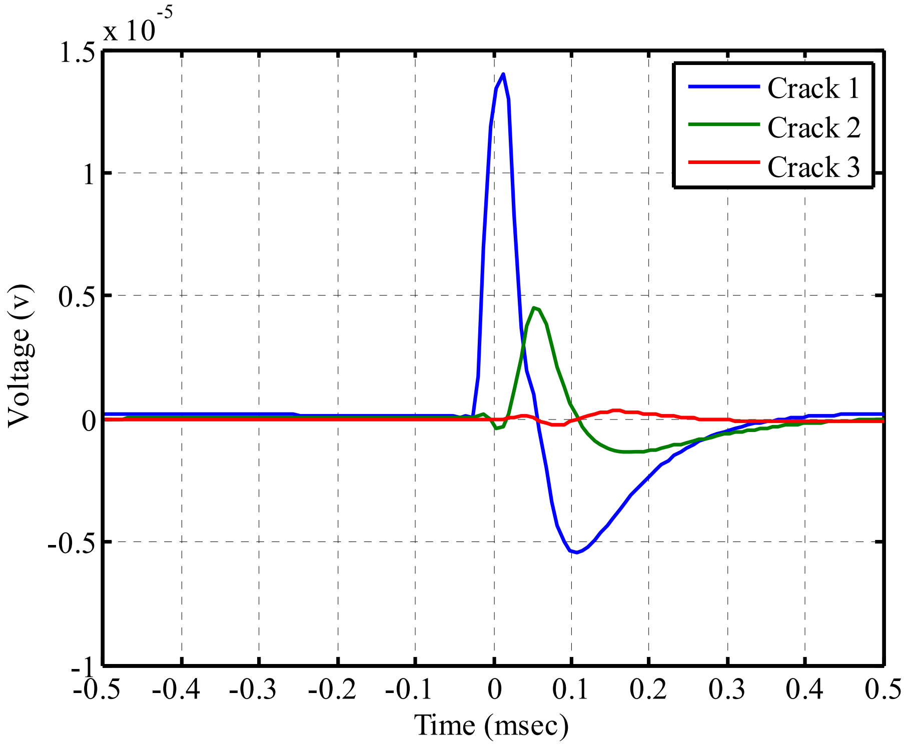


Figure 3.13: Time domain picked up voltage signal at origin for three cracks, with excitation pulse width 31.25μs.

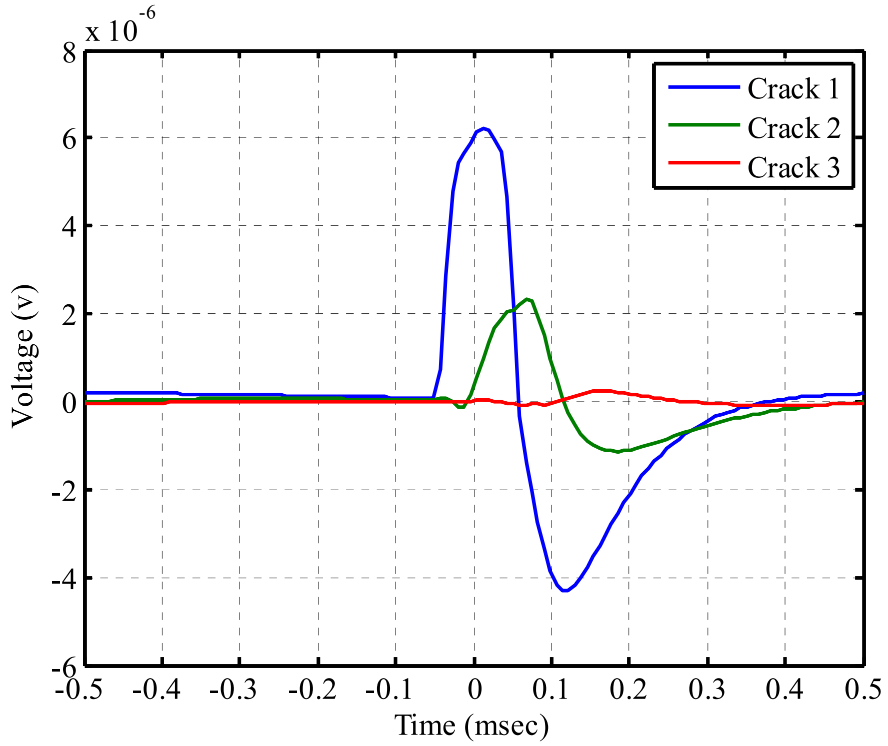


Figure 3.14: Time domain picked up voltage signal at origin for three cracks, with excitation pulse width 78.125μs.

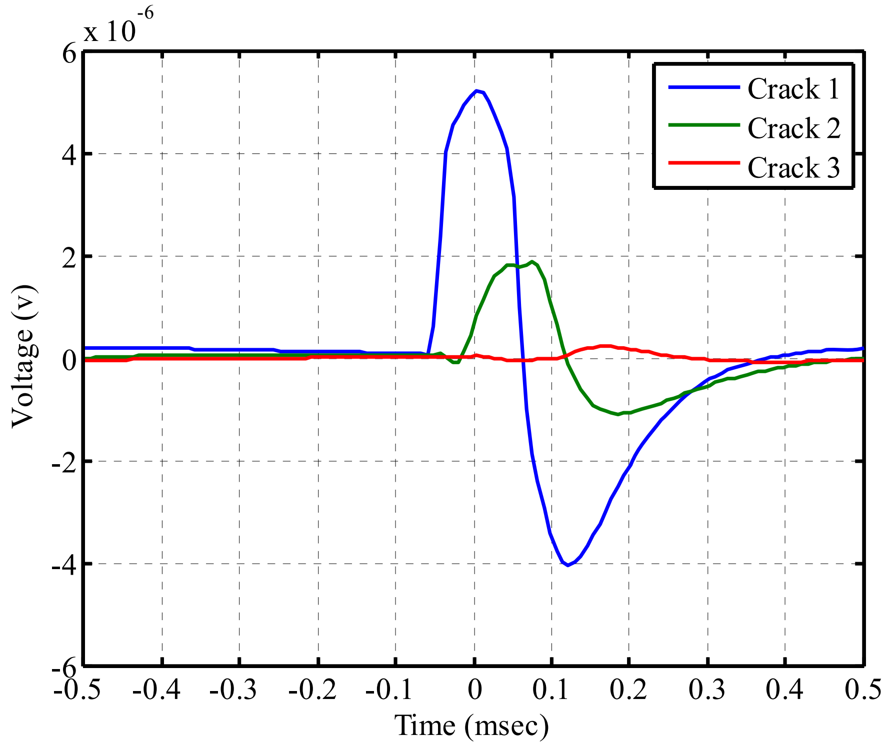


Figure 3.15: Time domain picked up voltage signal at origin for three cracks, with excitation pulse width 93.75μs.

CHAPTER 4

EDDY CURRENT IMAGING

Data visualization is an effective intuitive method for understanding the results of testing. It is easier for the inspector to understand the testing results in the image format than in the numerical one, or strip chart. An effective data visualization stage will help to improve the evaluation, especially in quantitative evaluation of types, locations, sizes and shapes of the defects. On the other hand imaging reduces the necessity for highly qualified inspector for interpretation of the results, since image will help in naturally reading of the data. Imaging also gives the ability to use the advanced image processing techniques for further improvements as image fusions which have been studied in this research.

This chapter talks about subject related to imaging, in the next section EC imaging results are presented for both conventional EC, and pulsed EC. In section 4.2 the idea and result of image registration is illustrated. EC noise simulation and experimental results are discussed in section 4.3.

4.1 Eddy Current Imaging

Various techniques have been developed to put eddy current inspection data in the form of C-scan images. Probe impedance values acquired in two dimensional surface

scans provide a set of ranges [17]. Magnetic flux maps could also be presented in image format using techniques such as magneto-optic eddy current technology [58] or giant magneto-resistive sensors GMR field scanning [59].

In this study, in conventional EC sequence of probe impedance are recorded while the probe is scanning the object to be tested i.e. the model is solved for different positions then the differential values arranged to obtain C-scan images. In PEC the feature extracted from the picked-up signal either the maximum, time to maximum, the minimum, or time to zero crossing, arranged to form C-scan images.

Experimentally, scanning using robotic and X-Y plotter have been used to produce an image. Detail of this subject comes later in this chapter.

Sequence values of probe inductance and resistance values are recorded and arranged to obtain c-scan images which simulates an object with the three crack types described earlier. Crack 1 is on the right, crack 2 is on the left and type 3 crack is in the middle. Figure 4.1 presents ten images generated with 128x128 resolution, representing probe resistance values (images R_1-R_5) on the top row, and probe inductance values (images L_1-L_5) on the bottom row. Images R_1 and L_1 on the left side correspond to lowest frequency while R_5 & L_5 on the right side correspond to high.

In PEC it is very important to select the feature accurately based on the previous knowledge about the possible crack that might be most probably occur. In surface cracks the amplitude feature gives better resolution, while the time feature gives more information about the subsurface cracks. In Figures 4.2 to 4.5, PEC images are shown for different features extracted from the picked up signals with different excitation pulse width as illustrated in chapter 3, from these figures it is clear that different feature gives different resolution with the conclusion that all cracks are detected.

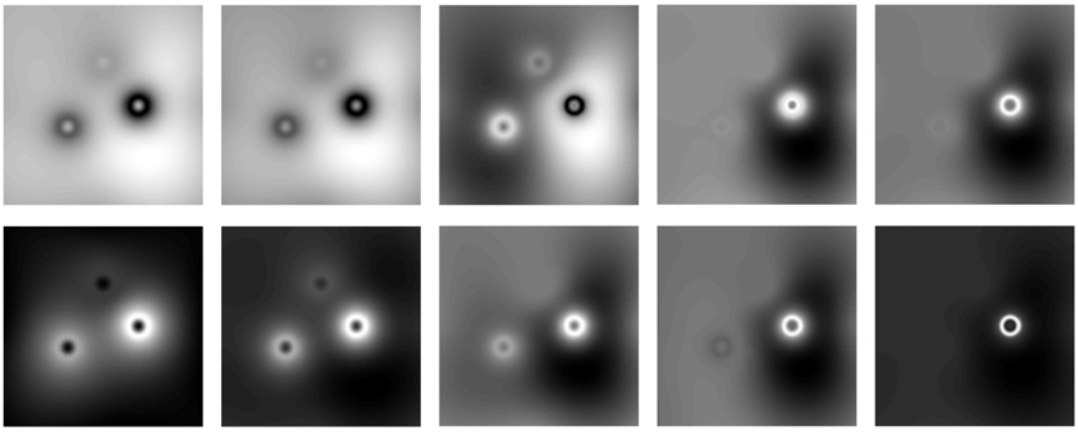


Figure 4.1: Ten images representing probe resistance values R_1-R_5 (top row, left to right) and inductance values L_1-L_5 (bottom row, left to right) corresponding to five different frequencies: 100 Hz, 1 kHz, 10 kHz, 100 kHz, and 1M Hz.

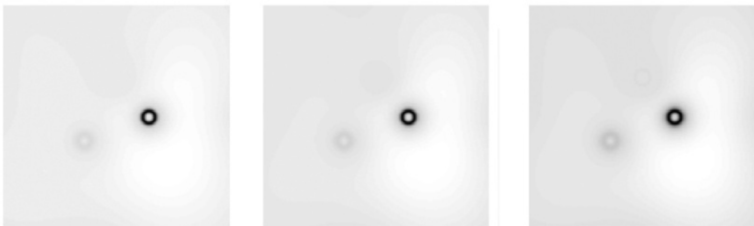


Figure 4.2: PEC images for the minimum amplitude feature for different excitation pulse width.

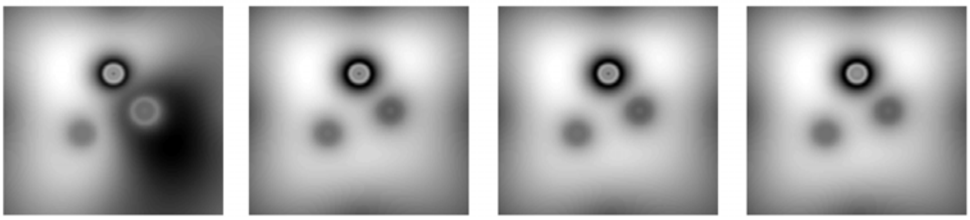


Figure 4.3: PEC images for the time to minimum amplitude feature for different excitation pulse width.

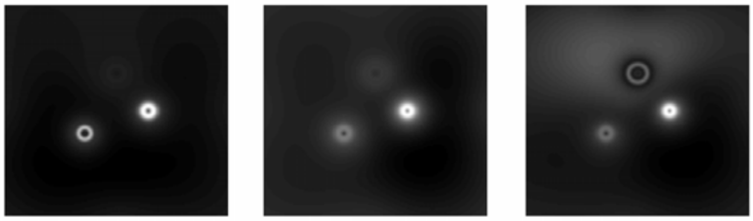


Figure 4.4: PEC images for maximum amplitude for different feature for different excitation pulse width.

Figure 4.5 shows an image that gives information about the depth of the cracks, where the surface of the object to be tested taken as a reference, and this is practically can be done through the calibration stage at the beginning of any inspection process.

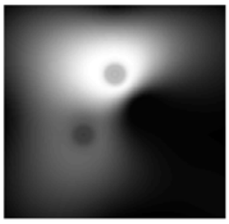


Figure 4.5: PEC image for the time to maximum feature taking the surface as a reference.

4.2 Experimental Eddy Current imaging

Experimental EC images produced by employing EC measurement device connected to a scanning system. Two scanning systems were used:

1. Simple scanning system using old Roland X-Y plotter DXY-1150A shown in Figure 4.6, and EC measurement system (Rohmann B300) [60] shown in Figure 4.7. The two dimensional X-Y plotter controlled via a full handshaking null modem with special commands.
2. Advanced scanning system based on six degree of freedom robot arm manufactured by Staubli [61] shown in Figure 4.8 which can gives a resolution of 0.1 mm.

The output of the EC measurement system for both scanning systems was connected to a data acquisition system manufactured by National Instruments [62] and the data then stored for future processing.

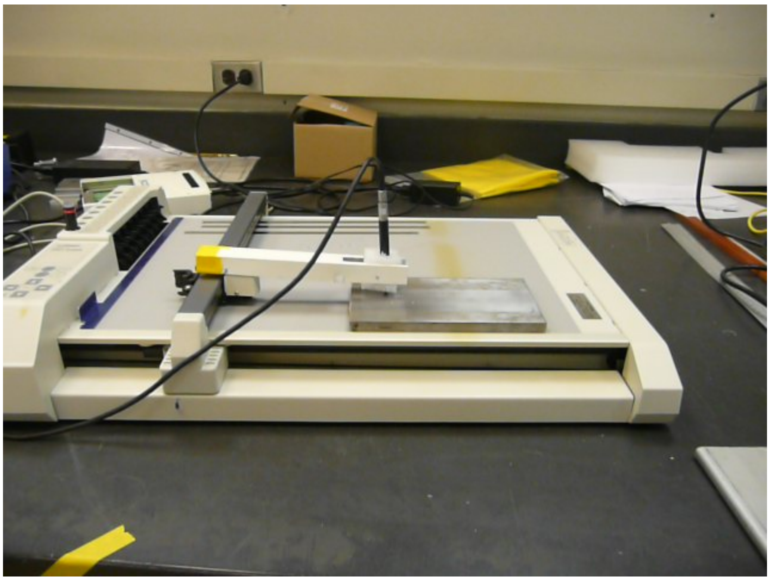


Figure 4.6: Type I developed scanning system based on Roland X-Y plotter DXY-1150A.

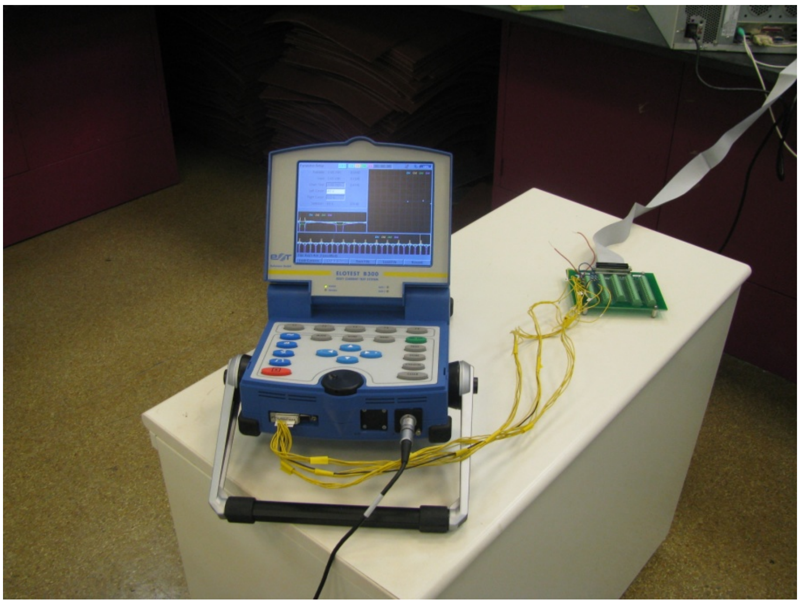


Figure 4.7: Eddy current measurement system (Rohmann B 300).

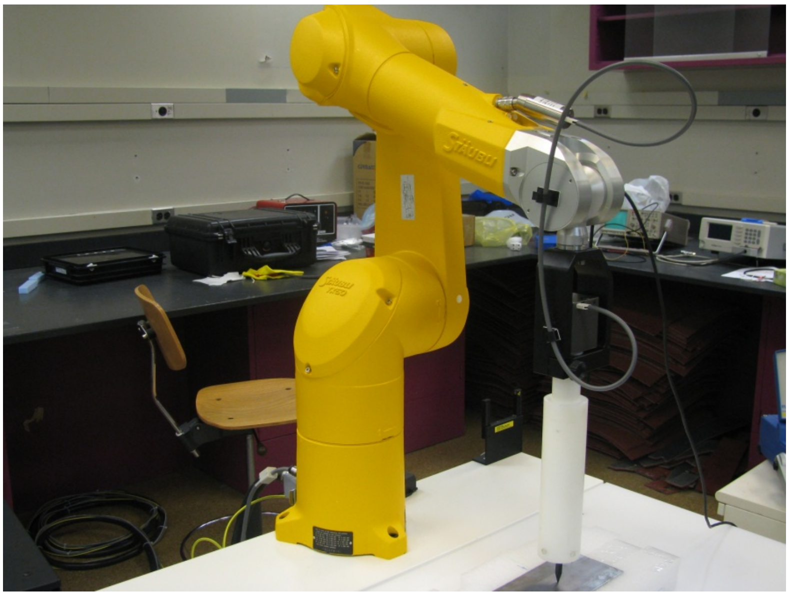


Figure 4.8: Staubli robot which is the main part of advanced type II scanning system.

The standard sample used for experimental measurements is shown in Figure 4.9. This plate was manufactured by Olympus NDT [63], and it has been chosen because of the artificial cracks have different sizes, shapes, and orientation with respect to the scanning direction.

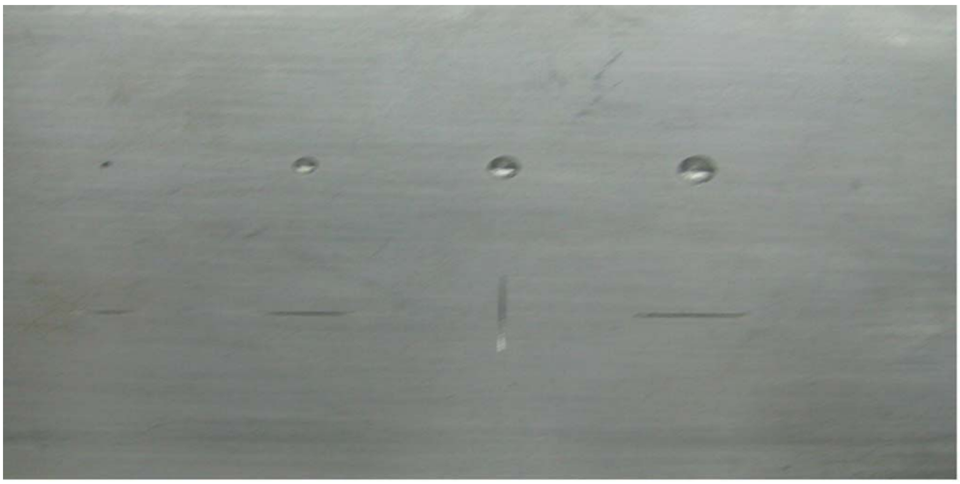


Figure 4.9: Optical photo of the plate used in experimental measurements.

Figure 4.10 show four experimental images at frequencies 10 kHz, 100 kHz, 300 kHz, and 800 kHz, respectively. These images represent the amplitude of the vertical component after the rotation of the axes to reduce the effect of liftoff noise.

4.3 Image Registration Methodology

Multi-sensor image registration is a preprocessing stage to find the corresponding scene or character in different images of the same object, following which may be the fusion or compression operation. It is of great importance in the fields of aerial surveillance, automatic target recognition, machine vision, medical imaging and NDE wherever multiple modalities are employed and the acquired data is in the image format. The registration can be defined as the process, which determines the best match of two or more images acquired at the same or different times by different or identical sensors.

One image is used as the reference image, and all the other images, called input image, are matched relative to the reference data. In the common approach, control points, which represent the most significant and outstanding characteristics of the images, are searched to perform the matching and compute the transformation function between two images. Match can be performed at the one-dimensional level, the two-dimensional level and the three-dimensional level.

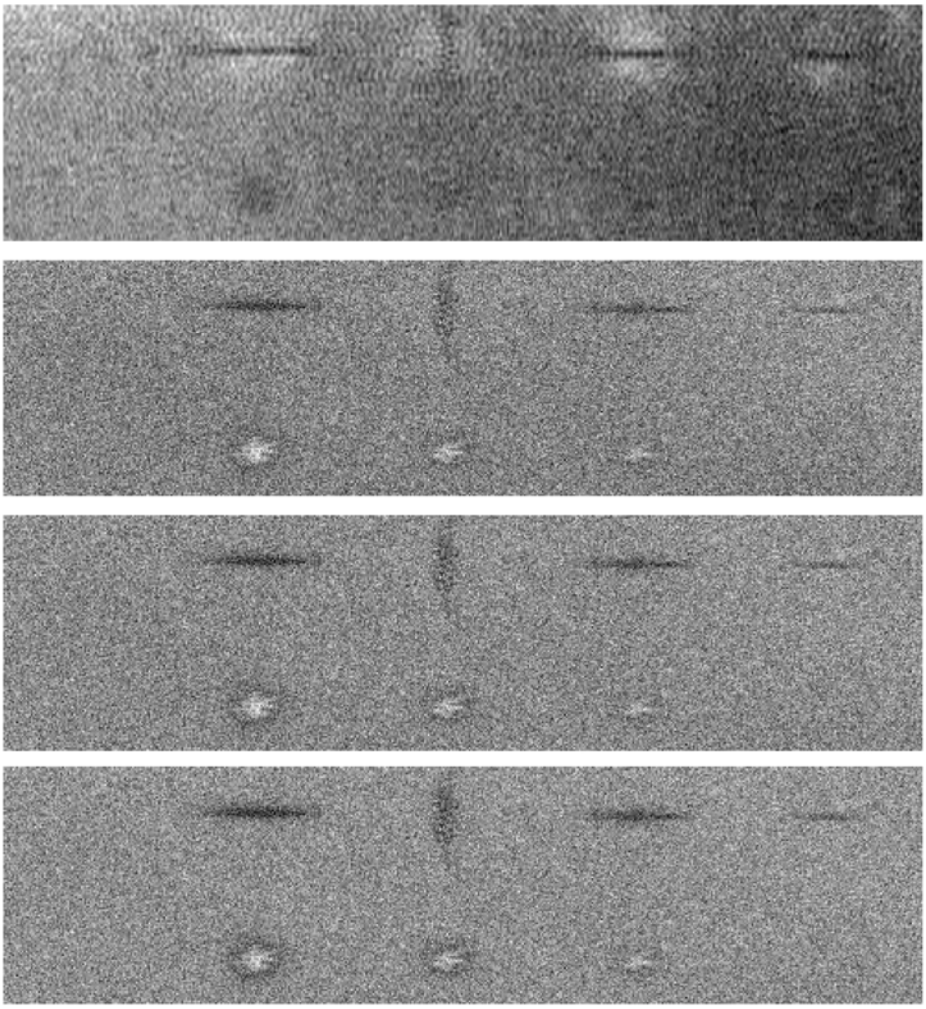


Figure 4.10: Measured EC images at 10 kHz, 100 kHz, 300 kHz, and 800 kHz.

Image registration, as mentioned above, can be divided into four main groups according to the manner of the image acquisition:

1. **Different viewpoints** (multi-view analysis). Images of the same scene are acquired from different viewpoints. The aim is to gain a larger 2D view or 3D representation of the scanned scene. Examples of applications; remote sensing, and computer vision.
2. **Different times** (multi-temporal analysis). Images of the same scene are acquired at different times, often on regular basis, and possibly under different

conditions. The aim is to find and evaluate changes in the scene which appeared between the consecutive images acquisitions. Examples of applications; remote sensing i.e. monitoring of global land usage, landscape planning, computer vision, i.e. automatic change detection for security monitoring, motion tracking, medical imaging, i.e. monitoring of the healing therapy, monitoring of the tumor evolution, and NDE i.e. tracking the spreading of stress crack.

3. **Different sensors** (multi-modal analysis). Images of the same scene are acquired by different sensors. The aim is to integrate the information obtained from different source streams to gain more informative and detailed scene representation. Examples of applications; NDE i.e. eddy current sensor, and optical sensor, or eddy current sensors and ultrasonic sensors. Remote sensing, fusion of information from sensors with different characteristics like panchromatic images, and multispectral images. Medical imaging, combination of sensors recording the anatomical body structure like magnetic resonance image (MRI), ultrasound or computer tomography (CT).
4. **Scene to model registration.** Images of a scene and a model of the scene are registered. The aim is to localize the acquired image in the scene/model and/or to compare them. Examples of applications: Remote sensing, registration of aerial or satellite data into maps or other geographic information systems GIS layers. Computer vision, target template matching with real-time images, automatic quality inspection. Medical imaging, comparison of the patient's image with digital anatomical atlases, specimen classification.

Due to the diversity of images to be registered and due to various types of degradations it is impossible to design a universal method applicable to all registration tasks [64], and [65]. The registration problems basically include dilation, translation and rotation.

The majority of the registration methods consist of the following four steps [64] as shown in Figure 4.11:

1. **Selection of feature points**. Salient and distinctive objects (closed-boundary regions, edges, contours, line intersections, corners, etc.) are manually or, preferably, automatically detected. These points are called control points (CPs) in the literature.
2. **Feature matching**. In this step, the correspondence between the features detected in the input image and those detected in the reference image is established. Various feature descriptors and similarity measures along with spatial relationships among the features are used for that purpose.
3. **Transform model estimation**. The type and parameters of the so-called mapping functions, aligning the input image with the reference image, are estimated. The parameters of the mapping functions are computed by means of the established feature correspondence.
4. **Image re-sampling and transformation**. The input image is transformed by means of the mapping functions. Image values in non-integer coordinates are computed by the appropriate interpolation technique.

The above four steps shown in figure 4.11, illustrated as follows:

- Top row: feature detection (corners were used as the features in this case).

- Middle row: feature matching by invariant descriptors (the corresponding pairs are marked by numbers).
- Bottom left: transform model estimation exploiting the established correspondence.
- Bottom right: image re-sampling and transformation, using appropriate interpolation technique.

In this research the registration is needed to align the experimental images with the sample optical image shown in Figure 4.9, which can be used in the fusion, as will be discussed in chapter 6. In our study the simulation results can be arranged so that the registration stage is assumed perfect.

4.4 Eddy Current Noise Analysis

Eddy current inspection modalities have been observed to exhibit many different sources of noise: liftoff noise, conductivity change noise, inspection tilt angle, and thermal noise. In this study various modeling runs have been performed to model the liftoff and conductivity perturbation noise, the noise model for liftoff and conductivity are assumed Gaussian. For example if the liftoff and conductivity means are 1.1 mm, and 3.5×10^7 s/m respectively and standard deviation is 10% of each mean for both, the analysis of the results show that the standard deviation of the real and imaginary components of the probe impedance at five excitation frequencies are shown in Table 4.1.

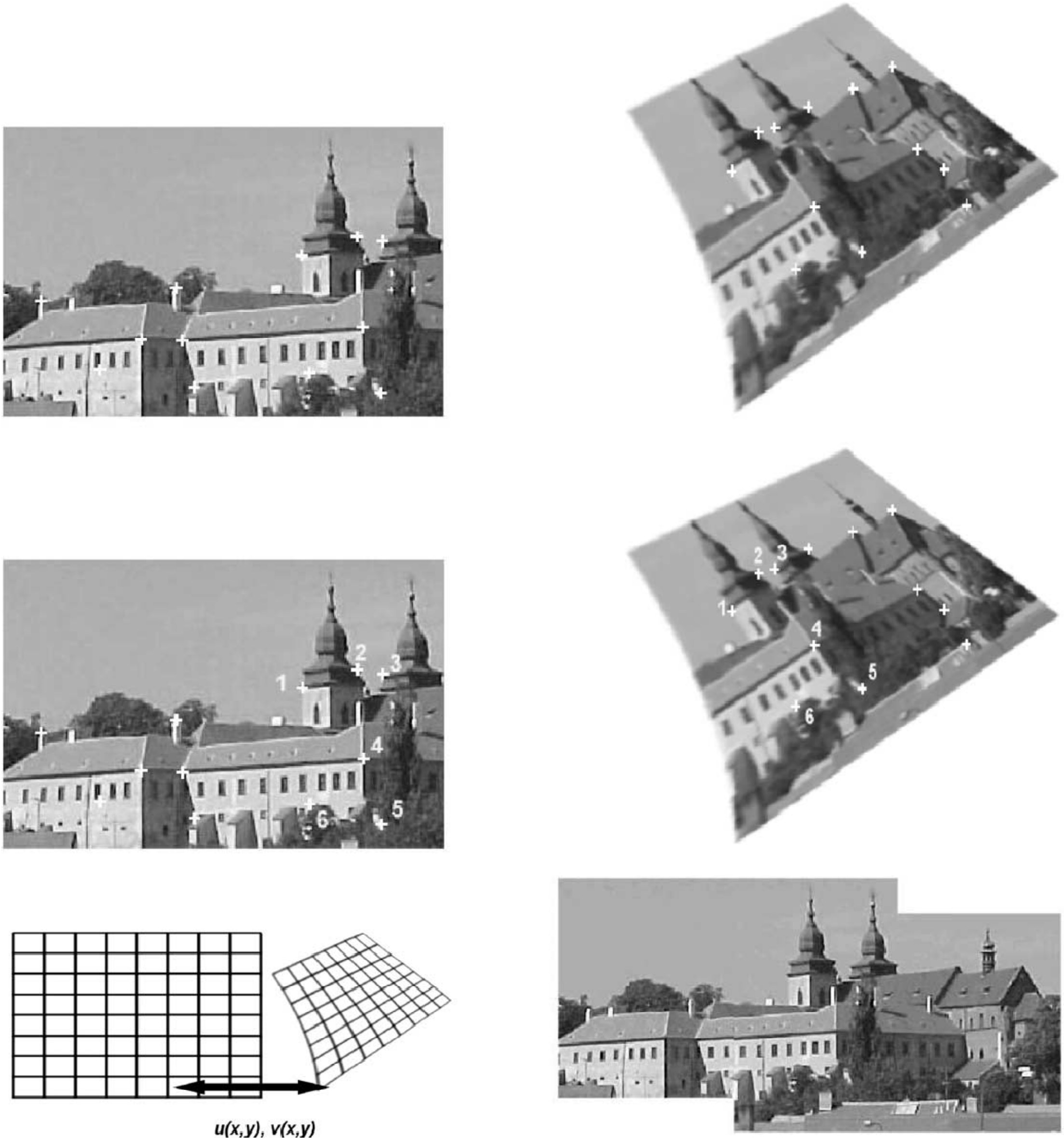


Figure 4.11: Four steps of image registration ([64]).

Table 4.1 Standard deviation of the real and imaginary components of the probe impedance

Frequency	SD (Real)	SD (Imaginary) $\times 10^{-5}$
100 Hz	0.0013	4.3
10kHz	0.6793	3.36
100kHz	4.5226	3.17
500kHz	13.3210	3.28
1MHz	17.6404	3.28

It is clear that the real component of the probe impedance representing the resistance is very sensitive to liftoff and conductivity perturbations as the frequency increases, while the imaginary component representing the inductance is more resistant to liftoff and conductivity noise. Another analysis has been done for liftoff noise with conductivity constant and vice versa, with the same parameters mentioned above, it has been noticed that the liftoff noise introduces 90.8% of the EC noise.

In order to test the noise distribution, a plot called normal probability plot, are used to assess whether data comes from a normal distribution. Any statistical procedures make the assumption that an underlying distribution is normal, so normal probability plots can provide some assurance that the assumption is justified, or else provide a warning of problems with the assumption.

An analysis of normality typically combines normal probability plots with hypothesis tests for normality. Figures 4.12 to 4.16 show the normal probability plots of the probe resistance data at different frequencies, where the plus signs plot the empirical probability versus the data value for each point in the data. A solid line connects the 25th and 75th percentiles in the data, and then extends it to the ends of the data. The y-axis values are probabilities from zero to one, but the scale is not linear. The distance between tick marks on the y-axis matches the distance between the quintiles of a normal distribution. The quintiles are close together near the median (probability = 0.5) and stretch out symmetrically moving away from the median. In a normal probability plot, if all the data points fall near the line, an assumption of normality is reasonable. Otherwise, the points will curve away from the line, and an assumption of normality is not justified.

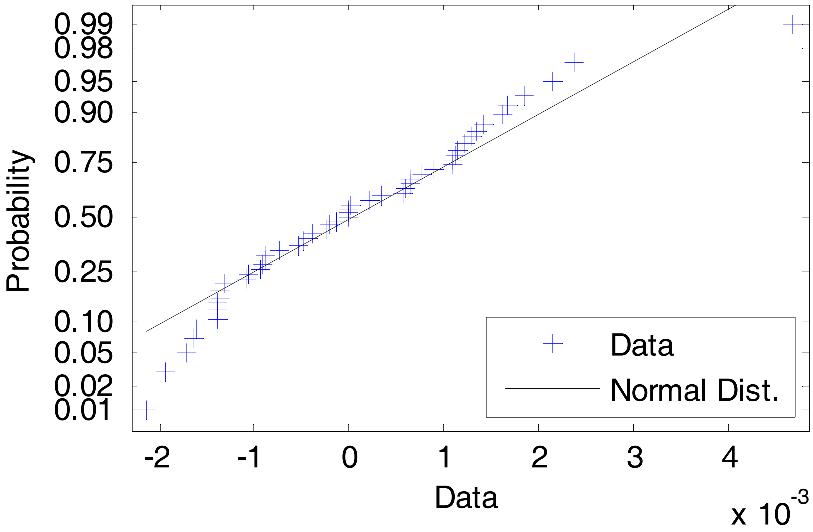


Figure 4.12: Normal probability plot of probe resistance noise at 100Hz.

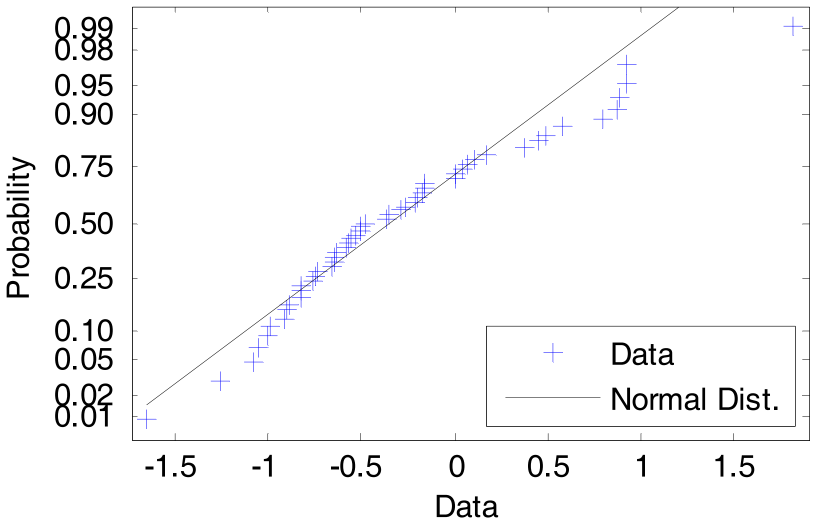


Figure 4.13: Normal probability plot of probe resistance noise at 10 kHz.

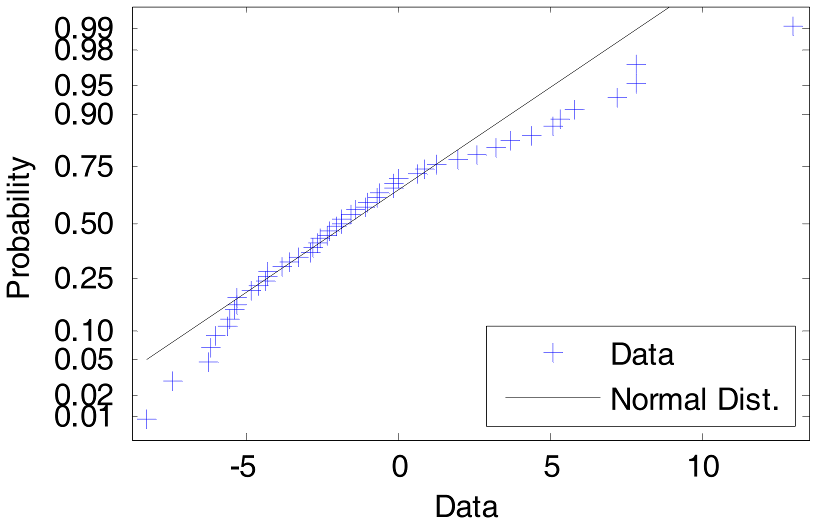


Figure 4.14: Normal probability plot of probe resistance noise at 100 kHz.

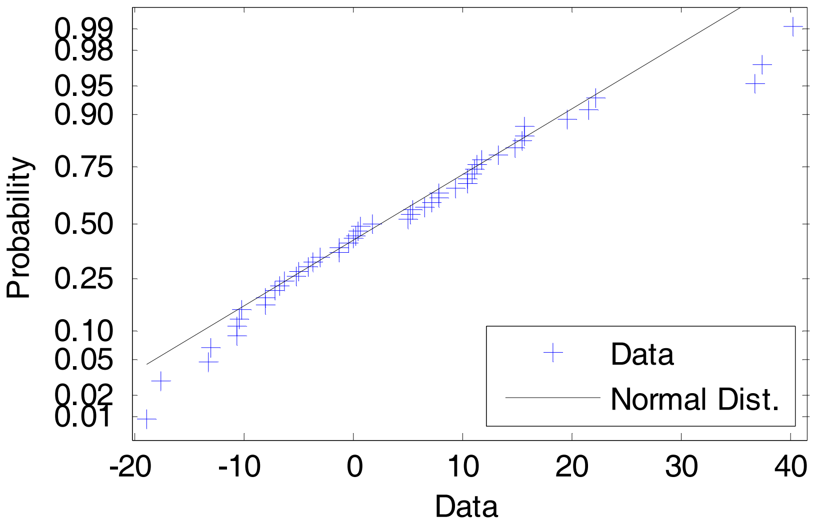


Figure 4.15: Normal probability plot of probe resistance noise at 500 kHz.

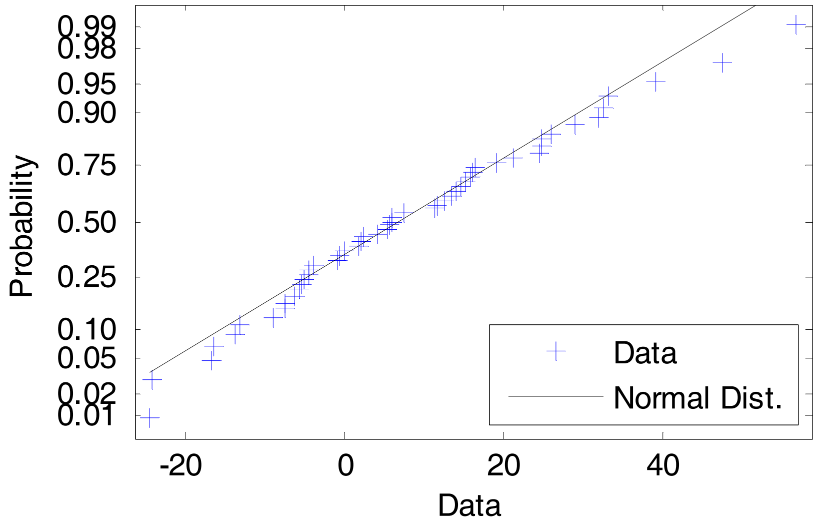


Figure 4.16: Normal probability plot of probe resistance noise at 1 MHz.

Figures 4.12 - 4.16 shows that the distributions in all figures are almost Gaussian, provided that the assumptions that have been mentioned above are valid, and the distribution come closer to Gaussian as the frequency increases, the same effect have been noticed with normal probability plot of the probe inductance.

Another analysis has been made from the above modeling runs to figure out the effect on the flux passing through a closed contour with the same assumptions. The analysis results shows that the noise add to the magnitude of the flux is Gaussian distribution, while the noise effect of the flux angle are shown in Figures 4.17 – 4.20

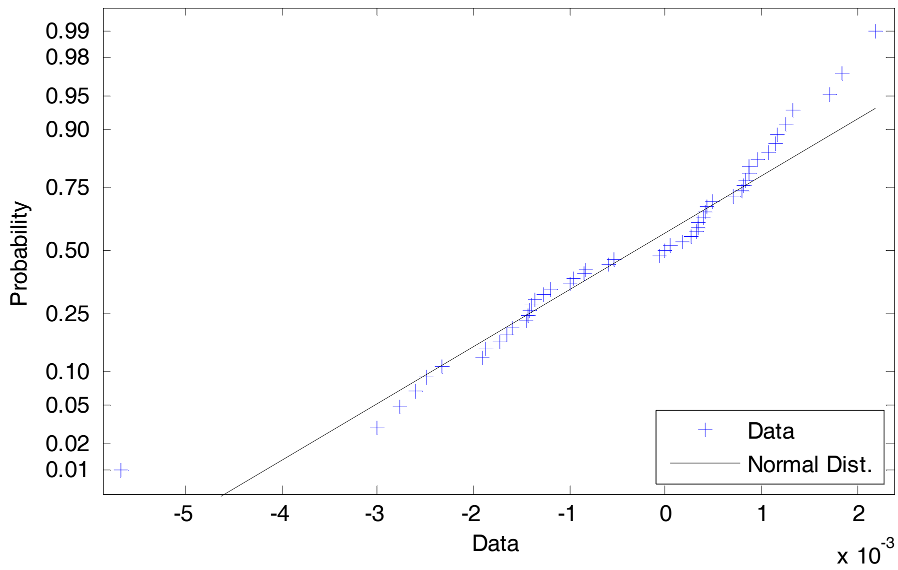


Figure 4.17: Normal probability plot of flux angle noise at 100Hz.

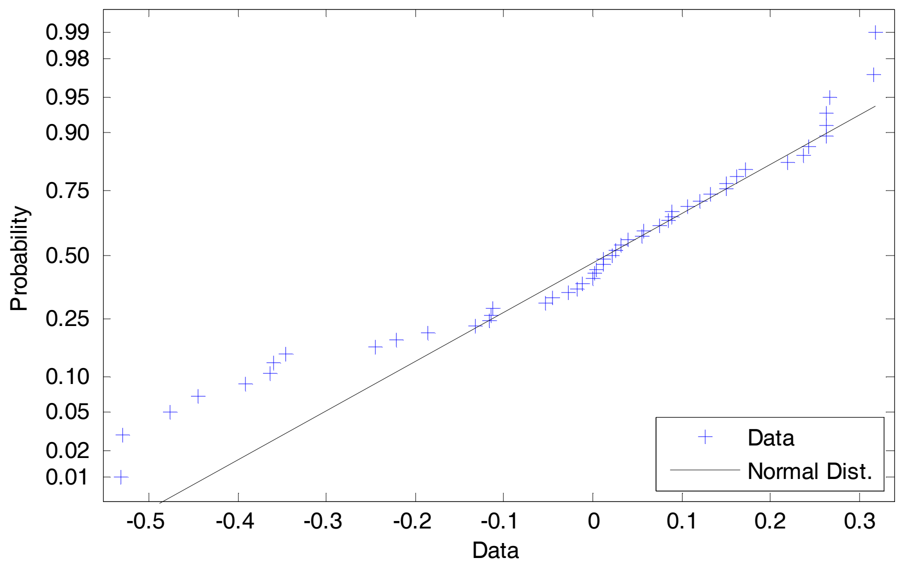


Figure 4.18: Normal probability plot of flux angle noise at 100kHz.

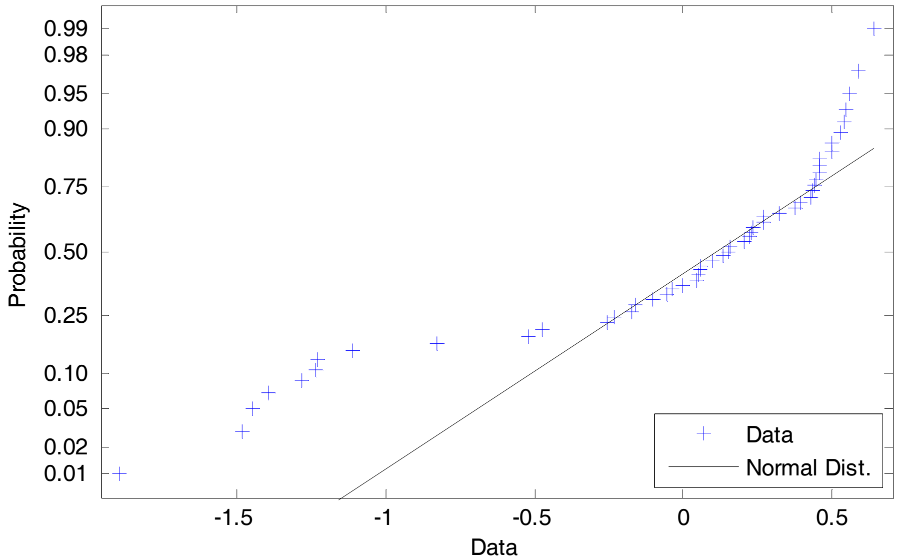


Figure 4.19: Normal probability plot of flux angle noise at 500kHz.

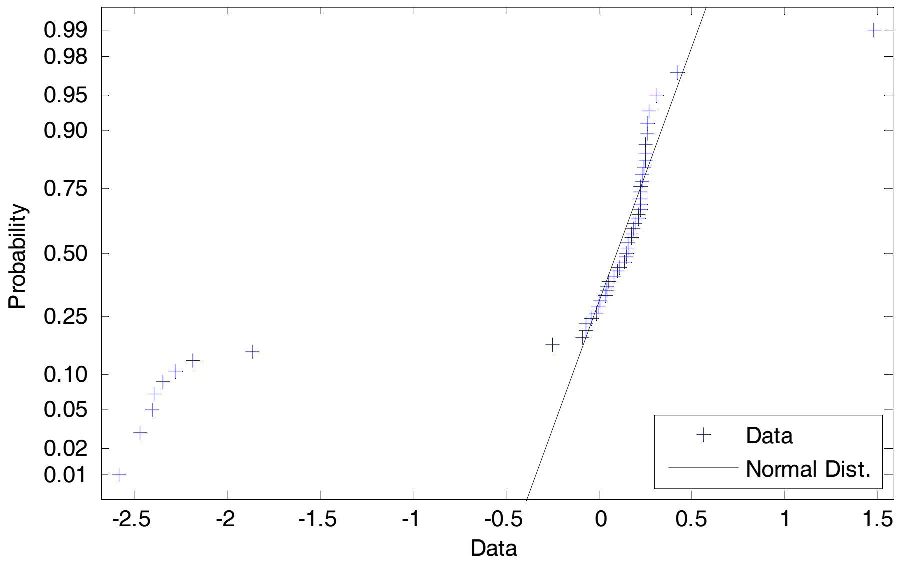


Figure 4.20: Normal probability plot of flux angle noise at 1MHz.

From Figures 4.17 – 4.20 it is clear that the points curve away from the line as the frequency increases, and the assumption of normality is not justified as the cases shown in Figures 4.19, and 4.20. Since in PEC the most energy is concentrated in the lower frequency band, the PEC noise is assumed Gaussian.

Figure 4.21 gives an example of Gaussian noise with zero mean and 10% standard deviation added to the ten conventional EC images, to show how the noise affect the EC inspection particularly the liftoff noise.

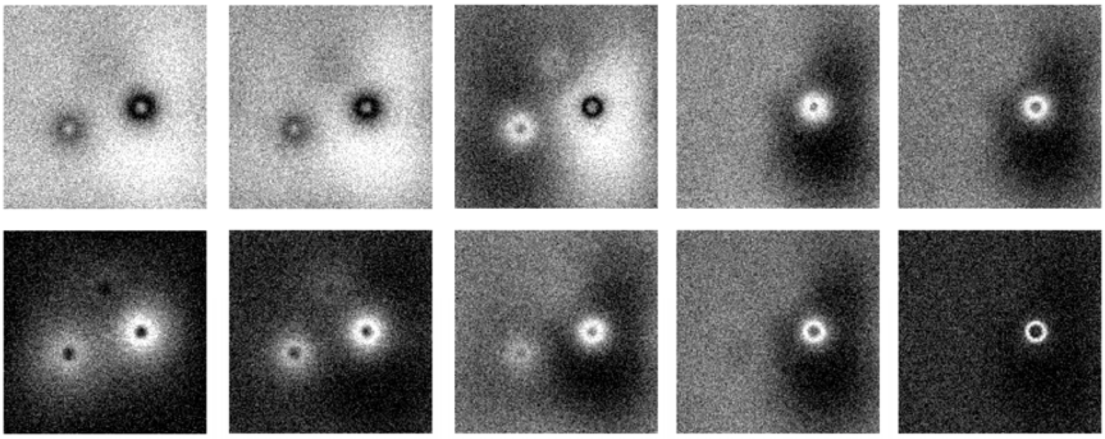


Figure 4.21: Gaussian noise added to EC images.

CHAPTER 5

FUSION PERFORMANCE EVALUATION

The best method for assessing the quality of the fused image generally depends on the application domain. In many applications, a human observer is the end user of the fused image. Therefore, the human perception and interpretation of the fused image is very important. Consequently, one way to assess the fused images is to use subjective tests. In these tests, human observers are asked to view a series of fused images and rate them. Although the subjective tests are typically accurate whenever performed correctly, they are inconvenient, expensive, and time consuming. Hence, an objective performance measure that can accurately predict human perception would be a valuable complementary method. However, it is difficult to find a good, easy to calculate, objective evaluation criterion which matches favorably with visual inspection and is suitable for a variety of different application requirements. In the literature, there are two broad classes of objective performance measures. One class requires a reference image, while the other does not [66 - 68].

5.1 Objective Evaluation Measures Requiring a Reference Image

For certain applications, it is possible to generate an ideal fused image. This ideal fused image is then used as a reference to compare with the experimental fused results. The quality metrics used for these comparisons are listed next:

1. The root mean square error (RMSE)

$$RMSE = \sqrt{\frac{1}{NM}\sum_{i=1}^{N}\sum_{j=1}^{M}|R(i,j) - F(i,j)|^2} \tag{5.1}$$

where *R* denotes the reference image, *F* denotes the fused image, *(i, j)* denotes a given pixel, and $N \times M$ is the size of the image.

2. The correlation (CORR)

$$CORR = \frac{2C_{R,F}}{C_R + C_F} \tag{5.2}$$

where

$$C_R = \sum_{i=1}^{N}\sum_{j=1}^{M} R(i,j)^2 \tag{5.3}$$

$$C_F = \sum_{i=1}^{N}\sum_{j=1}^{M} F(i,j)^2 \tag{5.4}$$

$$C_{R,F} = \sum_{i=1}^{N}\sum_{j=1}^{M} R(i,j)F(i,j) \tag{5.5}$$

3. The peak signal to noise ratio (PSNR)

$$PSNR = 10log_{10}\left(\frac{L^2}{\frac{1}{NM}\sum_{i=1}^{N}\sum_{j=1}^{M}|R(i,j) - F(i,j)|^2}\right) \tag{5.6}$$

where L is the number of gray levels in the image.

4. The mutual information (MI)

$$MI = \sum_{i_1=1}^{L}\sum_{i_2=1}^{L} h_{R,F}(i_1, i_2)log_2 \frac{h_{R,F}(i_1, i_2)}{h_R(i_1)h_F(i_2)} \tag{5.7}$$

where $h_{R,F}$ denotes the normalized joint gray level histogram of images R and F while h_R, h_F are the normalized marginal histograms of the two images.

The four objective image quality measures, RMSE, PSNR, CORR, MI, are widely employed due to their simplicity. However, they must be used carefully because they have been found to sometimes not correlate well with human evaluation when sensors of different types are considered [44].

5. Structure information, structural similarity (SSIM). This image quality assessment proposed by Wang, and Bovik [66]

$$SSIM = \frac{(2\mu_R\mu_F + C_1)(2\sigma_{RF} + C_2)}{(\mu_R^2 + \mu_F^2 + C_1)(\sigma_R^2 + \sigma_F^2 + C_2)} \tag{5.8}$$

where C_1 is a constant that is included to avoid the instability when sum of mean of reference image R, and mean of fused image F is close to zero (i.e. $\mu_R^2 + \mu_F^2 \approx 0$), and C_2 is a constant that is included to avoid the instability when standard deviations is close to zero (i.e. $\sigma_R^2 + \sigma_F^2 \approx 0$)

5.2 Objective Evaluation Measures Not Requiring a Reference Image

As stated previously, quantitatively accessing the performance in practical applications is a complicated issue because it is usually very difficult to access the truth (i.e., the ideal composite images is normally unknown). Several simple quantitative evaluation methods which do not require a reference image are listed below.

1. The standard deviation (SD)

$$\sigma = \sqrt{\sum_{i=0}^{L} (i - \bar{\imath})^2 h(i)}, \qquad \bar{\imath} = \sum_{i=0}^{L} i h(i) \tag{5.9}$$

   where h is the normalized histogram of image.

2. The entropy (H)

$$H = -\sum_{i=0}^{L} h(i) log_2 h(i) \tag{5.10}$$

3. Petrovic quality index (QE)

   Xydess and Petrovic [68] proposed an objective performance metric which measures the amount of information that is transferred from the input images into the fused image. Their approach is based on the assumption that important visual information is related with edge information.

   A Sobel edge operator is applied to yield edge strength $g(i,j)$ and orientation $\alpha(i,j) \in [0,\pi]$ for each pixel of the image. Then the relative strength and orientation

values, $G^{AF}(i,j)$ and $\Phi^{AF}(i,j)$, of input image *A* with respect to fused image *F* are defined as:

$$G^{AF}(i,j) = \begin{cases} \dfrac{g_F(i,j)}{g_A(i,j)} & if\ g^F(i,j) > g^A(i,j) \\ \dfrac{g_A(i,j)}{g_F(i,j)} & otherwise \end{cases} \tag{5.11}$$

and

$$\Phi^{AF}(i,j) = 1 - \frac{|\alpha_A(i,j) - \alpha_F(i,j)|}{\pi/2} \tag{5.12}$$

The edge preservation values Q^{AF} from input image *A* to fused result *F* is formed by the product of a sigmoid mapping function of the relative strength and orientation factors. Some constants as defined in [68] $\kappa, \sigma, and\ \Gamma$ determine the shape of the sigmoid mapping as

$$Q^{AF}(i,j) = \frac{\Gamma_g \Gamma_a}{\left(1 + exp^{\kappa_g\left(G^{AF}(i,j) - \sigma_g\right)}\right)\left(1 + exp^{\kappa_\alpha\left(\Phi^{AF}(i,j) - \sigma_\alpha\right)}\right)} \tag{5.13}$$

In equation 5.13, there are 6 parameters ($\kappa_g, \sigma_g, \Gamma_g, \kappa_a, \sigma_a, and\ \Gamma_a$), the parameters ($\kappa_g, \sigma_g, \kappa_a, \sigma_a$) are determined via an optimization process that maximizes a correspondence measure between objective and subjective image fusion assessment results. Furthermore the constant Γ_g, Γ_a selected such that for optimal values of $\kappa_g, \sigma_g, \kappa_a, \sigma_a$ and G^{AF}, Φ^{AF} equal to 1, the Q^{AF} will also be equal to 1 [69]. The overall objective quality quantity measure $QE^{AB/F}$ is obtained by weighting the normalized edge preservation values of both input images *A*, and *B* as:

$$\mathrm{QE}^{AB/F} = \frac{\sum_{i=1}^{N}\sum_{j=1}^{M} \mathrm{Q}^{AF}(i,j)w^{A}(i,j) + \mathrm{Q}^{BF}(i,j)w^{B}(i,j)}{\sum_{i=1}^{N}\sum_{j=1}^{M}(w^{A}(i,j) + w^{B}(i,j))} \tag{5.14}$$

In general the weights $w^{A}(i,j)$ and $w^{B}(i,j)$ are a function of edge strength. The range of *QE* is between 0 and 1, where 0 indicates the complete loss of source information and 1 means the ideal fusion.

CHAPTER 6

PROPOSED NDE FUSION SYSTEMS

6.1 Introduction

In many industrial applications, several NDE techniques have always been used in a complementary manner. Data fusion techniques have been developed to allow effective data acquisition and processing as well as provide sound interpretation of test parameters in relation to the material integrity. Example is in [70] implementing more than single NDE method in order to accurately detect and quantify impact damage in composite materials [70]. Use of more than one single NDE technique is becoming essential to get all the required information about the object or process being inspected, in particular, when the inspection task is difficult. Each NDE method only gives a particular type and amount of information because of the involved physical phenomena themselves. For this reason,

With the help of advanced processing and storage device, the more information gathered from different inspection modalities and fused can help to fully automate the inspection process, this task need advanced fusion techniques that can deal with more information, i.e. more images in this case.

Figure 6.1 illustrates the progress in EC technology according to history and the research directions. As a general conclusion each inspection modality has information

limit, so many research tends to merge more than one testing method to end up with a fully automated inspection system.

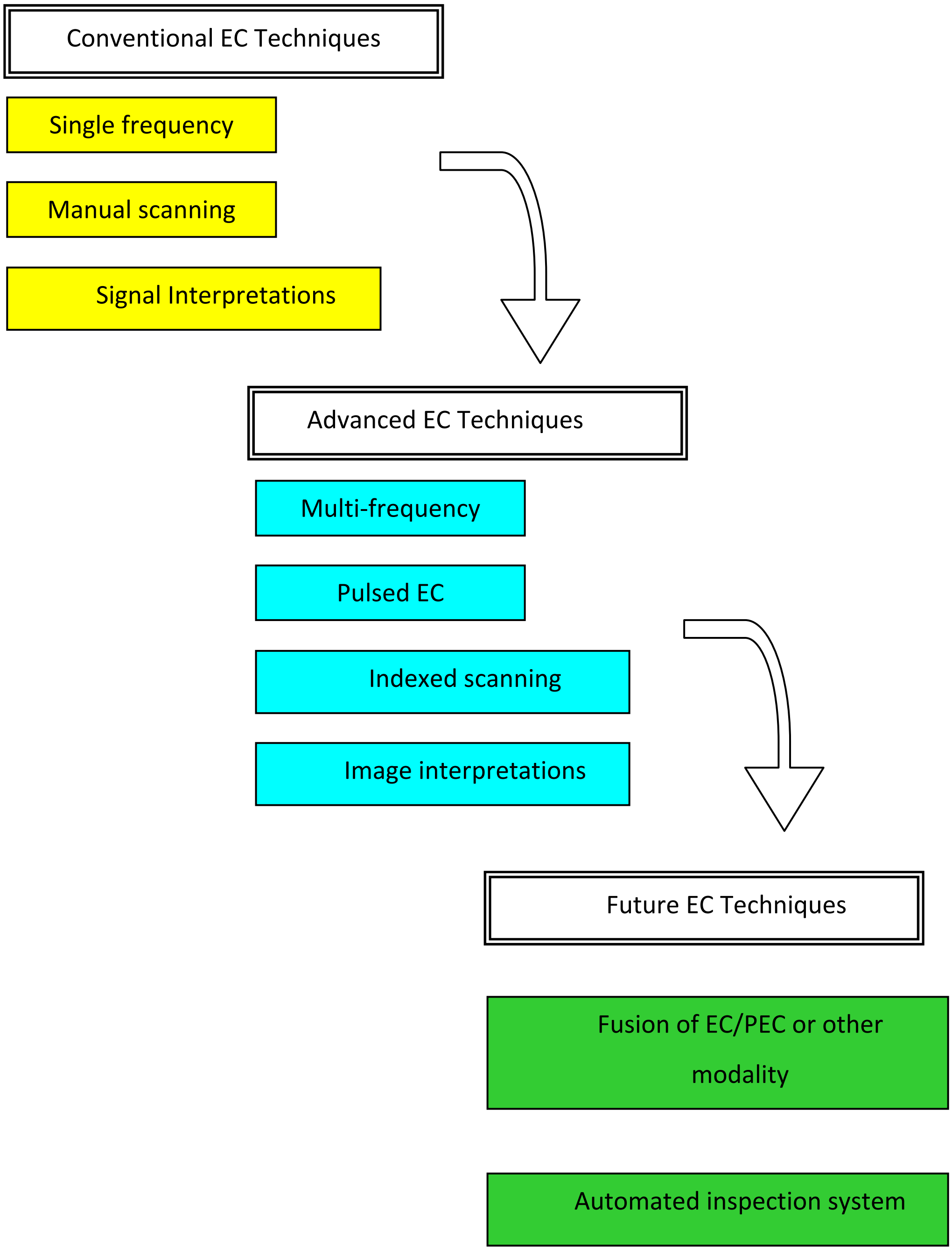


Figure 6.1: Eddy current Technology progress.

The proposed fusion systems based on linear transformation intensity hue saturation (IHS), and principal component analysis (PCA), where improvement algorithms introduced here for the application of NDE based on IHS, PCA and multi-resolution wavelet decomposition (MWD). In section 6.1 the IHS fusion method is presented, PCA is then introduced in section 6.2 which can be used to generalize the fusion of arbitrary number of images, while the proposed wavelet based NDE fusion system described in section 6.3. Results presented in section 6.4.

6.2 Intensity-Hue-Saturation (IHS) Transform Fusion

The IHS technique is a standard procedure in image fusion, and has fast computing capability for fusing images [71].

The widespread use of the IHS transform to merge remote sensing images is based on the ability to separate the spectral information of the RGB image into its two components (H) and (S), while isolating most of the spatial information in the (I) component, as shown in Figure 6.2.

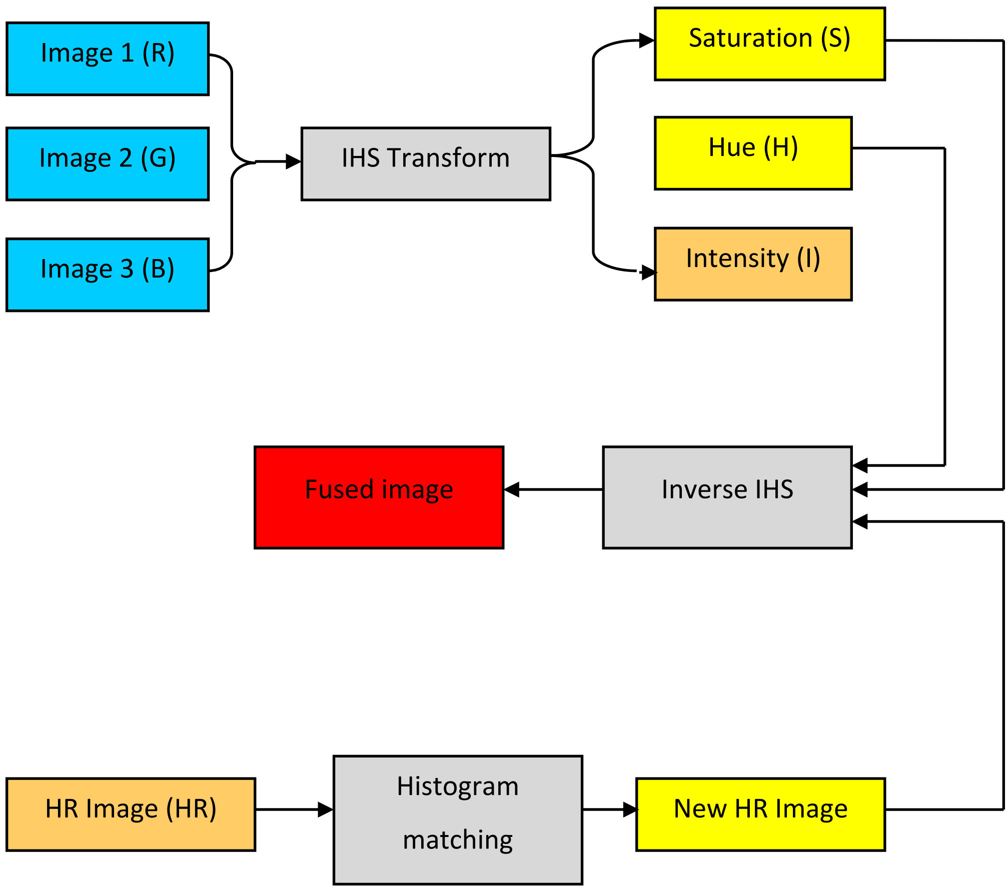


Figure 6.2: IHS fusion procedure.

IHS Fusion Steps:

1. Register the input images defined as *R*, *G*, and *B* to the same size as the high resolution image defined as HR.
2. Transform the *R*, *G*, and *B* false color image into the *IHS* component using one of the different transformations that have been developed to transfer a color image from the RGB space to the IHS space. The most common RGB- IHS conversion system is based on the following linear transformation [72], for each pixel *p*.

$$\begin{bmatrix} I^p \\ V_1^p \\ V_2^p \end{bmatrix} = \begin{bmatrix} \frac{1}{3} & \frac{1}{3} & \frac{1}{3} \\ \frac{-\sqrt{2}}{6} & \frac{-\sqrt{2}}{6} & \frac{\sqrt{2}}{3} \\ \frac{1}{\sqrt{2}} & -\frac{1}{\sqrt{2}} & 0 \end{bmatrix} \begin{bmatrix} R^p \\ G^p \\ B^p \end{bmatrix} \quad (6.1)$$

$$H^p = tan^{-1}\left(\frac{V_1^p}{V_2^p}\right) \quad (6.2)$$

$$S^p = \sqrt{\left(V_1^p\right)^2 + \left(V_1^p\right)^2} \quad (6.3)$$

3. Modify the *HR* image to account for differences related to acquisition techniques, this is usually performed by conventional histogram matching between the *HR* image and the intensity component *I* of the IHS representation [73], i.e. after computing the histogram of both *HR* image and the intensity component *I* of the IHS representation, the histogram of the intensity component *I* is used as reference to which *HR* image histogram was matched, the new *HR* image defined as *NRM*.
4. Replace the intensity component *I* by the *NRM* image.
5. Perform the inverse transformation to obtain the merged *R'G'B'* fused image using the relations [72].

$$\begin{bmatrix} R'^p \\ G'^p \\ B'^p \end{bmatrix} = \begin{bmatrix} 1 & \frac{-1}{\sqrt{2}} & \frac{1}{\sqrt{2}} \\ 1 & \frac{-1}{\sqrt{2}} & \frac{-1}{\sqrt{2}} \\ 1 & \sqrt{2} & 0 \end{bmatrix} \begin{bmatrix} HRM^p \\ V_1^p \\ V_2^p \end{bmatrix} \quad (6.4)$$

The generated fused image provides the full details of the *HR* image but introduces color distortion. This is because of the low correlation between the *HR* image and the intensity component *I*. As the intensity component is obtained as linear

combination of the different bands of the RGB image, a high correlation between these and the HR image can only be possible if the bandwidth of *HR* cover the entire range of the bandwidths of all RGB original bands.

6.3 Principal Component Analysis PCA Fusion

For the sake of completeness the theory of PCA is first described. PCA belong to linear transforms based on the statistical techniques. This method provides a powerful tool for data analysis which is often used in signal and image processing [74] as a technique for data compression, data dimension reduction, and data fusion.

PCA in signal processing can be described as a transform of a given set of n input vectors (variables) with the same length *K* formed in n-dimensional vector $\boldsymbol{x} = [x_1, x_2, \dots x_n]^T$ into a vector $\boldsymbol{y}$ according to

$$\boldsymbol{y} = \boldsymbol{P}(\boldsymbol{x} - \boldsymbol{m_x}) \tag{6.5}$$

This point of view enables to form a simple formula shown in equation 6.5 but it is necessary to keep in mind that each row of the vector $\boldsymbol{x}$ consists of *K* values belonging to one input. The vector $\boldsymbol{m_x}$ is the vector of mean values of all input variables defined by the relation

$$m_x = E\{\boldsymbol{x}\} = \frac{1}{K}\sum_{k=1}^{K} x_k \tag{6.6}$$

Matrix $\boldsymbol{P}$ is determined by the covariance matrix $\mathbf{C_x}$. Rows in $\boldsymbol{P}$ matrix are formed from the eigenvectors $\boldsymbol{e}$ of $\boldsymbol{C_x}$ordered according to corresponding eigenvalues in descending order. The evaluation of the $\boldsymbol{C_x}$ matrix is possible according to relation

$$\boldsymbol{C_x} = E\{(\boldsymbol{x} - \boldsymbol{m_x})(\boldsymbol{x} - \boldsymbol{m_x})^{\boldsymbol{T}}\} = \frac{1}{K}\sum_{k=1}^{K} \boldsymbol{x_k x_k^T} - \boldsymbol{m_x m_x^T} \tag{6.7}$$

As the vector $\boldsymbol{x}$ of input variables is *n*-dimensional it is obvious that the size of $\boldsymbol{C_x}$ is $n \times n$. The elements $\boldsymbol{C_x}(i, i)$ lying in its main diagonal are the variances of $\boldsymbol{x}$

$$\boldsymbol{C_x}(i, i) = E\{(\boldsymbol{x_i} - m_i)^{\mathbf{2}}\} \tag{6.8}$$

and the other values $\mathbf{C_x}(i, j)$ determine the covariance between input variables x_i, x_j.

$$\boldsymbol{C_x}(i, j) = E\{(\boldsymbol{x_i} - m_i)(\boldsymbol{x}_{\mathrm{j}} - m_{\mathrm{j}})\} \tag{6.9}$$

The rows of $\boldsymbol{P}$ in equation 6.5 are orthonormal so the inversion of PCA is possible according to the relation

$$\boldsymbol{x} = \boldsymbol{P^T y} + \boldsymbol{m_x} \tag{6.10}$$

Both IHS and PCA mergers are based on the same principal, i.e. to separate most of the spatial information of multispectral image from its spectral information by means of linear transforms. The IHS transform separates the spatial information of the multispectral image as the intensity (*I*) component. In the same way, PCA separates the spatial information of the image into the first principal component PC1.

PCA allows synthesizing the original bands creating new bands, the principal components, which pick up and reorganize most of the original information. In general, the first principal component PC1 collects the information that is common to all the bands used as input data in the PCA, i.e., the spatial information, while the spectral information that is specific to each band is picked up in the other principal components [75].

In this case, all original images constitute the input data. As a result of this transformation, we obtain non-correlated new bands, called the principal components.

The PCA method is similar to the IHS method, with the main advantage that an arbitrary number of bands can be used [75]. PC1 is replaced by the HR image, whose histogram has previously been matched with that of PC1. Finally, the inverse transformation is applied to the whole dataset formed by the modified HR image and the PC2 … PCn, as illustrated in Figure 6.3. The above illustrated PCA fusion obtaining new merged images with the spatial detail of HR image incorporated into them.

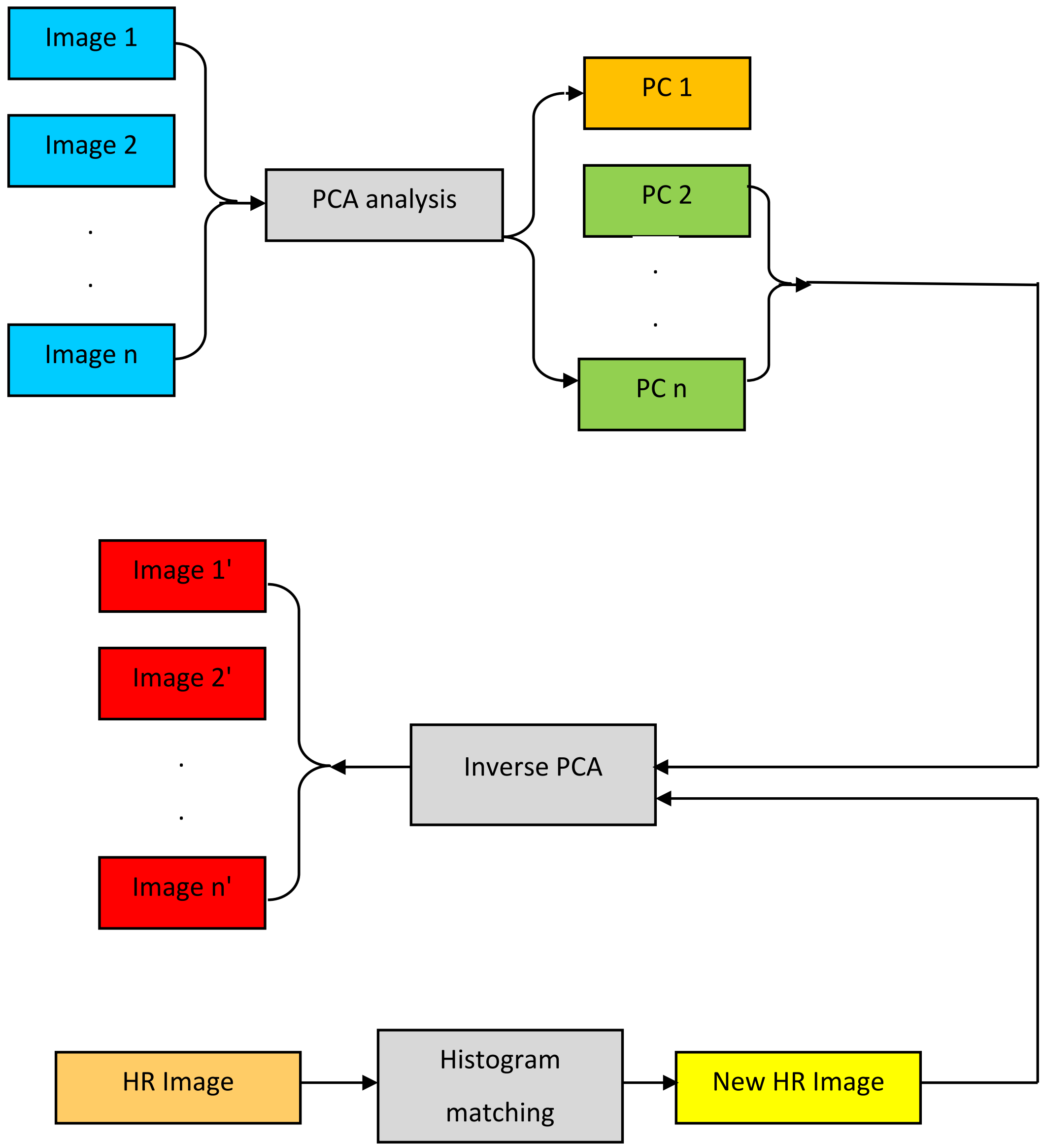


Figure 6.3: PCA fusion process.

If more than three images to be fused using IHS, principal component analysis PCA is proposed to be used as a first step in IHS fusion algorithm as shown in Figure 6.4, which gives the ability for arbitrary input IHS fusion system.

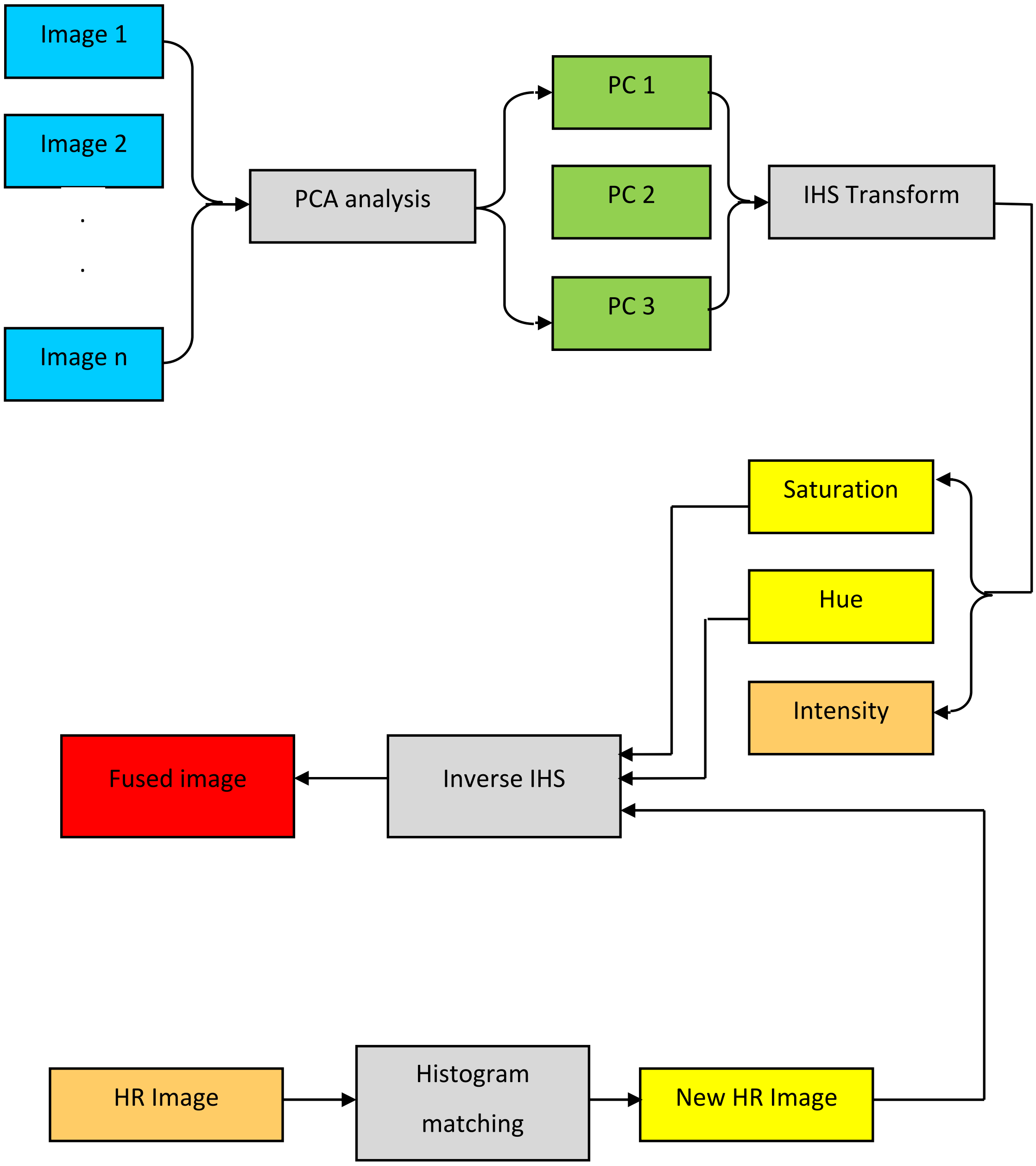


Figure 6.4: Arbitrary number of inputs IHS fusion system.

6.4 Improved IHS Based on Multi-Resolution Wavelet Decomposition (MWD) Fusion Technique

As mentioned above, the IHS fusion method usually can integrate color and spatial features smoothly. The intensity of the IHS fusion results is high and, if the correlation between the IHS intensity image and the HR image is high, the IHS fusion

can well preserve the color information. However, the color distortion is significant due to the low correlation between the intensity image and the HR image, especially when the input images and HR images are originally from different sensors.

On the other hand, the discrete wavelet transform (DWT) image fusion usually can better preserve color information than other fusion methods, such as, IHS, PCA, because the high-resolution spatial information from HR image is injected into all the three low-resolution multispectral bands. However, the spatial detail from HR image is often different from that of a multispectral band having the same spatial resolution. This difference may introduce some color distortion into the wavelet frame fusion results.

To better utilize the advantages of the IHS and the DWT fusion techniques, and to overcome the shortcomings of the two techniques, an integrated IHS and wavelet frame fusion approach is proposed in this dissertation to be applied NDE technology [76]. The shift invariant wavelet transform that could be obtained using á trous (with holes) algorithm overcomes image artifacts [77] and [78], so the un-decimated multi-resolution wavelet decomposition (MWD) or shift invariant discrete wavelet transform (SIDWT) was used for the IHS fusion improvement. The steps of this approach are shown in Figure 6.5, and summarized next

.

Improved IHS based on MWD Fusion Technique Steps:

1. **Registration:** All images are first registered.
2. **IHS Transform:** the multispectral image is transformed into IHS components as illustrated before.
3. **Histogram match:** To improve the fusion results as mentioned before, the histogram of the HR image and the intensity component *I* of the IHS color

space are matched and a new HR image (*NHR*) is obtained. An example of histogram matching is illustrated in Figure 6.5.

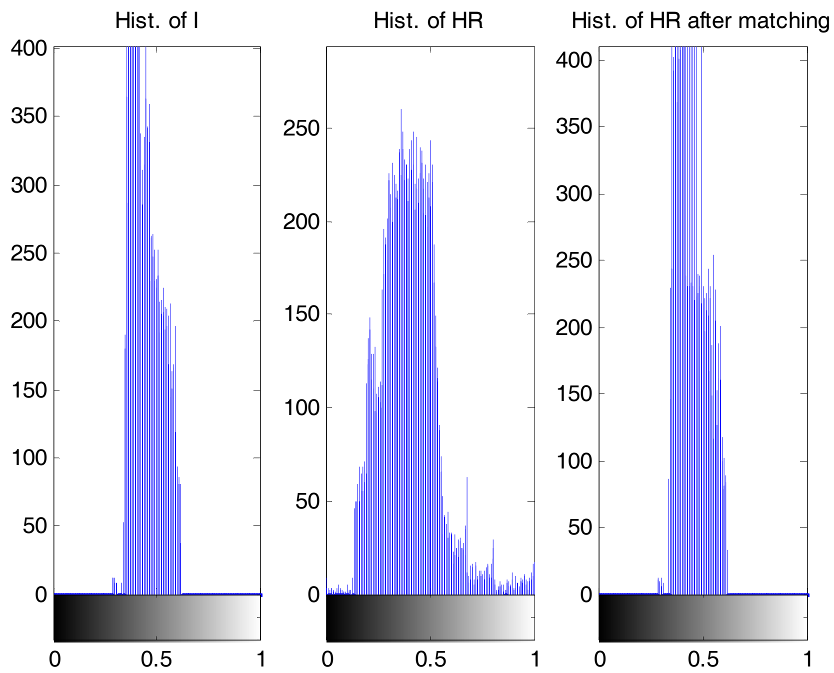


Figure 6.5: Example of histogram matching.

4. **SIDWT Decomposition:** Apply the un-decimated wavelet decomposition, to the intensity component *I* and to the corresponding histogram matched *NHR* image using the Daubechies four coefficient wavelet. Figure 6.6 and 6.7 show the first three approximation and detail coefficients of intensity component image I and HR image, where the HR image in this case taken as the coil resistance image at 1MHz.
5. **Fuzzy selection:** after the decomposition has been made a selection based on the application needed should be made. For example one possible application is to fuse optical image that has information about the rivets and joints for example with recently inspection EC images, in this case the best selection

would be to take the approximation of the optical image and the detail of the EC images. Another application is to replace high spatial resolution information with low spatial resolution of the fused images, in this case the detail of the *NHR* is selected, and this is the selection case taken in this study.

6. **Inverse SIDWT:** the shift invariant reconstruction transform applied to the selected wavelet coefficients to form the new intensity image.

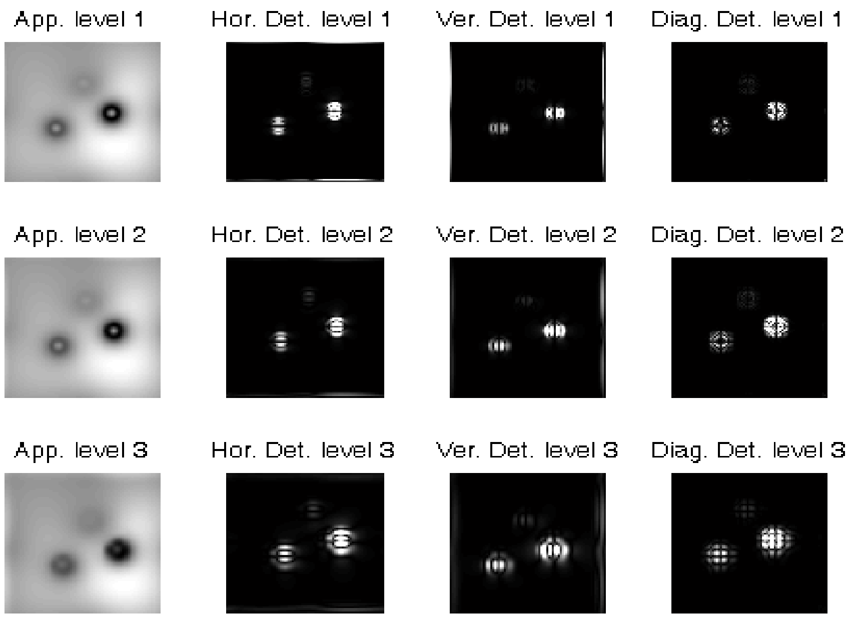


Figure 6.6: SIDWT approximation and detail coefficients at levels 1,2, and 3 of intensity component image *I*. Daubechies wavelets were used.

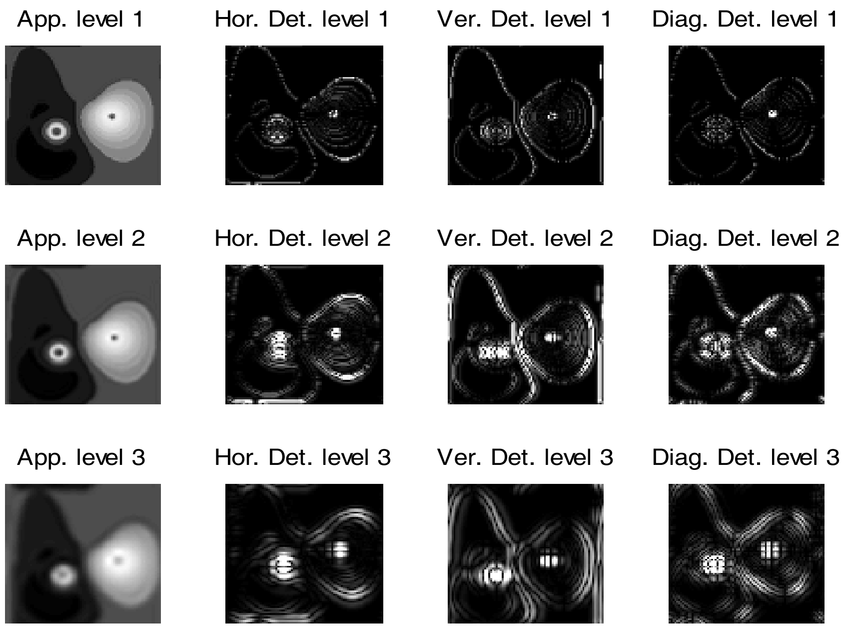


Figure 6.7: SIDWT approximation and detail coefficients at levels 1,2, and 3 of HR image (HR= R_5). Daubechies wavelets were used.

7. **Inverse IHS transform:** The final fused image is generated by transforming the new intensity image together with the hue and saturation components back into RGB space.

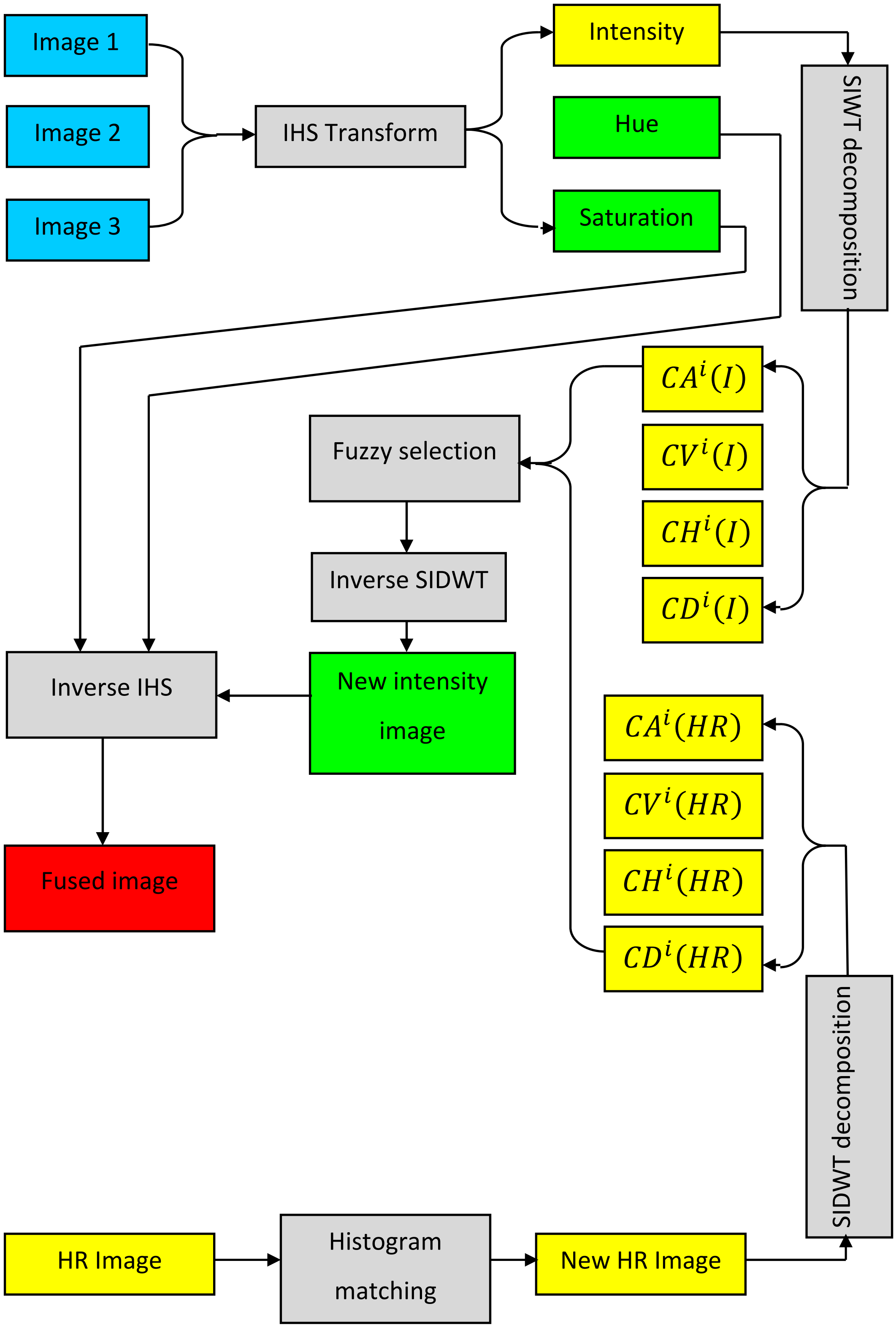


Figure 6.8: Improved IHS fusion based on MWD.

6.5 NDE Fusion Results

Through the simulation and experimental measurements, dozens of images were generated with conventional EC, pulsed EC, or optical, those carry complementary information about the sample under inspection. With the goal stated many time through this work, it is necessary to combine these information to achieve as much as possible of the benefits stated in table 2.1.

The evaluation of the IHS proposed fusion with application to NDE is done in two steps: the first is based simulation images, along with objective evaluation measures not requiring a reference image. The second uses experimentally acquired images with objective evaluation measures requiring a reference image. The reference image was generated based on the data sheet of the sample used for inspection. The objective evaluation measures used were discused previously in chapter 5.

6.5.1 Simulation Results

Figure 6.9 presents ten images generated with 128x128 resolution, representing probe resistance values (images R_1-R_5) on the top row, and probe inductance values (images L_1-L_5) on the bottom row. Images R_1 and L_1 on the left side correspond to lowest frequency while R_5 & L_5 on the right side correspond to high. All simulation images shown in this section are 128x128 resolution.

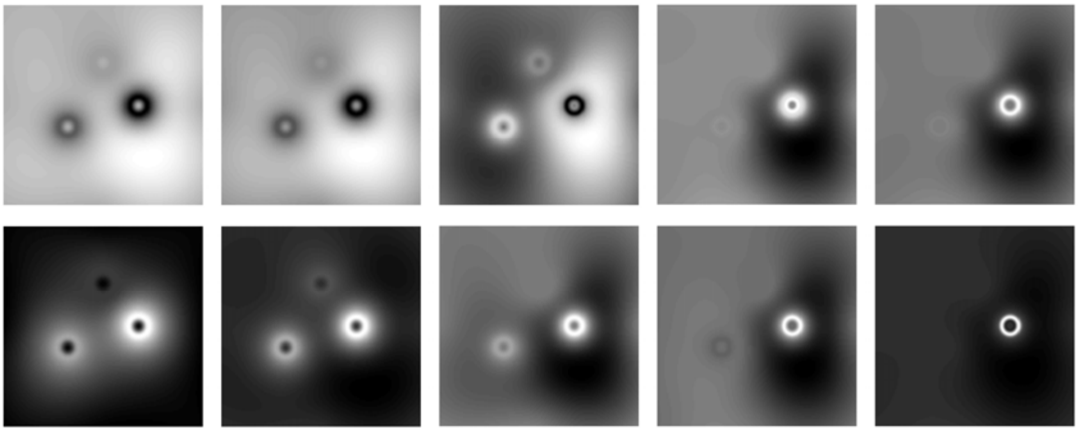


Figure 6.9: Ten images representing probe resistance values R_1-R_5 (top row, left to right) and inductance values L_1-L_5 (bottom row, left to right) corresponding to five different frequencies: 100 Hz, 1 kHz, 10 kHz, 100 kHz, and 1M Hz.

First some of fusion results are presented, before the presentation of a comparison of many fusion algorithms. Figure 6.10 presents fused images corresponding to simple RGB fusion technique, identifying three cracks at different depths. Figure 6.11 is based on IHS fusion with high frequency high-resolution image generated at 256x256. Examples of image fusion with shift invariant wavelet decomposition are presented in Figure 6.12, where Daubechies wavelets of order 4 are used. Figure 6.13 presents the first four principal components images computed from R_1-R_5 (the first row of Figure 6.9).

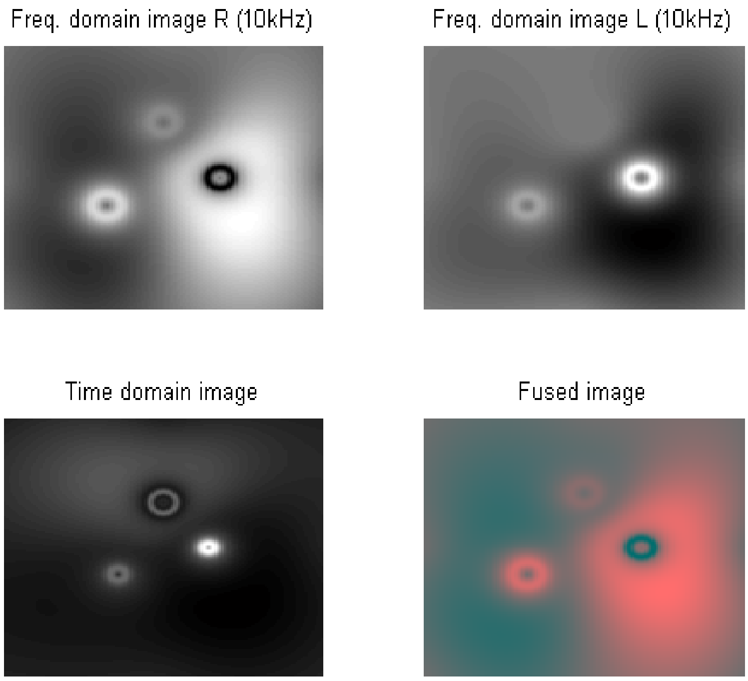


Figure 6.10: Simple fusion, with 2 frequency domain images and one time domain image.

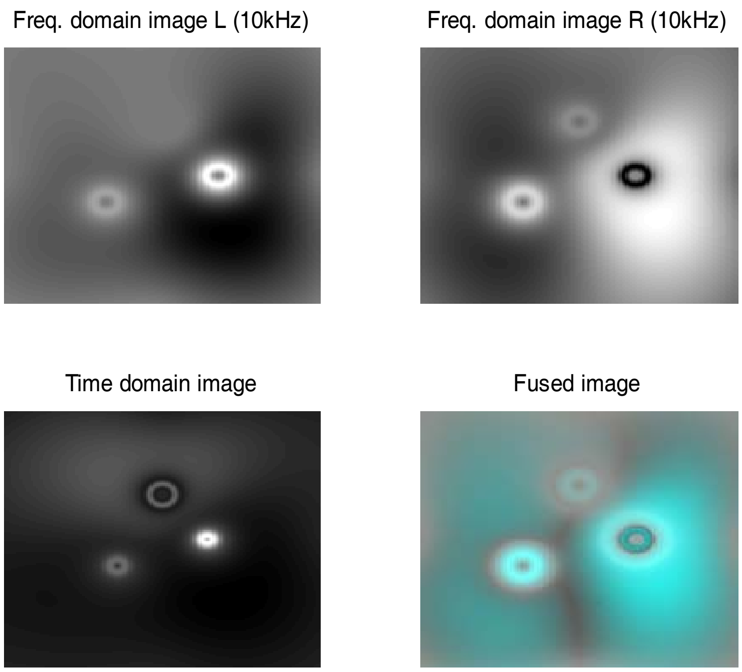


Figure 6.11: Fusion obtained with IHS transform.

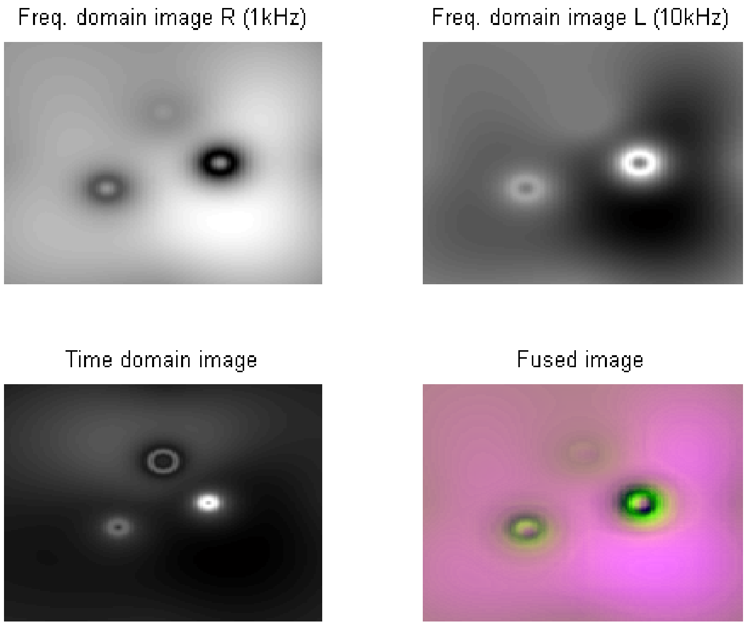


Figure 6.12: Fusion obtained with wavelet decomposition, where the high spatial resolution image was taken as R_5.

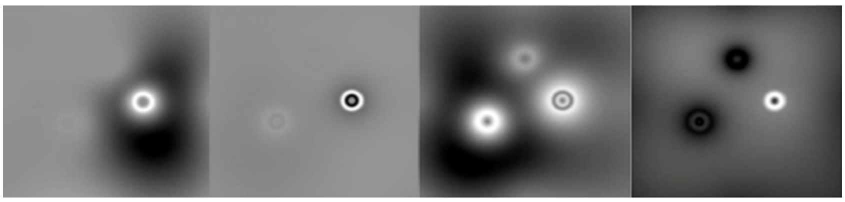
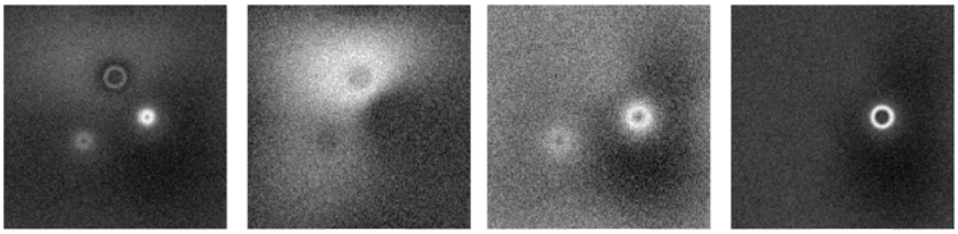


Figure 6.13: The first four principal components images computed from R_1-R_5 (the first row of Figure 6.9)

Four images were selected to make the comparison of fusion algorithms that have been applied to the NDE technology with the proposed fusion algorithms. The selection based on the sense that it may help in clear evaluation of these fusions. The selected simulation images presented in Figure 6.14 were two frequency domain images, and two time domain images used.



(a) (b) (c) (d)

Figure 6.14: Images used to evaluate the fusion algorithms, (a) maximum amplitude feature transient image, (b) time to maximum transient image, (c) probe L image at 10 kHz, (d) probe L at 1MHz as a HR.

The proposed IHS based fusion algorithms, called IHS presented in section 6.1, and the improved IHS based on MWD fusion termed as IHSW were compared with three fusion algorithms mostly presented in literature with application to NDE i.e. the Laplacian pyramid (LAP), the discrete wavelet transform (DWT), and the shift invariant discrete wavelet transform (SIDWT) presented in chapter 2. Further more there is the fact that human visual system processes information in a multiresolution fashion, i.e. there is the evidence that our human beings perform similar image decomposition [79 - 82]. This make sense since the final user is the human beings.

It has been reported in [83] that the results achieved by using Laplacian and Daubechie wavelet with different fusion rule were compared, and the consistency verification can only improve the result slightly, which may not introduce any difference to human observation [83]. So in this study the maximum frequency rule was used which selects the coefficients with the highest absolute value for LAP, DWT, and SIDWT fusion methods.

Figure 6.15 present the fusion results of the compared fusion algorithms where the input images for all were shown in Figure 6.14. Table 6.1 show the estimated quality measure for these fused images. Notice that the standard deviation (SD) and the entropy (H) illustrated that the IHS based methods are better, while the quality index (QE) idecates the opposite. There are six parameters in the QE performance measure which are determined via an optimization process that maximizes a correspondence measure between objective and subjective image fusion assessment results for a remote sensing images. It is thus not a relabile performance measure for general application, by investegating these quality measure it has been found that, a small change in these constant reverse the performance.

Note that the standard deviation is composed of the signal and noise parts. This metric would be more efficient in the absence of noise. It measures the contrast in the fused image. An image with high contrast would have a high standard deviation [84].

With the Gaussian noise added to the input images according to a predefined signal to noise ratio SNR, the performance of the fusion methods were compared with standard deviation SD, and entropy H, the results plotted in Figures 6.16 and 6.17 for SD and H respectively.

Note that in the color fused images shown in Figure 6.15 (d) and (e) high red component colors (orange in (d) and pink in (e)) correspond to high frequency information, and dark color correspond to low frequency information. In this case one can conclude that more red features means surface crack, and blacker features correspond to deeper crack.

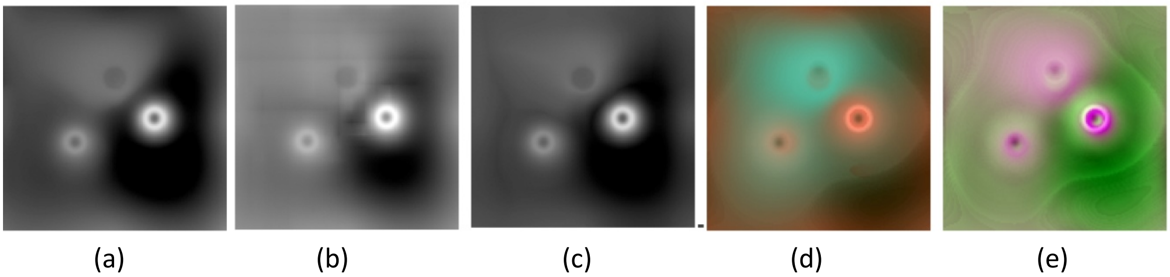


Figure 6.15: Fusion results of the images shown in Figure 6.14, (a) LAP, (b) DWT, (c) SIDWT, (d) IHS, (e) IHSW.

Table 6.1: Comparison between different quality measures for the fused images shown in Figure 6.15.

Fusion method	Standard deviation (SD)	Entropy (H)	quality index (QE)
Laplacian pyramid (LP)	30.1900	6.8695	0.7565
Discrete wavelet transform (DWT)	35.1318	6.8822	0.8077
Shift invariant discrete wavelet transform (SIDWT)	27.7046	6.7731	0.7588
Intensity hue saturation (IHS)	45.8145	7.1791	0.6008
Intensity hue saturation with wavelet (IHSW)	33.3772	7.3190	0.5484

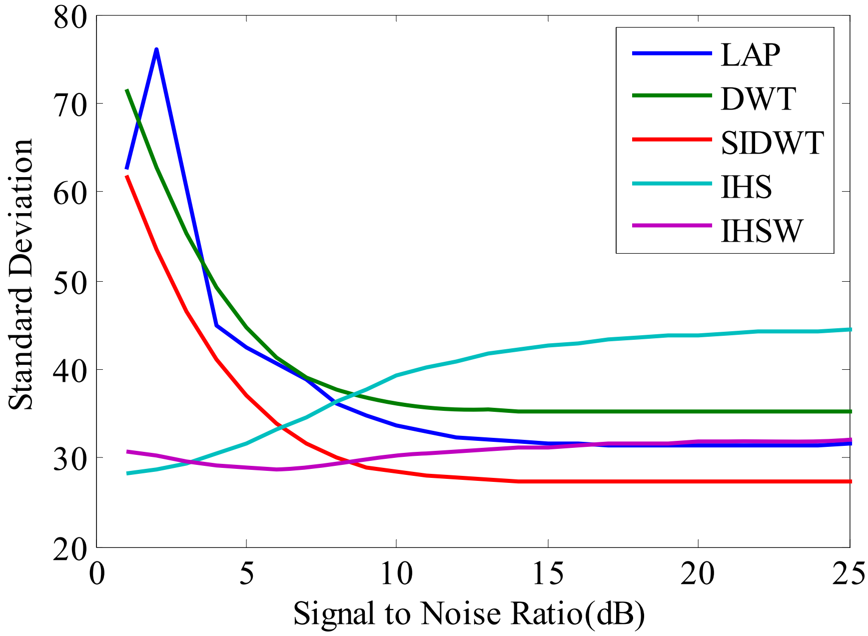


Figure 6.16: Performance of fusion with standard deviation quality metric.

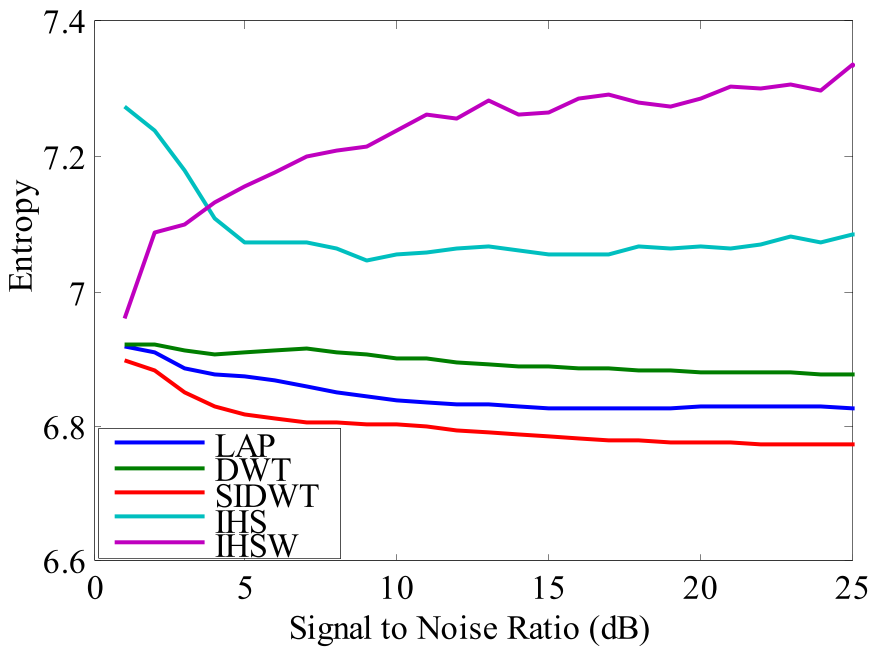


Figure 6.17: Performance of fusion with entropy quality metric.

It is clear from the plots shown in Figures 6.16, and 6.17 that the IHS based methods perform better. Also it is interested to figure out that the SD of the IHS based methods increases with the increase of SNR of input images. Entropy is used to measure the amount of uncertainty or information of an image, but it is sensitive to noise [84]. The dynamic range of SD and H are very small when the SNR exceed 20dB which is typically the acceptable image SNR.

Subjectively, IHS based fusion methods ranked higher than the other fusion methods.

6.5.2 Experimental Results

As mentioned in chapter 4, a lab for EC inspection was established in the electrical engineering department. Measurements have been obtained with the tools available. Figure 6.19 presents four images selected to measure the performance of the proposed

fusion algorithms with application to ND, and to figure out the increase in reliability of inspection using fusion techniques.

After the registration of EC to the optical image shown in Figure 6.18, the first three EC images of Figure 6.19 and the optical image were used as input to the fusion algorithms. IHS and IHSW use the three EC images as input to the IHS transform, and optical image as the HR image. Other fusion methods LAP, DWT, and SIDWT normally accept two input images only, and a multi-stage fusion process were conducted for the comparison to be far and use the same information.



Figure 6.18: Optical image of the test sample.

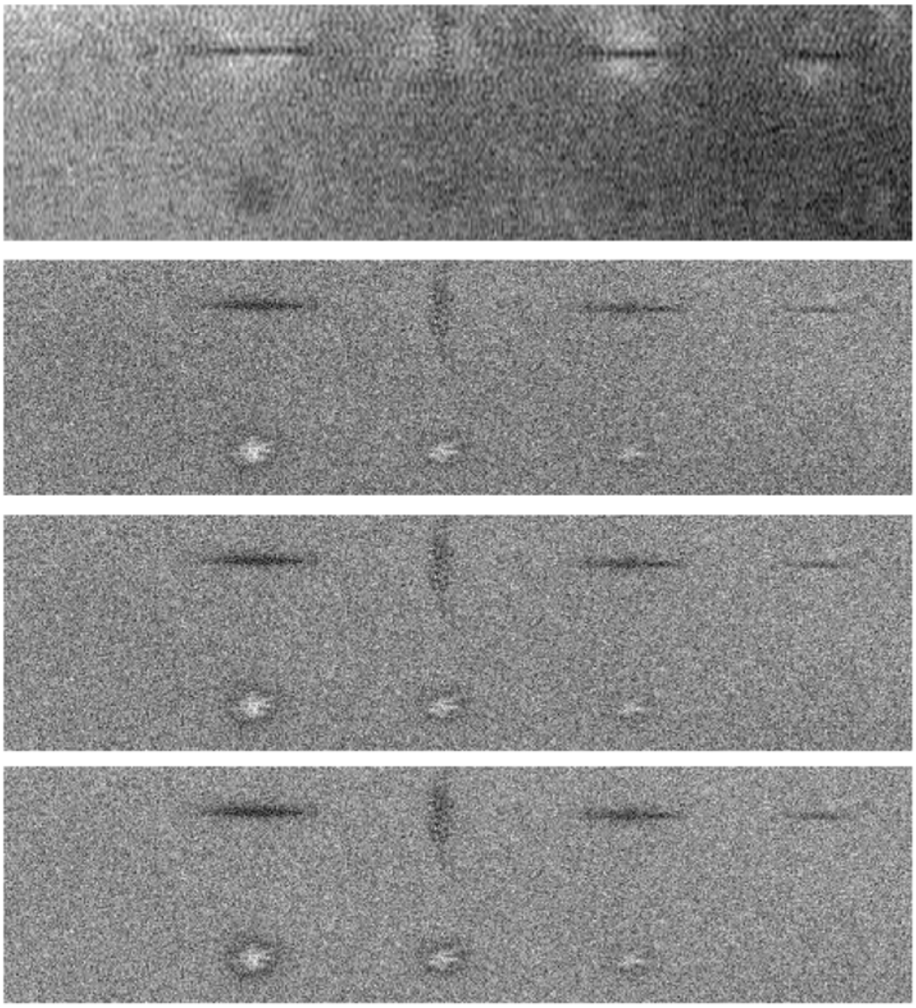


Figure 6.19: Experimental EC images at frequencies 10 kHz, 100 kHz, 300 kHz, and 800 kHz (top to bottom order).

With the Gaussian noise added to the experimental images used as inputs to the fusion methods according to a predefined signal to noise ratio SNR, the performance of the fusion methods were compared with five objective evaluation measures that requires reference image as discussed in chapter 5 namely, mutual information (MI), structure information, structural similarity (SSIM), correlation coefficient (Corr), root mean square error (RMSE), and peak signal to noise ratio (PSNR). The reference image was produced manually depending on the standard sample used.

Figures 6.21 through Figure 6.25 shows the results of the five mentioned metrics and how these metrics affected with noise. Where the result fused images are compared with the reference image.

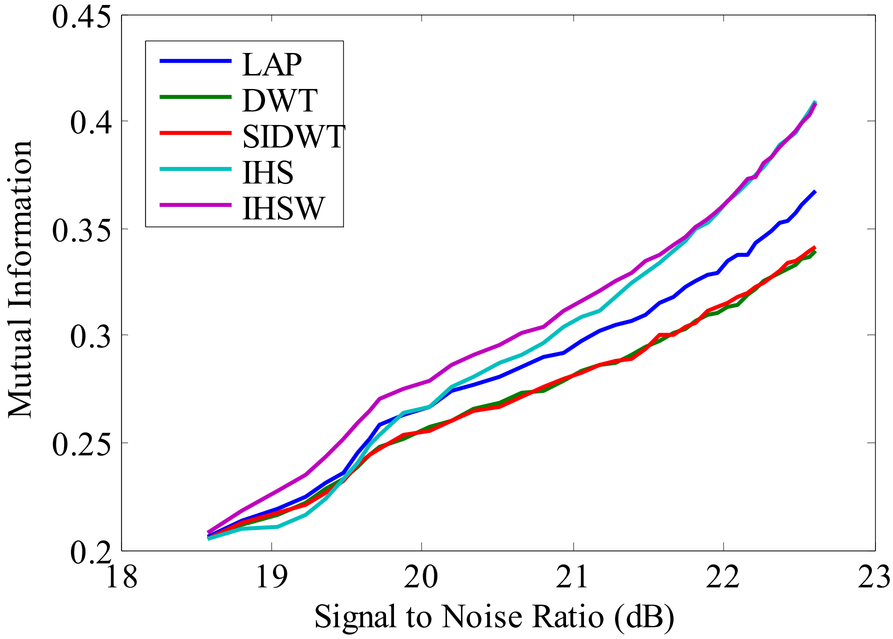


Figure 6.20: Performance of fusion with mutual information quality metric.

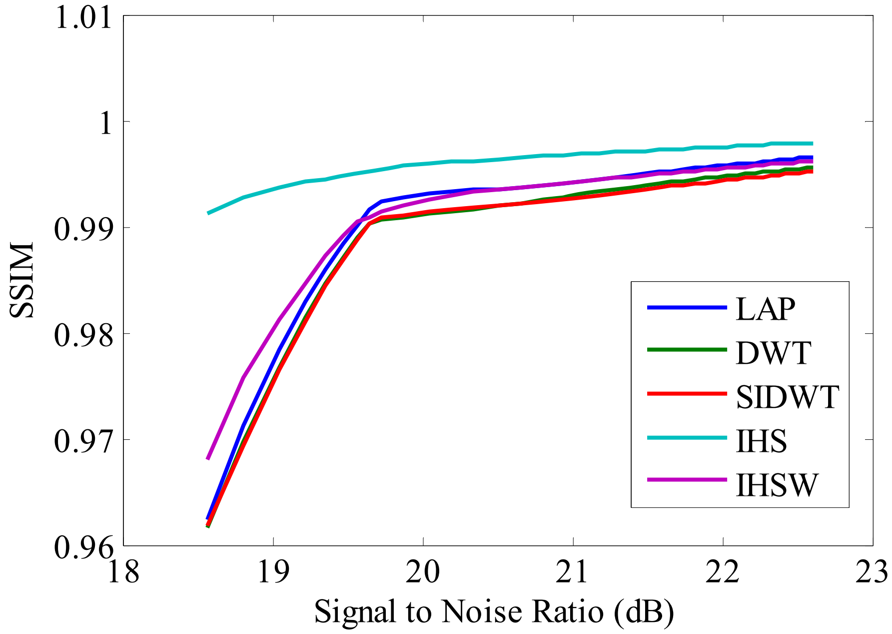


Figure 6.21: Performance of fusion with structure information, structural similarity quality metric.

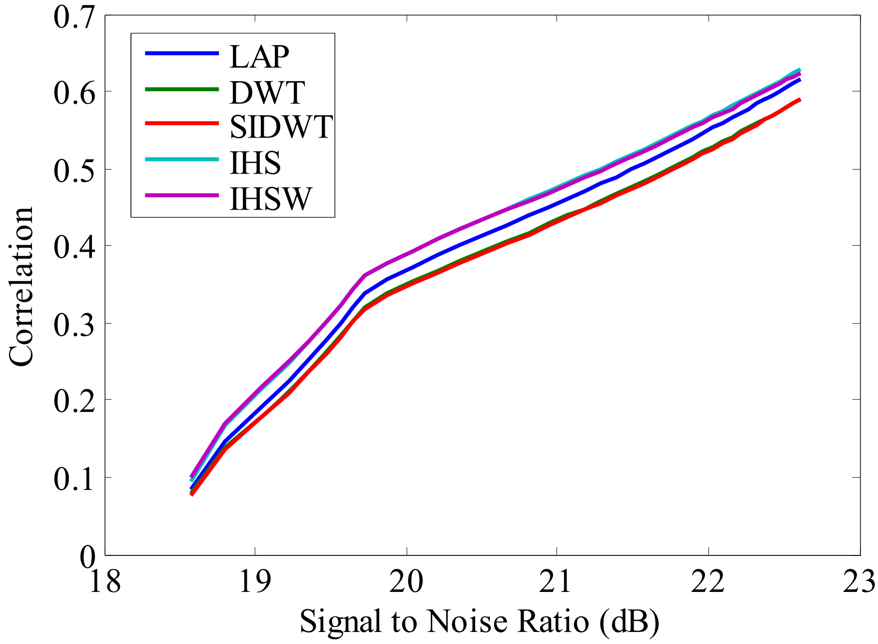


Figure 6.22: Performance of fusion with correlation quality metric.

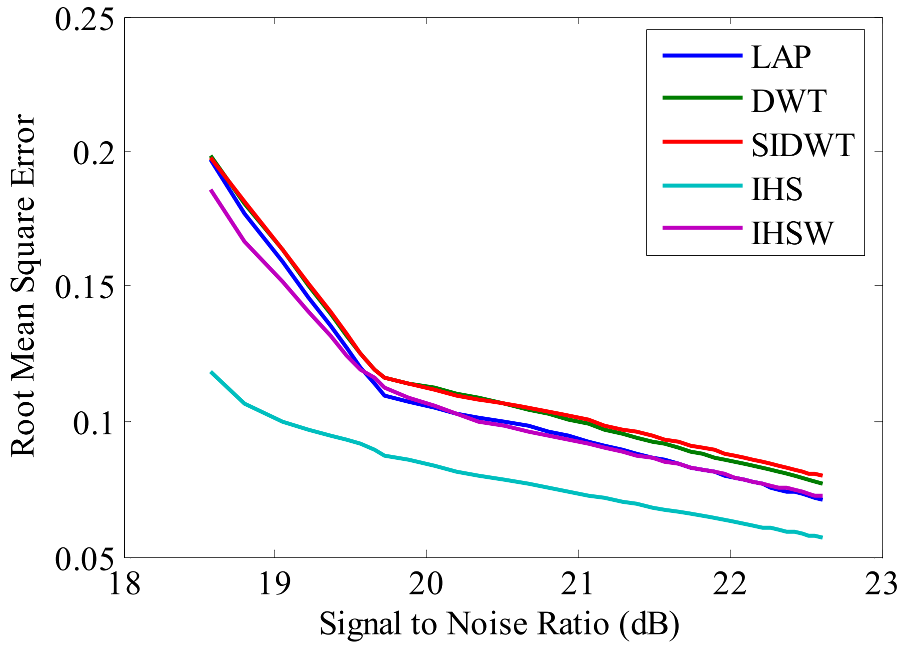


Figure 6.23: Performance of fusion with root mean square error quality metric.

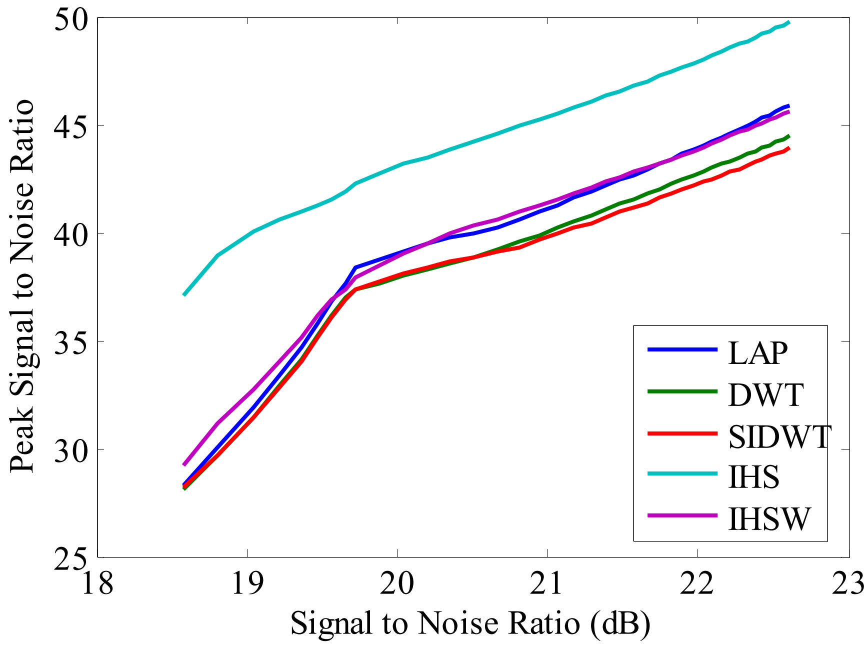


Figure 6.24: Performance of fusion with peak SNR quality metric.

Figures 6.20 to 6.24 shows that the IHS based methods perform better than the others three fusion methods for all performance measures used in the range of acceptable image SNR.

A comparison of using the three low frequency images and the three high frequency images are shown in Figure 6.25 and Figure 6.26 respectively, where the input images have SNR equals to 18, 25, 25 and 24 respectively. Notice that with use of high frequency images high resolution of the fuse images is obtained.

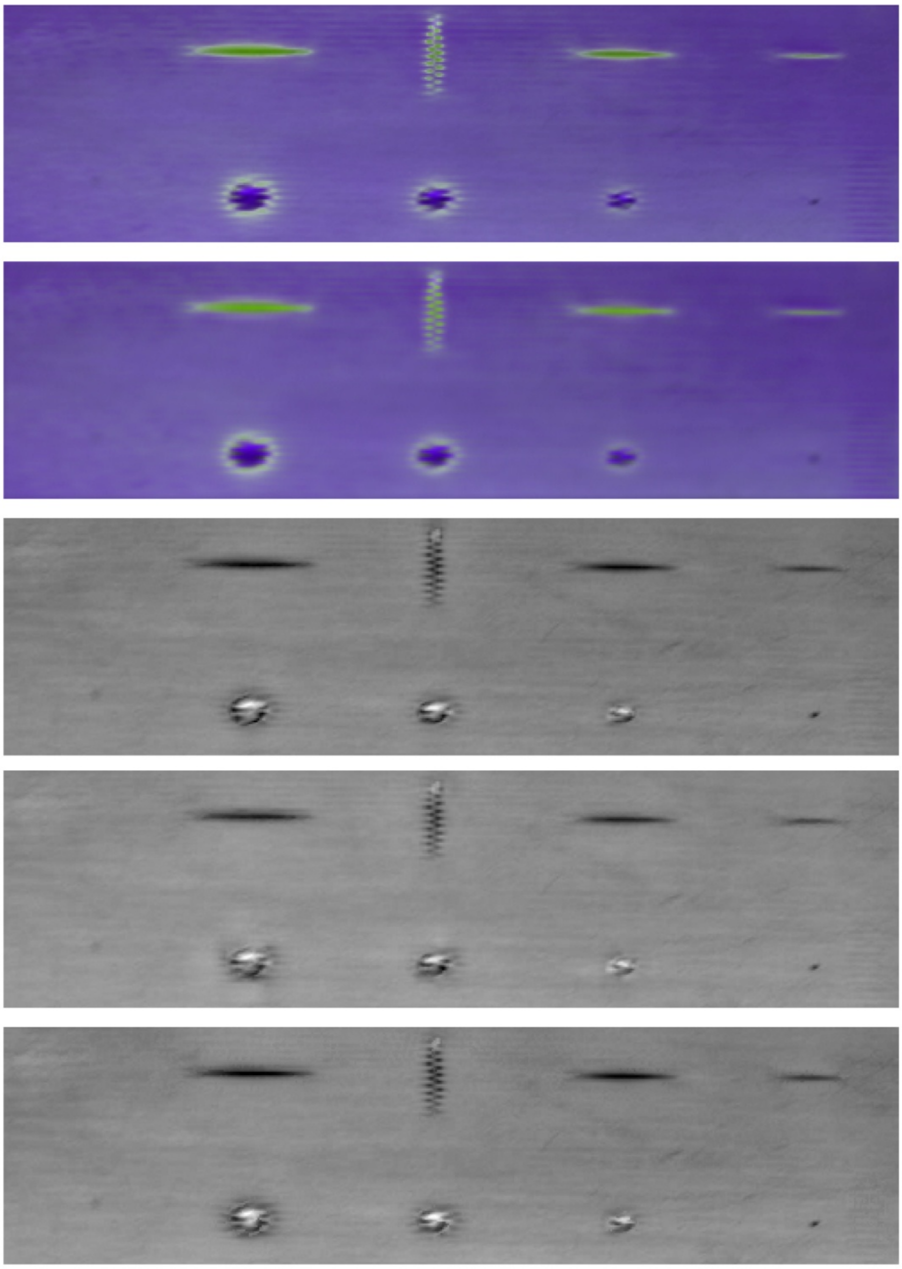


Figure 6.25: Fusion results with the first three low frequencies images shown in figure 6.18, and optical image (IHS, IHSW, SIDWT, DWT, LAP top to bottom respectively).

.

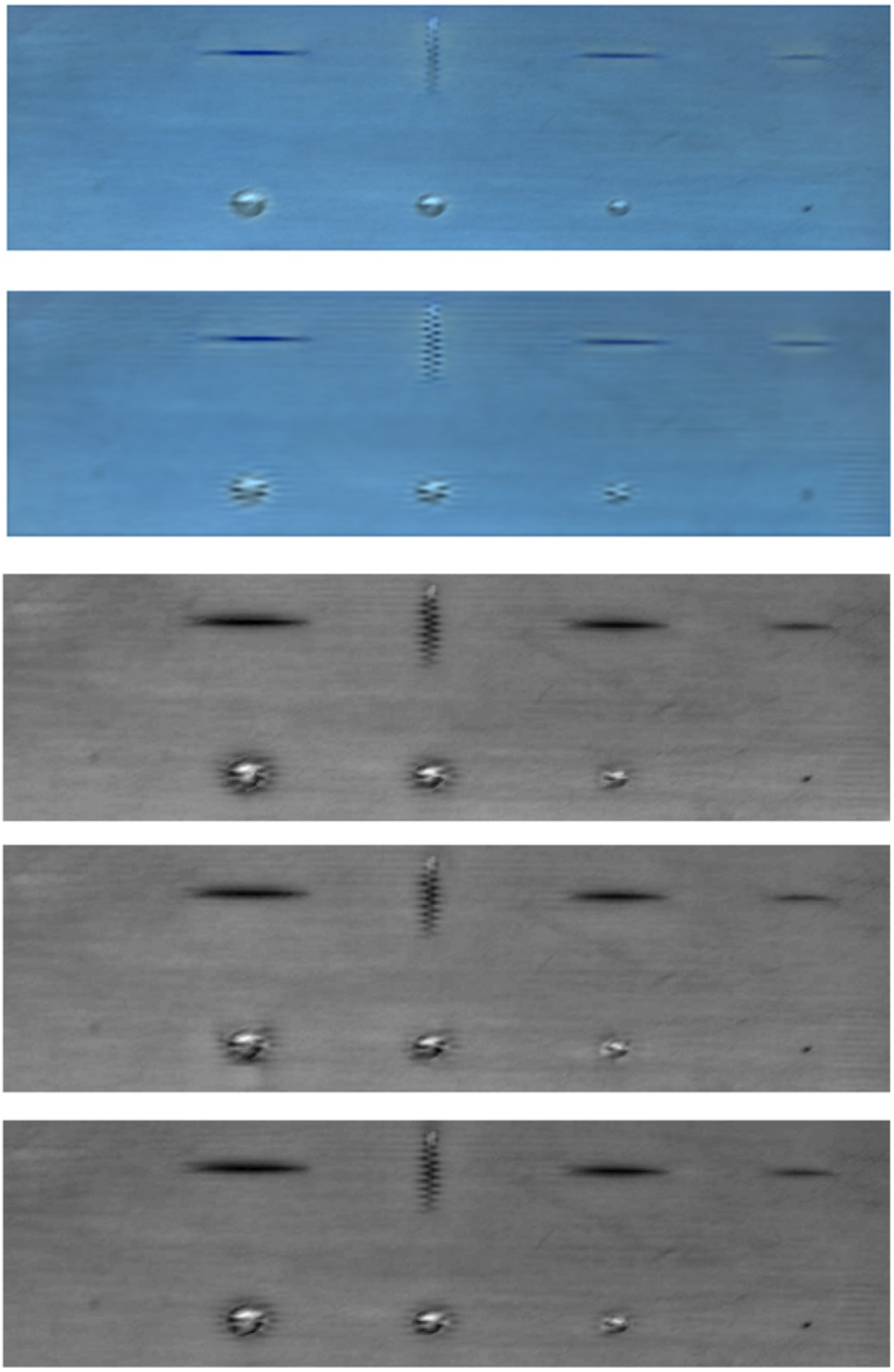


Figure 6.26: Fusion results with the last three high frequencies images shown in figure 6.18, and optical image (IHS, IHSW, SIDWT, DWT, LAP top to bottom respectively).

CHAPTER 7

CONCLUSIONS AND FUTURE WORK

This research results was made possible through support from King Abdulaziz City for Science and Technology (KACST), and Research Center, College of Engineering King Saud University. An EC laboratory has been established from provided funds.

Within this dissertation, the emerging concept of data fusion, particularly in NDE image fusion is used to develop a robust NDE system which can easily be adapted in industrial applications. The focus is directed to the emerging techniques based on eddy current (EC) inspection. EC techniques are considered to be the most promising electromagnetic inspection modality.

Although Electromagnetic testing are governed by the same physical laws, electromagnetic NDE techniques considerably depend on the frequency of operation. Techniques employing the static ($\omega = 0$) operation, such as the magnetic flux leakage, and the quasi-static frequency range such as eddy current methods are more commonly used in industry than higher frequency wave phenomenon methods. Modalities also exist at much higher frequency ranges such as thermal waves used in characterization coating adhesion and optical methods used in evaluating concrete and composite materials. Ionization frequency ranges as in x-ray techniques are used in

assessing residual stresses and crystalline texture of metal alloys. Hybrid techniques that operate at both high and low frequency ranges are also used as in the case of magneto-optic / eddy current imaging method.

Among the electromagnetic modalities the EC get more attention. Hazardous precautions are required for operation in the ionization frequency ranges, other band suffer from lack of time information. EC is one of the most sensitive and reliable methods for detecting surface and sub surface flaws. The characteristics responsible for such popularity of this technique include simplicity, versatility, high sensitivity, non-contact operation, couplant free testing and high speeds of testing. The interaction of induced alternating currents and fields with defects to produce noticeable changes in search coil impedance, or picked up signals are covered thoroughly in chapter 3.

The robustness of the developed system can be attributed to the fact that a system that is capable of extracting complementary segments of information from data collected from multiple NDE testing methods can offer increased insight relative to conventional NDE testing. Image fusion algorithms exploit both the redundancy and complementary information to enhance the resulting image. Redundant information is used to improve the SNR and complementary information is used to augment the overall information content, which increases the accuracy and reliability of inspection systems. Fusion algorithms and related subject such as objective evaluation measures of the fusion systems are presented in details in chapters 2, 5, and 6.

Various conclusions and contributions have been affirmed during the course work of this research. The eddy current has been well established in industry. This research has thus focused on this modality and invoked finite element (FE) computation model to obtain a robust analysis system for the interaction of excitation signal and object under test. Although, considerable effort was directed to establish

absolute analysis model, results revealed that differential analysis is essential in which the signal is disclosed from the dominant background signal that highly dependent on mesh noise.

Although, conventional EC is dominating industry use, EC imaging can cross the gap between eddy current testing ET and radiography tests RT. Data visualization is an effective intuitive method for understanding the results of testing. It is easier for the inspector to understand the testing results in the image format compared to a strip chart. An effective data visualization stage will help to improve the evaluation, especially in quantitative evaluation of types, locations, sizes and shapes of the defects. On the other hand, imaging reduces the necessity for highly qualified inspectors for interpretation of the results, since image help provide naturally reading of the data.

No single set of inspection parameters can provide robust information. Each method or technique include conditions required by that method, conditions to be met for technique application (access, physical contact and preparation) and requirements to adopt the probe or probe medium to the test object, this conditions perform the limitations of each method.

Pulsed eddy current (PEC) is spectrally rich, having low frequency and high frequency components simultaneously. The low frequency component reveal deep features while the high components can give better insight into the surface. No simple map however exists between time domain signal features and inspection information. Various techniques were used in this research to extract eddy current information from time domain signal.

A novel system is developed for fusing of conventional and pulsed eddy current images. The new system has been developed to fuse multi-spectral, multi-temporal, and multi-spatial information in EC images. The proposed fusion system

performs better than many other fusion system applied to NDE, according to the evaluation of many performance quality measures. The results illustrate the advantages of fusion in providing EC images that mimics optical images which are familiar to the human eye.

Noise analysis of normal distribution of the liftoff and conductivity parameters have been investigated, and validated with experimental work. These novel results indicate that the closeness to normal distribution is preserved as the frequency increased.

Various image quality metrics are presented to assess the quality of resulting fusion images. Eight objective fusion performance measures have been applied to the proposed fusion systems. The results of this objective evaluation are almost consistent with the subjective evaluation results. The developed system could easily be adopted to automate NDE in various industrial environments.

Although the research covered various details to develop a system which can easily be adapted in next generation NDE system various aspects cab be considered in the future to enhance this work.

Robotic system need to be improved to be able to work in field environment and still conserve their accuracy and robustness. The challenges include making the robot portable, requiring less intervention of human beings and acquiring more intelligence.

Crossing the gap between subjective judgment depending on human operators and automated system providing objective results is a wide field of contributions of the research society. This dissertation provided pioneering a start point defining quality metrics of fusion images for NDE applications, but the door is widely open for

researchers in the coming decades. Results taken from research fields such as remote sensing and medical data fusion can be very effective in this direction.

The results of PEC modeling are encouraging to investigate in the future the ability to formulate empirical equations that relate the features of the PEC picked up signal and the shape and size of the crack, hence quantify the discontinuity.

As Shannon provided his theory on channel capacity in 1948 which became later the essence of communication revolution, investigation of the information capacity of EC can be very promising in development of this field.

To the best of knowledge of the author, the dissertation presents a novel system implementing image fusion in EM NDE applications. The system implements the state of the art hardware robotic equipment and image processing. Industrialization of the system, however, should be feasible in the near future and could have major impact for NDE industry, in general and in the Saudi industry in particular.

The research can thus be an effective element which can be integrated with other elements to establish the edifice of industrial development in the Kingdom of Saudi Arabia.

REFERENCES

[1] Z. Liu, S. David Forsyth, J. P. Komorowski, K. Hanasaki, and T. Kirubarajan, "Survey: State of the Art in NDE Data Fusion Techniques." *IEEE Trans. Inst. Meas.,* vol. 56, no. 6, Dec. 2007.

[2] W. Lord, "Application of Numerical Field Modeling to Electromagnetic Methods of nondestructive Testing." *IEEE Trans. on Magnetics,* vol. 19, no. 6, pp. 2437-2442, Nov. 1983.

[3] I. Elshafiey, *Computational Aspect of Electromagnetic NDE phenomena.* :Ph. D. dissertation, Iowa State Univ., Ames, Iowa, 1994.

[4] T. R. Cantor, "Review of Penetrating Radar as Applied to Nondestructive Evaluation of Concrete." *In Situ/Nondestructive Testing of Concrete,* V. M. Malhotra, ed., American Concrete Institute, Detroit, 1984.

[5] J. Jarinen, J. Hartikainen, and M. Luukkala, "Quantitative Thermal Wave Characterization of Coating Adhesion Defects." *Review of Progress in Quantitative NDE, D. O. Thompson and D. Chimenti, eds.,* vol. 8B, pp. 1311-1319, Plenum, New York, 1989.

[6] F. Ansari, "Real Time Condition Monitoring of Conctere Structures by Embadded Optical Fibers Sensors." *Nondestructive Testing of Concrete Elements and Structures proceedings of sessions sponsored by the Engineering Mechanics Division of the American Society of Civil Engineers,* New York, 1992.

[7] S. Simms, "MOI: Magneto-Optic/Eddy Current Imaging." *Materials Evaluation,* Vol. 51, pp. 529-535, 1993.

[8] D. Vasic, V. Bilas, and D. Ambrus, "Pulsed Eddy Current Nondestructive Testing of ferromagnetic Tubes." *IEEE Trans. Instrumentation and Measurement,* vol. 53, no. 4, Aug. 2004.

[9] H. tsuboi, N. Seshima, I. Sebestyen, J. Pavo, S. Gyimothy, and A. Gasparics, "Transient Eddy Current Analysis of Pulsed Eddy Current Testing by Finite Element Method." *IEEE Trans. Magnetics,* vol. 40, no, 2, Mar. 2004.

[10] Y. A. Plotnikov, S. C. Nath, and C. W. Rose, "Defect Characterization in Multi-Layered Conductive Components with Pulsed Eddy Current." *Review of Progress in Quantitative Nondestructive Evaluation,* vol.21, 2002.

[11] R. C. Luo, and M. G. Kay, "Multisensor Integration and Fusion in Intelligent Systems." *IEEE Transactions on System, Man and Cybernetics,* vol. 19, no. 5, pp. 901–931, Sep. 1989.

[12] R. S. Blum and Z. Liu, *Multi-Sensor image fusion and its application.* New York : Taylor & Francis , 2006.

[13] R. R. Brooks, and S. S. Iyengar., *Multi-Sensor Fusion.* : Prentice Hall PTR, Upper Saddle River, NJ, 1998.

[14] D. L. Hall, *Mathematical Techniques in Multisensor Data Fusion.* : Artech House, ISBN 0-89006-558-6, 1992.

[15] X. E. Gros and K. Takahashi, "Fusion of NDT Data Improve Inspection of Composite Materials." *in Proceedings of 1998 Japanese Society of Nondestructive Inspection Spring Conference*, 1998, pp. 265–268.

[16] G. Simone and F. C. Morabito, "NDT image fusion using eddy current and ultrasonic data." *Int. J. Comput. Math. Elect. Electron. Eng*., vol. 20, no. 3, pp. 857–868, 2001.

[17] L. Udpa, and I. Elshafiey., "WINSADS: A New tool for Enhancing the Performance of Eddy Current Inspection of Aging Aircraft Wheels",." *Invited Paper, Proceeding of The 5th Joint NASA/FAA/DoD Conference on Aging Aircraft,* Hyatt-Orlando, Orlando, Florida Sep. 2001, pp. 10-13.

[18] Z. Wang, D. Ziou, C. Armenakis, D. Li, and Q. li., "A Comparative Analysis of Image Fusion Methods." *IEEE Trans. Geoscience and Remote Sensing,* vol. 43, no. 6, Jun. 2005.

[19] M. Mina, J. Yim, S. S. Udpa, and L. Udpa., "Two dimensional multi-frequency eddy current data fusion,." *in Review of Progress in QNDE,* vol. 15. New York: Plenum, 1996, pp. 2125–2132.

[20] M. Mina, S. S. Udpa, L. Udpa, and J. Yim., "A new approach for practical two dimensional data fusion utilizing a single eddy current probe." *in Review of*

Progress in QNDE, vol. 16, D. O. Thompson and D. E. Chimenti, Eds. New York: Plenum, 1997, pp. 749–755.

[21] J. Yim, S. S. Udpa, M. Mina, and L. Udpa., "Optimum filter based techniques for data fusion." *in Review of Progress in QNDE,* vol. 15, D. O. Thompson and D. E. Chimenti, Eds. New York: Plenum, 1996, pp. 773–780.

[22] Z. Liu, K. Tsukada, K. Hanasaki, and M. Kurisu., "Two-dimensional eddy current signal enhancement via multifrequency data fusion." *Res. Nondestruct. Eval.,* vol. 11, no. 3, pp. 165–177, Nov. 1999.

[23] X. E. Gros, P. Strachan, and D. W. Lowden., "Theory and implementation of NDT data fusion." *Res. Nondestruct. Eval.,* vol. 6, no. 4, pp. 227–236, Dec. 1995.

[24] Y. W. Song and S. S. Udpa, "A new morphological algorithm for fusing ultrasonic and eddy current images." *in Proc. IEEE Ultrason. Symp.,* 1996, pp. 649–652.

[25] X. E. Gros, Z. Liu, K. Tsukada, and K. Hanasaki., "Experimenting with Pixel-level NDT Data Fusion Techniques." *IEEE Trans. Instrumentation and Measurement,* vol. 49, no. 5, Oct. 2000.

[26] Z. Liu, X. E. Gros, K. Tsukada, K. Hanasaki, and K. Takahashi., "The use of wavelets for pixel level NDT data fusion." *in Proc. 2nd Jpn.–US Symp. Advances NDT,* Kahuku, HI, 1999, pp. 474–477.

[27] G. Y. Tian, A. Sophian, D. Taylor, and J. Rudlin., "Multiple sensors on pulsed eddy-current detection for 3-D subsurface crack assessment." *IEEE Sensors J.,* vol. 5, no. 1, pp. 90–96, Feb. 2005.

[28] A. J. Volponi, T. Brotherton, R. Luppold, and D. L. Simon., "Development of an Information Fusion System for Engine Diagnostics and Health Management." *NASA/TM—2004-212924,* Cleveland, OH: NASA, Feb. 2004.

[29] V. Kaftandjian, Y. Min Zhu, O. Dupuis, and D. Babot, "The Combined Use of the Evidence Theory and Fuzzy Logic for Improving Multimodal Nondestructive Testing Systems." *IEEE Trans. Instrumentation and Measurement,* vol. 54, no. 5, Oct. 2005.

[30] C. Chi, and Yen L. P., "A Noval Multiphysics Sensing Method Based on Thermal and EC Techniques and its Application for Crack Inspection." *Proceedings of the 2008 IEEE International Conference on Sensor Network, Ubiquitous, and Trustworthy Computing,* pp. 475-479, 2008.

[31] Z. Liu, F. Abbas, and M. Nezih., "Application of Dempster-Shafer Theory for Fusion of Lap Joints Inspection Data7." *Proceedings of SPIE, the International Socity for Optical Engineering,* vol. 6176, pp. 6176J-6176J.9, 2006.

[32] T. Chady, R. Sikora, G. Psuj, M. Enokizono, and T. Todaka., "Fusion of electromagnetic inspection methods for evaluation of stress-loaded steel samples." *IEEE Trans. Magn.,* vol. 41, no. 10, pp. 3721–3723, Oct. 2005.

[33] A. M. Djafari, "Fusion of X-ray and geometrical data in computed tomography for nondestructive testing applications." *in Proc. Int. Conf. Inf. Fusion,* Annapolis, MD, Jul. 2002, pp. 309–316.

[34] V. Kaftandjian and N. Francois,, "Use of data fusion methods to improve reliability of inspection: Synthesis of the work done in the frame of a European thematic network,." *in Proc. 8thECNDT ,* Barcelona, Spain Jun. 2002, vol. 8, no. 2.

[35] L. Udpa,, "Neural networks for NDE." *in Proc. IV Int. Workshop: Advances Signal Process. Nondestructive Eval. Mater.,* Quebec City, QC, Canada, Aug. 2001.

[36] Z. Liu, X. E. Gros, K. Tsukada, K. Hanasaki, and K. Takahashi., "The use of wavelets for pixel level NDT data fusion." *in Proc. 2nd Jpn.–US Symp. Advances NDT*, Kahuku, HI, 1999, pp. 474–477.

[37] B. J. Matuszewski, L. K. Shark, and M. R. Varley., "Region-based wavelet fusion of ultrasonic, radiographic and shearographic nondestructive testing images." *in Proc. 15thW orld Conf. Nondestructive Testing,* Rome, Italy, Oct. 2000.

[38] M. Brassard, A. Chehbaz, A. Pelletier, and D. S. Forsyth., "Combined NDT inspection techniques for corrosion detection of aircraft structures." *in Proc. 15thWorld Conf. Nondestructive Testing,* Rome, Italy, Oct. 2000.

[39] J. Yim, S. S. Udpa, L. Udpa, and W. Lord., "“Neural network approaches to data fusion." *in Review of Progress in QNDE, Vol. 14, D. O. Thompson and D. E. Chimenti, Eds.* New York: Plenum, 1995, pp. 819–826.

[40] J. Yim,, *Image fusion using multiresolution decomposition and LMMSE filter.* : Ph.D. dissertation, Iowa State Univ., Ames, IA, 1995.

[41] R. C. Gonzalez and R. E. Woods, *Digital Image Processing.* : Addison–Wesley, 1992.

[42] P. J. Burt and E.H. Adelson, "The Laplacian pyramid as a compact image code." *IEEE Transactions on Communications,* vol. 31, no. 4, pp. 532–540, 1993.

[43] A. Toet, "Multiscale Contrast Enhancement with Application to Image Fusion." *Optical Engineering,* vol. 31, no. 5, pp. 1026–1031, May 1992.

[44] R. S. Blum and Z. Liu, *Multi-sensor image fusion and its applications.* Boca Raton : CRC Press, Taylor & Francis Group, 2006.

[45] S. Li, "Using the discrete wavelet frame transform to Merge Landsat TM and SPOT Panchromatic Images." *Information Fusion,* Vol. 3, pp. 17-23, 2002.

[46] D. Vasic, V. Bilas, and D. Ambrus., "Pulsed Eddy Current Nondestructive Testing of ferromagnetic Tubes." *IEEE Trans. Instrumentation and Measurement,* vol. 53, no. 4, Aug. 2004.

[47] H. J. Krause, G. I. Panaitov, and Y. Zhang., "Conductivity Tomography for Non-Destructive Evaluation Using Pulsed Eddy Current with HTS SQUID Magnetometer." *IEEE Trans. Applied Superconductivity,* vol. 13, no. 2, Jun. 2003.

[48] G. Y. Tian, A. Sophian, D. Taylor, and J. Rudlin., "Multiple Sensors on Pulsed Eddy Current Detection for 3-D Subsurface Crack Assessment." *IEEE Senssors Journal,* vol. 5, no. 1, Feb. 2005.

[49] M. Sadiku, *Numerical Techniques in Electromagnetics.* Boca Raton, Florida : CRC Press LLC, 2001.

[50] O. Biro and K. Preis, "On the use of the magnetic vector potential in the finite element analysis of three-dimensional eddy currents." *IEEE Trans. Magn.,* vol. 25, pp. 3145–3159, Jul. 1989.

[51] M. Sadiku,, "A simple introduction to finite element." *IEEE Trans. on Education,* vol. 32, no. 2, pp. 85-93.

[52] D. N. Dyck, G. Gilbert, B. Forghani, and J. P. Webb., "An NDT Pulse Study With TEAM Problem 27." *IEEE Trans. Magnetics,* vol. 40, No. 2, Mar. 2004.

[53] U. Patel, and D. Rodger, "Finite Element Modelling Of Pulsed Currents For Nondestructive testing." *IEEE Trans. On Magnetics,* vol. 32, no. 3, May 1996.

[54] Documentation, ANSYS., http://www.ansys.com. [Online]

[55] K. Chomsuwan, S. Yamada, M. Iwahara, H. Wakiwaka, and S. Shoji., "Application of Eddy-Current Testing Technique for High-Density Double-Layer Printed Circuit Board Inspection." *IEEE Trans. Magnetics,* vol. 41, no. 10, Oct. 2005.

[56] H. Tsuboi, N. Seshima, I. Sebestyen, J. Pavo, S. Gyimothy, and A. Gasparics., "Transient Eddy Current Analysis of Pulsed Eddy Current Testing by Finite Element Method." *IEEE Trans. Magnetics,* vol. 40, no, 2, Mar. 2004.

[57] A.B. Carlson, et al., *Communication Systems: An Introduction to Signals and Noise in Electrical Communication, 4th Ed.* : McGraw Hill, Boston, 2002.

[58] S. J. Lee and S. H. Song, "Magnetooptic Sensor for Remote Evaluation of Surfaces." *IEEE Trans. Magn,* vol. 41, pp. 2257-2259, 2005.

[59] C. Athanasios and L. M. Malkinski, "GMR Multilayers on a New Embossed Surface." *IEEE Trans. Magn.,* vol. 40, 2004.

[60] www.rohmann.de.[Online].

[61] www.staubli.com/en/robotics.[Online].

[62] www.ni.com/dataacquisition.[Online].

[63] www.olymousNDT.com. [Online]

[64] B. Zitova, and J. Flusser., "Image registration methods: a survey." *Image and Vision Computing,* vol. 21, 2003, pp. 977–1000.

[65] G. Xin, W. Chao, Z. Weiguo, W. Ji, L. Hao, "The analysis and application of spline interpolation for multisensor and multiresolution image registration."

Geoscience and Remote Sensing Symposium, 2003. IGARSS apos;03. Proceedings. 2003 IEEE International, vol. 2, Jul. 2003 pp. 1056 - 1058.

[66] Z. Wang, A. Conrad Bovik, H. Rahim Sheikh, and E. P. Simoncelli., "Image Quality Assessment: From Error Visibility to Structural Similarity." *IEEE trans. on image processing*, Vol. 13, NO. 4, 2004.

[67] G. Qu, D. Zhang, and P. Yan, "Information measure for performance of image fusion." *Electronic letter,* vol. 38, 2002.

[68] C. S. Xydeas, and V. Petrovid, "Opjective pixel level image fusion performance measure." *In Proc. SPIE,* Orlando, FL, vol. 4051, 88-99, 2000.

[69] Y. Chen, and R. S. Blum, "Experimental Tests of Image Fusion for Night Vision." *8th International Conference on Information Fusion,*ECE Dept., Lehigh Univ. Bethlehem, PA, USA,2005.

[70] X. E. Gros, Z. Liu, K. Tsukada, and K. Hanasaki., "Experimenting with pixel level NDT data fusion techniques." *IEEE Trans. Instrum. Meas.,* vol. 49, no. 5, pp. 1083–1090, Oct. 2000.

[71] S. Tania, *Image Fusion: Algorithms and applications.* London : Academic Press is an imprint of Elsevier, 2008.

[72] M. G. Audicana, "A Low Computational-Cost Method to Fuse IKONOS Images Using the Spectal Response Function of Its Sensors." *IEEE Trans. Geosci. Remote Sens.* vol. 44, 2006, pp. 1683-1691.

[73] J. Nunez,, X. Otazu, O. Fors, A. Prades, V. Pala, and R. Arbiol, "Multiresolution based image fusion with additive wavelet decomposition." *IEEE Trans. Geosci. Remote Sens.,* vol. 37, no. 3, pp. 1204 - 1211, May 1999.

[74] R. C. Gonzales and R. E. Woods, *Digital Image Processing.* : Printice Hall, 2002.

[75] P. S. Chavez and A. Y. Kwarteng, "Extracting spectral contrast in Landsat Thematic Mapper image data using selective principal component analysis." *Photogramm. Eng. Remote Sens.,* vol. 55, pp. 339 - 348, Mar. 1989.

[76] I. Elshafiey, A. Algarni,, and M. Alkanhal, "Image fusion based enhancement of eddy current nondestructive evaluation", *International Journal of Applied Electromagnetics and Mechanics*, Volume 28, Number 1-2, 2008.

[77] Z. Wang, D. Ziou, C. Armenakis, D. Li, and Q. Li, "A Comparative Analysis of Image Fusion Methods." *IEEE Transactions on Geoscience and Remote Sensing.* vol. 43, no. 6, pp. 1391-1402, Jun. 2005.

[78] J. E. Fowler, "The Redundant Discrete Wavelet Transform and Additive Noise." *IEEE Signal Processing Letters.* vol. 12, no. 9, pp. 629 - 632, Sep. 2005.

[79] E. H. Adelson, C. H. Anderson, J. R. Bergen, P. J. Burt, and J. M. Ogden., "Pyramid Methods in Image Processing." *RCA Engineer,* vol. 29, no. 6, pp. 33–41, 1984.

[80] Bergen, D. J. Heeger and J. R., "Pyramid-based Texture Analysis/Synthesis." *ACM Computer Graphics Proceedings,* 1995, pp. 229–236.

[81] E. H. Adelson and E. Simoncelli, "Orthogonal Pyramid Transforms for Image Codinging." *Proceedings of SPIE,* vol. 845 of Visual Communications and Image Processing II, pp. 50–54, 1987,.

[82] Z. Liu, X. E. Gros, K. Tsukada, K. Hanasaki, and K. Takahashi., "The Use of Wavelets for Pixel Level NDT Data Fusion." *Proceedings of Second Japan-US Symposium on Advance NDT,* Hawaii, USA, 1999, pp. 474–477.

[83] Z. Liu, *Studies on Data Fusion of Nondestructive.* Kyoto : Ph. D. dissertation, Kyoto Univ., Mar. 2000.

[84] V.P.S. Naidu and J.R. Raol, "Pixel-level Image Fusion using Wavelets and Principal Component Analysis." *Defence Science Journal*, vol. 58, no. 3, pp. 338-352, May 2008.

LIST OF PUBLICATIONS

1. A. Algarni, I. Elshafiey, and M. Alkanhal, “Spectrally Enhanced Eddy Current Inspection Exploiting Fusion Techniques,” *Presented in the Quantitative NDE International Conference, QNDE 2008*, University of Illinois, Chicago, Illinois, USA, July 20-25, 2008.

2. A. Algarni, I. Elshafiey, and M. Alkanhal, “Advanced Tool for Industrial Eddy Current Inspection Systems,” *Presented in the 7th Engineering Conference and Exhibition*, Riyadh, Saudi Arabia, December 2-5, 2007.

3. I. Elshafiey, A. Algarni,, and M. Alkanhal, “Image fusion based enhancement of eddy current nondestructive evaluation”, *International Journal of Applied Electromagnetics and Mechanics*, Volume 28, Number 1-2, 2008.

4. I. Elshafiey, A. Algarni, and M. Alkanhal, “Transfusion of Time-Domain and Frequency-Domain Eddy Current Signals,” *Presented in the Fourth Middle East Non-Destructive Testing Conference and Exhibition*, Manama, Bahrain, December 2-5, 2007.

5. I. Elshafiey, M. Alkanhal, and A. Algarni, “Image Fusion Based Enhancement of Eddy Current Nondestructive Evaluation,” *Presented at the 13th International Symposium of Applied Electromagnetics and Mechanics*, ISEM 2007, Michigan State University, East Lansing, MI, USA, September 9-12, 2007.

6. A. Algarni, I. Elshafiey, and M. Alkanhal, “Multimodal Image Fusion for Next Generation NDE Systems, ” Accepted in *Special Session on Advanced Signal Processing Techniques in NDT/E for IEEE ISSPIT*, Ajman, UAE, December 14-17, 2009.

7. A. Algarni, I. Elshafiey, and M. Alkanhal, “Automation of Inspection with Image Fusion Application to Nondestructive Evaluation,” Ready to be submitted to *IEEE Transactions on Magnetics*.